UNIVERSITAT POLITÈCNICA DE VALÈNCIA

ESCOLA TÈCNICA SUPERIOR D'ENGINYERIA DEL DISSENY

Design of new bio-gated nanodevices for advanced communication processes and targeted controlled release of therapeutic agents

PhD. THESIS

Submitted by

Cristina Giménez Morales

PhD. Supervisors:

Dr. Félix Sancenón Galarza
Dr. Ramón Martínez Máñez

Valencia, January 2016

Instituto Interuniversitario de Reconocimiento Molecular y Desarrollo Tecnológico

Escuela Técnica Superior de Ingeniería del Diseño

RAMÓN MARTÍNEZ MÁÑEZ, PhD in Chemistry and Professor at the Universitat Politècnica de València, and FÉLIX SANCECNÓN GALARZA, PhD in Chemistry and Lecturer at the *Universitat Politècnica de València*.

CERTIFY:

That the work *"Design of new bio-gated nanodevices for advanced communication processes and targeted controlled release of therapeutic agents"* has been developed by Cristina Giménez Morales under their supervision in the Centro de Reconocimiento Molecular y Desarrollo Tecnológico de la *Universitat Politècnica de València*, as a thesis Project in order to obtain the degree of PhD in Chemistry at the *Universitat Politècnica de València.*

València, January 2016.

Prof. Ramón Martínez Máñez Dr. Félix Sancenón Galarza

A la meua família i a Santi.

Agraïments.

Aknowledgements. Agradecimientos.

Sembla mentira, però ha arribat el moment de tancar aquesta etapa. Realitzar durant estos anys la tesis doctoral ha suposat per a mi un llarg camí d'aprenentatge, de gran formació professional i, sobretot, de creixement personal i autoconeixement. Al llarg del camí he tingut la sort de coincidir amb persones excepcionals que m'han fet aquest recorregut més fàcil i més feliç. A tots i cada un de vosaltres, gràcies!

En primer lloc voldria donar les gràcies a Ramón per donar-me l'oportunitat de fer la tesis al seu grup d'investigació. Gràcies per confiar amb mi, a pesar de les meues inseguretats, i introduir-me i guiar-me en el món de la investigació. Gràcies Félix per la teua dedicació, per la teua infinita ajuda sempre que m'ha fet falta i per el teu suport al llarg d'estos anys. Gràcies Loles, Luis i Joserra, per el vostre suport, per ensenyar-me tantes coses i estar disposats sempre a tirar-me una mà. També vull agrair a Ángel Maquieira i a Núria la seua imprescindible ajuda amb els experiments amb el ICP.

Además, me gustaría agradecer al Dr. Manuel Serrano la oportunidad que me dió de realizar una estancia de investigación en su grupo. Muchas gracias por abrirme las puertas de tu laboratorio, por tu amabilidad y por tu disposición para hablar y discutir en todo momento sobre los experimentos. Para mí ha sido una de las experiencias más enriquecedoras en este camino de formación. Y como no, muchas gracias Dani por acogerme esos meses bajo tu tutela, por enseñarme tantísimas cosas, siempre con una sonrisa, y por tu amistad. Siempre recordaré esas tardes infinitas en patología examinando a los ratones (bisturí en mano), hablando de todo y de nada, y cruzando los dedos para obtener los resultados que esperábamos. Gracias por darme tu confianza y hacerme ver mis capacidades. Junto a Dani, muchas gracias a Cristina, Maribel y Juanma por vuestra gran ayuda. A pesar de que hacía cosas raras con nanopartículas, me habéis ayudado y enseñado mucho y habéis sido un gran apoyo. Además, quiero agradecer a todo el

grupo de Supresión Tumoral y al grupo de Telómeros por acogerme en el laboratorio, por prestarme toda la ayuda que he necesitado y por hacerme sentir realmente una más (a pesar de ser una ingeniera rodeada de biólogos). Me ha encantado conoceros y he disfrutado muchísimo compartiendo con vosotros los días en el laboratorio (y las cervezas de después). Gracias especialmente a mis compañeros de mesa y de risas, Montero, Ana y Miguel Ángel, os quiero mucho!

Per a continuar, gràcies a les meues "mamis" del laboratori del IDM, Elena, Carmen, Estela i Andrea, com agrair-vos tota la ajuda i el recolzament que meu donat...Gràcies per ensenyar-me tantíssimes coses, per donar-me suport al llarg de tots estos anys, per animar-me a reposar-me i seguir quan ho veia tot negre. Gràcies per guiar-me i per la vostra amistat. M'enduc molts bons moments amb vosaltres. Sou lo més! Aplegats a este punt em diríeu: "Floreta, en lo que hi ha és juga".

A més, vull agrair a totes les persones que han passat per el laboratori 2.6, que han sigut els meus companys de viatge en este llarg camí. Als que estaven al principi del camí: Maria (i la teua organització), Inma Candel, Inma Campos, Cris Sanfeliu, Laura, Yoli i Édgar (ma que eres bonico), gràcies per la vostra ajuda i per tots els bons moments passats al laboratori, sempre recordaré aquesta etapa del principi de la tesis (quant encara era ajena a la saturació de feina), erem entonces una "xicoteta" família en expansió. Especialment a Aless, que juntament amb Estela, vam conviure en aquella etapa feliç del nostre pis patera, quan erem un pack i es baquejaven de nosaltres per portar el mateix d'esmorzar i de dinar.

Gràcies també a la gent que va anar unint-se al grup, Sameh (gracias por ser tan bueno y hacerme reir), Luis Enrique, Carol, Patri, Marian i Roman per la seua ajuda i els bons moments al lab. Gràcies també a Cris T (eres una power girl, tu pots amb tot!) i a la gent que ha passat esporàdicament per el grup (Ravi, sé feliz!).

També vull agrair a la gent que s'ha unit al grup en l'última part del meu camí. Gràcies Toni, Cris M, Lorena, Santi, Alba, Mónica, M^{a} Elena, Adrián, Marta, Bea,

Luis (eres un crack), Àngela (Angelus!), Amelia i Irene per els bons moments que he passat al lab amb vosaltres i per el entusiasme que despreneu. Gràcies Eli per les rises i els bons moments a la CPI (ànim i avant perla!). També vull agrair a Amelia el seu recolzament al laboratori i el suport que m'ha donat. Eres molt tenaç i faenera, estic segura que aplegaràs on vulgues! Gràcies també a Irene perquè m'has ajudat molt en l'última part del meu treball (juntament amb el teu patito Regina, altra crack, fèiem l'equip senescència!!). Eres una gran persona i a més boníssima amb la feina, sempre tan perseverant amb els teus objectius. M'ha encantat treballar amb tu i poder compartir les alegries (i, al nostre pesar, maldecaps) que ens ha dut el dia a dia en este projecte. Estic segura que aconseguiràs tot allò que et proposes.

Moltes gràcies als que han sigut els meus companys indispensables de caminada, a Mar, Dani, Neus, Núria, Almu, Lluís i María R. També a Carles i Isa, que han patit els efectes colaterals. Hem fet un comboi de por!! Només dir-vos que vos estime i que la vostra amistat és el més gran que m'enduc d'estos anys.

Per últim, vull agrair a la meua família tot el seu suport incondicional. Especialment als meus pares i a la meua germana, que sempre em segueixen i em recolzen en tots els empreniments que faig. Gràcies per estar sempre ahi, per escoltar-me riure i plorar, per el vostre infinit amor i per donar-me tot el que soc. Si he aplegat fins ací ha sigut gràcies a vosaltres. I com no, gràcies Santi. Has patit també els efectes colaterals de la tesis. Gràcies per el teu suport, per escoltar-me i intentar entendre'm, i per fer-me sempre riure. Moltes gràcies per estar sempre ahi demostrant-me el teu amor.

Agraïments

Abstract

The present PhD thesis, which is entitled “Design of new bio-gated nanodevices for advanced communication processes and targeted controlled release of therapeutic agents” is focused on the development of new functional hybrid organic-inorganic materials for applications in the field of the controlled delivery of target molecules.

The first chapter of the present thesis gives an introduction to the organic-inorganic hybrid materials functionalized with “molecular gates" and its application in controlled release processes.

The second chapter of this thesis is focused on the development of a new nanodevice able to deliver its cargo as a function of the glucose concentration. The nanodevice is based on mesoporous silica nanoparticles loaded with a suitable fluorophore and functionalized with propylbenzymidazole moieties on the pore outlets. The mesopores are then capped with an active cyclodextrin modified glucose oxidase enzyme (through the formation of an inclusion complex between the cyclodextrins and the propylbenzymidazole group anchored to the solid support). When glucose is added its enzymatic oxidation produced gluconic acid. This acid induced a decrease in the pH of the medium and the protonation of the benzymidazole group that might result in the inclusion complex dethreading and the subsequent cargo release.

The third chapter of the thesis is focused on the development of a new redox-responsive material for the controlled delivery of cytotoxic drugs in cancer cells.
The system is based on mesoporous silica nanoparticles loaded with a reporter (safranin O) and functionalized with two different sized polyethylene glycol chains in the pore outlets using a disulfide linkage. In presence of glutathione, the disulfide bonds are cleaved allowing the release of the entrapped cargo. Once confirmed the aperture protocol, the uptake of the gated nanoparticles and their

ability to deliver the cargo (fluorophore or cytotoxic agent) in HeLa cells were tested. Moreover, cell viability assays were also performed.

The fourth chapter of the thesis is focused on the preparation and the study of a nanodevice for the controlled delivery in senescent cells in a murine model of pulmonary fibrosis. The material is prepared using mesoporous silica nanoparticles (as an inorganic support) and galactoligosaccharide (molecular gate) moieties anchored on the external surface. In presence of senescent cells, which overexpress β-galactosidase enzyme, the hydrolysis of the galactooligosaccharide capping molecules take place and the cargo release from the inner of the pores is produced (rhodamine B). After the *in vitro* studies, the ability of nanoparticles to accumulate and release their payload in tissues with abundance of senescent cells was evaluated *in vivo*. For that purpose, mice with induced pulmonary fibrosis, pathogenesis with associated increased alveolar senescence, were treated with the synthesized material and subsequently examined to assess its ability to accumulate and release its payload (fluorophore) in lung's damaged areas.

In the fifth chapter of the thesis it has been explored the concept of cascade chemical communication using different types of nanodevices, each of them loaded with a certain messenger and externally functionalized with a gate-like entity that controls the release of the payload. When the enzyme able to hydrolyze the molecular gate that blocks the pores of the first type of nanoparticles (**S1**), is added to an aqueous suspension containing the three nanoparticles, the delivery of the chemical messenger 1 is produced. This messenger is able to open the second type of nanoparticles (**S2**) which delivers the messenger 2. Finally, the messenger 2 triggers the aperture of the third group of gated system (**S3**), which ultimately delivers its load (a dye) as a final response.

Resumen

La presente tesis doctoral titulada “Diseño de nuevos nanodispositivos para procesos avanzados de comunicación y liberación controlada y dirigida de agentes terapéuticos” está centrada en el desarrollo de nuevos materiales híbridos orgánico-inorgánicos funcionales para aplicaciones en el campo de la liberación controlada de moléculas de interés.

El primer capítulo de la tesis ofrece una introducción a los materiales híbridos orgánico-inorgánicos funcionalizados con “puertas moleculares” y su aplicación en procesos de liberación controlada.

En el segundo capítulo de la tesis se aborda el desarrollo de un nanodispositivo capaz de responder y liberar su carga en función de la concentración de glucosa. Este nanodispositivo está basado en nanoparticulas de sílice mesoporosa funcionalizadas en su superficie externa con grupos benzimidazol y con los poros cargados con un fluoróforo. Los poros se cierran al añadir la enzima glucosa oxidasa funcionalizada con ciclodextrinas (por formación de un complejo de inclusión entre el benzimidazol y los oligosacáridos cíclicos). Al adicionar glucosa se produce su oxidación enzimática dando ácido glucónico. Este ácido induce una bajada del pH del medio con la consiguiente protonación de los benzimidazoles y la ruptura de los complejos de inclusión. Esta ruptura provoca la salida de la enzima de la superficie y la liberación del colorante atrapado en los poros.

El tercer capítulo de la tesis se ha centrado en el desarrollo de un material capaz de liberar su carga en respuesta a cambios en el potencial redox para la liberación controlada de agentes citotóxicos en células cancerosas. De nuevo se emplean nanopartículas de sílice mesoporosa con los poros cargados con un colorante (safranina O) y la superficie externa funcionalizada con dos polietilenglicoles (de diferente peso molecular) conteniendo enlaces disulfuro. En presencia de glutatión se produce la reducción del enlace disulfuro con la consiguiente liberación del colorante. Una vez confirmado el protocolo de apertura, se estudió

la internalización y la liberación de un fluoróforo y de un agente citotóxico en el modelo celular HeLa, realizando además ensayos de viabilidad.

En el cuarto capítulo de la tesis se ha preparado y ensayado un nanodispositivo para la liberación controlada en células senescentes en un modelo murino de fibrosis pulmonar. El material se prepara empleando nanopartículas de sílice mesoporosa (como soporte inorgánico) y un galactooligosacárido (puerta molecular) anclado en la superficie externa. En presencia de células senescentes, que sobreexpresan la enzima β-galactosidasa, se produce la hidrólisis del oligosacárido con la consiguiente liberación de la carga atrapada en los poros del soporte (rodamina B). Tras esto, la capacidad del nanodispositivo de acumularse y liberar su carga en tejidos ricos en células senescentes se evaluó *in vivo*. Para ello, ratones con fibrosis pulmonar inducida, patología en la que se ha descrito la aparición de senescencia en los tejidos dañados, se trataron con el material sintetizado y posteriormente fueron examinados para comprobar la capacidad de acumularse y liberar su carga (fluoróforo) en la zona pulmonar dañada.

En el quinto capítulo se ha explorado el proceso de comunicación química en cascada empleando tres tipos de nanopartículas mesoporosas de sílice cargadas con diferentes mensajeros y funcionalizadas con tres puertas moleculares distintas. Cuando sobre una suspensión de las tres nanopartículas se añade la enzima capaz de hidrolizar la puerta molecular que bloquea los poros del primer tipo de nanopartículas (**S1)**, se produce la liberación del mensajero 1. Este mensajero es capaz de inducir la apertura del segundo tipo de nanopartículas (**S2**), que a su vez liberan al medio el mensajero 2. Por último, el mensajero 2 es capaz de abrir la puerta molecular del tercer tipo de nanopartículas (**S3**), que liberan finalmente su carga (un colorante) como respuesta final.

Resum

La present tesis doctoral titulada “Disseny de nous nanodispositius per a processos avançats de comunicació i lliberació controlada i dirigida d’agents terapèutics” està centrada en el desenvolupament de nous materials híbrids orgànic-inorgànic funcionals per a aplicacions en el camp de la lliberació controlada de molècules d’interès.

El primer capítol de la tesis ofereix una introducció als materials híbrids orgànic-inorgànic funcionalitzats amb “portes moleculars” i la seua aplicació en processos de lliberació controlada.

En el segon capítol de la tesis s’aborda el desenvolupament d’un nanodispositiu capaç de respondre i lliberar la seua càrrega en funció de la concentració de glucosa. Este nanodispositiu està basat en nanopartícules de sílice mesoporoses funcionalitzades a la seua superfície externa amb grups benzimidazol i amb els pors carregats amb un fluoròfor. Els pors queden bloquejats al afegir el enzim glucosa oxidasa funcionalitzada amb ciclodextrines (per formació d’un complex d’inclusió entre el benzimidazol i els oligosacàrids cíclics). Al afegir glucosa es produeix la seua oxidació enzimàtica donant lloc a àcid glucònic. Este àcid indueix una baixada del pH del medi amb la consegüent protonació dels benzimidazols i el trencament dels complexes d’inclusió. Este trencament provoca l’eixida del enzim de la superfície i la lliberació del colorant atrapat als pors.

El tercer capítol de la tesis s’ha centrat en la preparació d’un material per a la lliberació controlada d’agents citotòxics en cèl·lules canceroses en resposta a canvis en el potencia redox. De nou s’empren nanopartícules de sílice mesoporoses amb els pors carregats amb un colorant (safranina O) i la superfície externa funcionalitzada amb dos polietilenglicols (de diferent pes molecular) contenint enllaços disulfur. En presència de glutatió es produeix la reducció del enllaç disulfur amb la consegüent lliberació del colorant. Una volta confirmat el protocol d’obertura, es va estudiar la internalització i la lliberació d’un fluoròfor i

d'un agent citotòxic en el model cel·lular HeLa, realitzant ademés assajos de viabilitat.

En el quart capítol de la tesis s'ha preparat i s'ha estudiat un nanodispositiu per a la lliberació controlada en cèl·lules senescents, en un model murí de fibrosis pulmonar. El material es prepara emprant nanopartícules de sílice mesoporoses i un galactooligosacàrid anclat a la superfície externa del material. En presència de cèl·lules senescents, que sobreexpresen el enzim β-galactosidasa, es produeix la hidròlisis del oligosacàrid amb el consegüent alliberament de la càrrega atrapada en els pors del suport (rodamina B). Després dels estudis *in vitro*, la capacitat del nanodispositiu d'acumular-se i lliberar la càrrega en teixits rics en cèl·lules senecents es va evaluar *in vivo*. Amb este propòsit, ratolins amb fibrosis pulmonar induïda, patologia en la que s'ha descrit l'aparició de senescència en els teixits danyats, es van tractar amb el material sintetitzat i posteriorment van ser examinats per a comprovar la capacitat d'acumular-se i lliberar la seua càrrega (fluoròfor) en la zona dels pulmons afectada.

En el quint capítol s'ha explorat el procés de comunicació química en cascada utilitzant tres tipus de nanopartícules mesoporoses de sílice carregades amb diferents missatgers i funcionalitzades amb tres portes moleculars diferents. Quan, sobre una suspensió de les tres nanopartícules, s'afegeix l'enzim capaç d'hidrolitzar la porta molecular que bloqueja els pors del primer tipus de nanopartícules (**S1**), es produeix la lliberació del missatger 1 des de **S1**. Este missatger és capaç d'induir l'obertura del segon tipus de nanopartícules (**S2**), les quals lliberen al medi el missatger 2. Per últim, el missatger 2 és capaç d'obrir la porta molecular del tercer tipus de nanopartícules (**S3**), que lliberen finalment la seua càrrega (un colorant) com a resposta final.

Abbreviations

4OHT	*4-hydroxytamoxifen*
AMF	*Alternating magnetic field*
APase	*Acid phosphatase enzyme*
ATP	*Adenosine triphosphate*
AuNPs	*Gold nanoparticles*
BET	*Brunauer-Emmet-Teller*
BJH	*Barrett-Joyner Halenda*
CD-GOx	*CD-modified-glucose oxidase*
CLSM	*Confocal laser scanning microscopy*
CMC	*Critical micelar concentration*
CNIO	*Spanish National Cancer Research Centre*
CTAB	*Hexadecyltrimethylammonium bromide*
DDS	*Drug delivery systems*
DIC	*Differential interference contrast*
DNA	*Deoxyribonucleic acid*
DNPD	*1,5-dioxynaphtalene derivative*
DOPC	*1,2-dioleoyl-sn-glycero-3-phosphocholine*
DOX	*Doxorubicin*
DTAB	*dodecyltrimethylammonium bromide*
DTT	*Dithiotheritol*
Dtxl	*Docetaxel*
EA	*Elemental analysis*
FA	*Folic acid*
FDA	*U.S. Food and Drug Administration*
FT-IR	*Fourier transformed infrared spectroscopy*
GOS	*Galactoligosaccharide*
GSH	*Glutathione*
HIFU	*High intensity focused ultrasound*
ICP-AES	*Inductively coupled plasma-atomic emission spectrometry*

Abbreviations

IPF	*Idiopathic Pulmonary Fibrosis*
IT	*Iintratracheal instillation*
LCST	*Lower critical solution temperature*
LD50	*Lethal dose 50*
MCM-41	*Mobile Crystalline Material with a hexagonal arrangement of the mesopores*
MDR	*Multidrug resistance*
ME	*Mercaptoethanol*
Mn	*Number average molecular weight*
MSN	*Mesoporous silica nanoparticles*
MTD	*Maximum tolerated dose*
OIS	*Oncogene-induced senescence*
p.i	*Post injection*
p.t	*Post treatment*
PEG	*Polyethylene glycol*
PFH	*Perfulorohexane*
PMOs	*Periodic Mesoporous Organosilicas*
PTFE	*Polytetrafluoroethylene, Teflon*
Rh	*Rhodamine*
SASP	*Senescence-associated secretory phenotype*
SAβ-Gal	*Senescence-associated β-galactosidase*
SBA	*Santa Barbara Amorphous Material*
TCEP	*Tris(2-carboxyethyl)phosphine*
TEM	*Transmission electron microscopy*
TEOS	*Tetraethylortosilicate*
TGA	*Thermogravimetric*
TLCT	*True liquid-crystal templating mechanism*
TMHA	*Tetramethylammonium hydroxide*
TMOS	*Tetramethylortosilicate,*
US	*Ultrasounds*
UV	*Ultraviolet*
WT	*Wild-type*

x-gal	*5-bromo-4-chloro-3-indolyl-beta-D-galactopyranoside*
XRD	*powder X-ray diffraction*
β-Gal	*β-galactosidase*
4OHT	*4-hydroxytamoxifen*

Content

Content

1. General introduction

1.1 **Nanotechnology**

In 1959, Richard Feynman gave a talk called "There's Plenty of Room at the Bottom" at an annual meeting of the American Physical Society at Caltech. In this conference, Feynman laid the conceptual foundations for the field now called nanotechnology when he imagined "a day when things could be miniaturized, when huge amounts of information could be encoded onto increasingly small spaces, and when machinery could be made considerably smaller and more compact". Today, nanotechnology has considerably improved, even revolutionized, many technological and industrial sectors. Moreover, there is any segment of human life and activity in which nanotechnology cannot be applied.

Encompassing diverse fields such as physics, chemistry, biology, materials science and engineering, nanotechnology involves imaging, measuring, modeling and manipulating matter at a molecular level driving out novel and exciting properties. This complex interdisciplinary science is focused on a comprehensive research of nanostructures, on a development of atomistic physico-chemical processes and self-assembling of nanomaterials for the fabrication of nanodevices, ultra-low integrated circuits, microopto-electro-mechanical systems, etc.

The development of nanomaterials is an activity that has been growing explosively worldwide in the past few years. Engineered nanomaterials are resources designed at the molecular (nanometer) level to take advantage of their small size and of its novel properties which are generally not seen in their conventional bulk counterparts. The two main reasons why materials at the nano scale can have different properties are their increased relative surface area and new quantum effects that arises from this fact. These emergent properties have the potential for creating new products with applications in fields such as biotechnology, medicine, electronics, chemistry or photonics.[1]

[1] A. Alagarasi, *Introduction to Nanomaterials*, in B. Viswanathan, Nanomaterials, **2009**, Ed. Narosa Publishing House.

1.2 **Organic-Inorganic Hibrid Nanomaterials for Advanced Applications**

In advanced technologies, the optimization of numerous applications need a set of requirements sustained in many cases by divergent properties that are very difficult to satisfy by using single component based materials. In this context, the combination of organic and inorganic building blocks within a single material is particularly attractive from the viewpoint of materials scientists.

The assembly of organic or biological molecules and inorganic components generates new complex materials with extraordinary features, which arise from the synergism between the properties of the components.[2] Hybrid organic inorganic materials are not simply physical mixtures. They can be broadly defined as molecular or nano-composites with (bio)organic and inorganic components, intimately mixed where at least one of the component domains has a dimension ranging from a few Å to several nanometers. Consequently the properties of hybrid materials are not only the sum of the individual contributions of both phases, but the role of their inner interfaces could be predominant.[3]

These multifunctional materials constitute a golden gate giving access to a large variety of tunable modern systems and devices. Moreover, the combination of supramolecular chemistry, inorganic solids, and nanotechnology has already led to significant advances in many areas such as sensing, controlled motion, and delivery. [4]

[2] a) P.A. Gale and R. Quesada, *Coord. Chem. Rev.,* **2006**, *250*, 3219. b) J. F. Callan, A. P. de Silva, D. C. Magri, *Tetrahedron*, **2005**, *61*, 8551. c) G. J. Mohr, Sens. Actuators B, 2005, 107, 2.

[3] C. Sánchez, *J. Mater. Chem*., **2005**, *15*, 3557.

[4] K. Rurack, R. Martínez-Máñez, *The supramolecular chemistry of organic-inorganic hybrid materials*, **2010**, Ed. John Wiley & Sons.

This PhD thesis is centered on the development of new hybrid nanomaterials for their application in the field of nanomedicine. The designed nanomaterials make use of mesoporous silica nanoparticles (MSN) as inorganic scaffoldings in which certain (bio)organic molecules are grafted in the outer surface. The anchored (bio)organic molecules confers improved properties and advanced functionalities to the final nanomaterials. The underlying idea is to apply the advanced smart nanomaterials prepared in controlled release protocols in pharmaceutical and medical applications.

1.2.1 Mesoporous silica materials as inorganic scaffolds

In the last century, porous materials with large specific surface areas have been attracted considerable research attention due to their potential applications in areas such as adsorption,[5] separation,[6] catalysis,[7] gas storage[8] and sensor technology.[9] According to their pore sizes, porous materials are classified by IUPAC, the International Union of Pure and Applied Chemistry, as microporous (pore size < 2 nm), mesoporous (2–50 nm) and macroporous (> 50 nm) materials.

The properties of these materials and thus, their suitability for different applications depend, to a large extent, on the characteristics of the porous system. Therefore, the development of new methodologies for the synthesis of materials with specific porosity architectures has been strongly encouraged.

As an example, zeolites are a family of microporous aluminosilicate materials able to "sieve" molecules having certain dimensions and allow them to enter the pores. Zeolites are widely used in industry for catalysis,[10] gas separation[11] and ion

[5] K. M. Thomas, *Catal. Today*, **2007**, *120*, 389.
[6] G. Sneddon, A. Greenaway, H. H. P. Yiu, *Adv. Energy Mater*., **2014**, *4,* 130187
[7] C. Perego, R. Millini, *Chem. Soc. Rev.,* **2013**, *42*, 3956.
[8] R. E. Morris and P. S. Wheatley, *Angew. Chem. Int. Ed.*, **2008**, *47*, 4966.
[9] D. J. Wales, J. Grand, V. P. Ting, R. D. Burke, K. J. Edler, C. R. Bowen, S. Mintova, A. D. Burrows, *Chemical Society Reviews,* **2015**, *44,* 4290.
[10] J. Weitkamp, *Solid State Ionics,* **2000**, *131*, 175.

exchange.[12] Moreover, synthetic zeolites are the most important catalysts in petrochemical refineries and played crucial roles in petroleum refining, synfuels preparation, and petrochemical production. This widespread use of zeolites in industry is mainly due to properties such as a narrow pore size distributions and a readily tunable pore size in a wide range. Moreover, around 229 zeolite frameworks have been identified until now.[13] Despite these facts, zeolites become inadequate when have to be processed reactants with sizes above the dimensions of the pores, which were restricted to around 15 Å.

The inadequate pore size of zeolites directed the research interest of the major oil companies to the field of materials science in order to explore the possibility to prepare new solids with expanded pore sizes. Into this context, in 1992, a research group of the Mobil Oil Company reported the preparation and characterization of a new family of periodic mesoporous silicas known as the M41S phases.[14]

Like the microporous crystalline zeolites, this class of materials is characterized by very large specific surface areas, with values between 500 and 1000 m^2/g, ordered pore systems, and well-defined pore radius distributions. The pore size of the M41S materials is in the range of 2-10 nm. In addition, these materials have a high pore volume from the order of 1 cm^3/g and exhibit amorphous pore walls. The best-known representatives of this class of materials include the silica solid MCM-41 (Mobile Crystalline Material with a hexagonal arrangement of the mesopores),

---

[11] N. K. Jensen, T. E. Rufford, G. Watson, D. K. Zhang, K. I. Chan, and E. F. May, *J. Chem. Eng. Data,* **2012,** *57*, 106.

[12] a)H. S. Sherry and H. F. Walton, *The Journal of Physical Chemistry,* **1967**, *71,* 1457. b) M. J. Stephenson , S. M. Holmes and R. A. W. Dryfe, *Angew. Chem. Int. Ed.* **2005**, *44*, 3075.

[13] a) International Zeolite Association, Database of Zeolite Structures. b) J. D. Dana, E. S. Dana, R. V. Gaines, *Dana's New Mineralogy: The System of Mineralogy of James Dwight Dana and Edward Salisbury Dana,* **1997**, Ed. Wiley.

[14] a) C. T. Kresge, M. E. Leonowicz, W. J. Roth, J. C. Vartuli, J. S. Beck, *Nature,* **1992**, *359*, 710. b) J. S. Beck, J. C. Vartuli, W. J. Roth, M. E. Leonowicz, C. T. Kresge, K. D. Schmitt, C. T. W. Chu, D. H. Olson, E. W. Sheppard, *J. Am. Chem. Soc.,* **1992**, *114*, 10834.

MCM-48 (with a cubic arrangement of mesopores) and MCM-50 (with a lamellar structure), which are depicted in Figure 1.

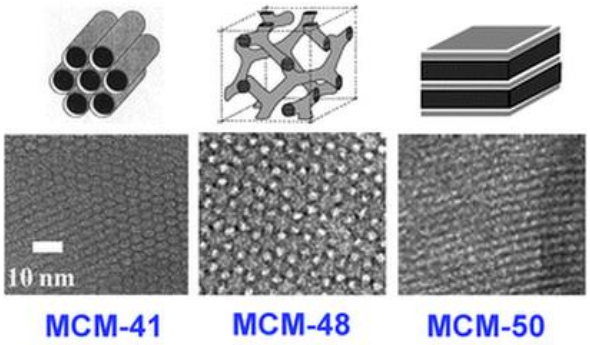

Figure 1. Structures of mesoporous M41S materials: Surfactant supramolecular assemblies are shown on top and TEM images of the final materials at the bottom. *Reprinted with permission from Chem. Soc. Rev., 2013, 42, 3663. Copyright © 2013 The Royal Society of Chemistry.*

Moreover, those M41S materials are featured by high chemical inertness and thermal stability. On the other hand, their synthesis requires inexpensive and non-hazardous precursors that are simple enough for large-scale production and that can be chemically modified using the well-known silicon oxide functionalization chemistry.[15]

Due to their highly organized porosity, high surface area, high pore volume, tailorable pore size, wall thickness, chemical nature and morphology the mesoporous silica are attractive materials for applications in catalysis,[16] filtration and separation,[17] gas adsorption and storage,[18] chemical/biochemical sensing,[19] enzyme immobilization,[20] biomedical tissue regeneration[21] and drug delivery.[22]

[15] F. Hoffmann, M. Cornelius, J. Morell, M. Fröba, *Angew. Chem. Int. Ed.,* **2006**, *45,* 3216.

[16] D.E. De Vos, M. Dams, B.F. Sels, P.A. Jacobs, *Chem. Rev.,* **2002,** *102,* 3615.

[17] X. Liu, Y. Du, Z. Guo, S. Gunasekaran, C. -B. Ching, Y. Chen, S .S .J. Leong, Y. Yang, *Microporous Mesoporous Mater.,* **2009**, *122*, 114.

[18] a) M. Kruk, M. Jaroniec, *Chem. Mater.*, **2001**, *13,* 3169. b) A. Corma, M. Moliner, M. J. Diaz-Cabanas, P. Serna, B. Femenia, J. Primo, H. Garcia, *New J. Chem.,* **2008**, *32*, 1338. c) C. Ispas, I. Sokolov, S. Andreescu, *Anal. Bioanal. Chem*., **2009**, *393*, 543.

1.2.2 Synthesis of inorganic mesoporous materials

Generally, the synthesis of inorganic mesoporous silica materials is accomplished by the use of a ***template*** that acts as a structure-directing agent, and the use of a ***polymeric precursor***, which has to self-organize around the template and, upon polymerization, build up the final rigid structure.

Instead of using small organic molecules as templating compounds, as in the case of zeolites, supramolecular aggregates of ionic surfactants are employed as the structure-directing agent during the synthesis of these highly ordered materials. As a consequence, the porosity properties of the mesoporous materials would depend on the type of surfactant employed during the true liquid-crystal templating mechanism (TLCT).

In detail, this synthetic process is based on the dissolution of surfactant molecules into polar solvents to yield the so-called liquid crystals. When the concentration of surfactant is above the critical micellar concentration (CMC), the surfactant molecules aggregate themselves to form micelles. The characteristics of these micelles depend on the nature of the employed surfactant, its concentration and temperature, although factors such as the pH of the solution and the total salt concentration. Those micelles organize themselves into supermicellar structures and, depending on the same factors reported before, different kind of supermicellar aggregates can be obtained. The resulting mesoporous framework depends on these supramicellar geometries, such as hexagonal, cubic, and laminar (see Figure 2).

---

[19] a) K. A. Kilian, T. Boecking, K. Gaus, M. Gal, J. J. Gooding, *ACS Nano*, **2007**, *1,* 355. b) A. Jane, R. Dronov, A. Hodges, N. H. Voelcker, *Trends Biotechnol.*, **2009**, *27*, 230.

[20] M. Vallet-Regi, M. Colilla, I. J. Izquierdo-Barba, *Biomed. Nanotechnol.,* **2008**, *4*, 1.

[21] I. I. Slowing, B. G. Trewyn, S. Giri, V. S. –Y. Lin, *Adv. Funct. Mater.,* **2007**,*17*, 1225.

[22] a) M. Vallet-Regi, F. Balas, D. Arcos, *Angew. Chem., Int. Ed.,* **2007**, *46*, 7548. b) K. A. Kilian, T. Bocking, K. Gaus, J. King-Lacroix, M. Gal, J. J. Gooding, *Chem. Commun.,* **2007**, 1936.

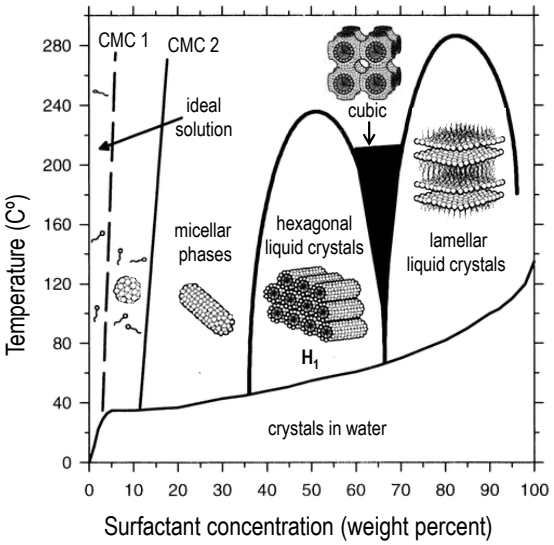

Figure 2. Schematic phase diagram for the surfactant cetyltrimethylamonium bromide (CTAB) in water. The aggregation of surfactant molecules into micelles and then into lyotropic liquid crystalline phases as a function of concentration and of temperature is shown. Adapted from *Chem. Mater.,* 1996, 8, 1682, *Copyright © 1996 American Chemical Societ.*

In the synthesis of silica based ordered inorganic scaffolds, oligomeric silicates, originating from different sources of silica (sodium silicate, alkoxydes like tetraethylortosilicate, TEOS and tetramethylortosilicate, TMOS) are used as a polymeric silica precursors.

Then, once the supramicellar aggregates are formed, the silica precursors are added. In the next step, the molecules of the silica precursor, are hydrolyzed and condensed around the supramicellar aggregates yielding a silicon oxide phase. The mesoporous final materials are obtained by subsequent removal of the surfactant contained within the pores by extraction with adequate solvents or by aerobic high temperature calcination.

Besides the TLCT mechanism, researchers have found that it is also possible to obtain these mesoporous materials following a different path, which is based in the co-assembly between the inorganic precursor and the structure directing agent. This mechanism considers that liquid-crystalline phase is formed even at

lower concentrations of surfactant molecules, through a cooperative self assembly of the template molecules and the added inorganic species,[23] as can be seen in Figure 3.

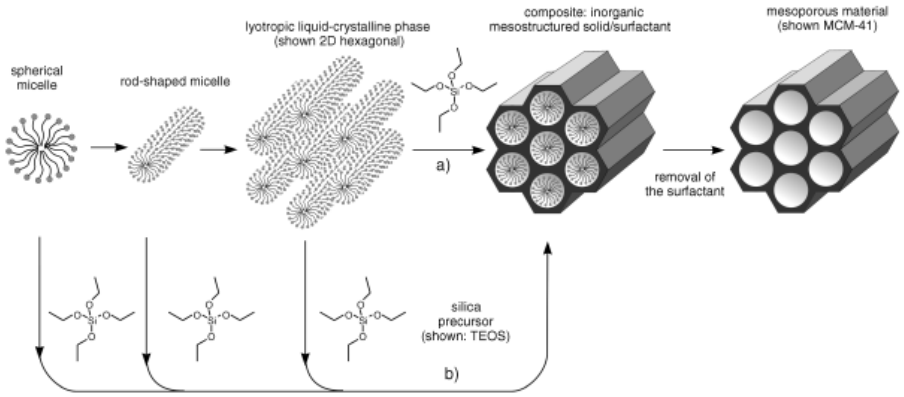

Figure 3. Formation of mesoporous materials by structure-directing agents: a) true liquid-crystal template mechanism; b) cooperative liquid crystal template mechanism. *Adapted from Angew. Chem. Int. Ed. 2006, 45, 3216. Copyright © 2006 Wiley.*

In any case, synthesis conditions such as source of silica, pH and composition of the reaction mixture, ionic strength, type of surfactant used, temperature and time affect the surfactant micellar conformation, the silica-surfactant interactions and the degree of silica poly-condensation. These conditions determine the characteristics of the porous structure (type of mesostructure, diameter and volume of the pores, wall thickness) and the macroscopic morphology.

Meanwhile, these template-synthetic routes have also been used, with a large number of variations, with the aim to obtain a wide variety of mesoporous materials with a defined topology and morphology. As an example, the use of triblock copolymer templates under acidic conditions was employed to prepare the so-called SBA (Santa Barbara Amorphous) silica phases.[24]

[23] A. Monnier, F. Scheth, Q. Huo, D. Kumar, D. Margolese, R. S. Maxwell, G. Stucky,M. Krishnamurty, P. Petroff, A. Firouzi, M. Janicke, B. Chmelka, *Science*, **1993**, *261*, 1299.

[24] a) D. Zhao, J. Feng, Q. Huo, N. Melosh, G.H. Fredrickson, B.F. Chmelka, G.D. Stucky, *Science*, **1998**, *279*, 548. b) D. Zhao, Q. Huo, J. Feng, B.F. Chmelka, G.D. Stucky, *J. Am. Chem. Soc.,* **1998**, *120*, 6024.

Within the M41S materials, the Mobile Crystalline Material with a hexagonal arrangement of the mesopores (MCM-41), is the best known and the most widely studied and used. As can be seen in Figure 3, the synthesis of MCM-41 deals with the polymerization of TEOS, used as inorganic siliceous precursor, around super-micellar-template formed by the surfactant hexadecyltrimethylammonium bromide (CTAB), under basic conditions. The obtained as-synthesized material may undergo a calcination or extraction process in order to obtain the final scaffold with free mesopores.

The final MCM-41 mesoporous scaffold presents cylindrical unidirectional empty channels of approximately 2.5 nm of diameter arranged in a hexagonal distribution. As mentioned above, the particle morphology of the synthetized MCM-41 material depends on the reaction parameters and can be adjusted to obtain micrometric and heterogeneous particles or nano-sized particles.[25] Moreover, the properties of the mesoporous MCM-41 material can be tuned through the introduction of small changes in the synthesis route or with a post-synthesis treatment. The modulation of the pore sizes is among one of the most desirable properties. MSN pore size can be easily modulated during the synthesis by controlling the reaction time and temperature,[26] by using suitable swelling organic molecules,[27] by adjusting the type and concentration of the surfactant,[28] or by post synthesis treatment.[29]

---

[25] a) H. B. S. Chan, P. M. Budd, T. D. V. Naylor, *J. Mater. Chem.,* **2001**, *11*, 951. b) Q. Cai, Z.-S. Luo, W.-Q. Pang, Y.-W. Fan, X.-H. Chen and F.-Z. Cui, *Chem. Mater.*, **2001**, *13,* 258. c) S. P. Naik, W. Fan, T. Yokoi, T. Okubo, *Langmuir*, **2006**, *22*, 6391. d) J. Kobler, K. Moller, T. Bein, *ACS Nano*, **2008**, *2*, 791.

[26] T. R. Pauly and T. J. Pinnavaia, *Chem. Mater.,* **2001,** *13*, 987

[27] a) K.-C. Kao, C.-Y. Mou, *Microporous Mesoporous Mater.,* **2013**, *169,* 7. b) A. S. Hamoudi, *Chem. Mater.,* **2001**, *13,* 3151. c) G. Sponchia, R. Marin, I. Freris, M. Marchiori, E. Moretti, L. Storaro, P. Canton, A. Lausi, A. Benedetti, P. Riello, *J. Nanopart. Res.,* **2014**, *16*, 2245. d) K. Zhang, L.-L. Xu, J.-G. Jiang, N. Calin, K.-F. Lam,S.-J. Zhang, H.-H. Wu, G.-D. Wu, B. Albela, L. Bonneviot and P. Wu, *J. Am. Chem. Soc.*, **2013**, *135*, 2427.

[28] a)A. Corma, Q. Kan, M. T. Navarro, J. Perez-Pariente, F. Rey, *Chem. Mater.*, **1997**, *9*, 2123. b) F. Gao, P. Botella, A. Corma, J. Blesa and L. Dong, *J. Phys. Chem. B.,* **2009**, *113*, 1796.

[29] N. Ž. Knežević and J.-O. Durand, *Nanoscale*, **2015,***7*, 2199.

1.2.3 Functionalization of MCM-41 scaffolds

The incorporation of organic groups (functionalization) into these silica-based mesoporous materials is particularly attractive because of the possibility to combine the functional variation of organic chemistry with the benefits of a mechanically and thermally stable inorganic scaffold.

The covalent modification of MCM-41 support can be easily carried out through their high concentration of structural defects in the form of silanol (Si-OH) groups than act as convenient anchoring points for organic functionalization. The reaction of these silanols with trialkoxysilane derivatives (with structures $(R'O)_3$-Si-R in which R is an organic group) to give a nucleofilic substitution is the most common methodology to functionalize these supports and generate a novel class of mono-functional and multifunctional organic–inorganic hybrid materials. The introduction of organic moieties allow the fine tuning of surface properties (hydrophilicity, hydrophobicity and binding to guest molecules), the alteration of the surface reactivity, the protection of the surface against chemical attack, the hydrophobization of the surface to avoid water attack, and the modification of the bulk properties of the materials while at the same time stabilizing the materials towards hydrolysis.

Generally, two different synthetic strategies are used to functionalize the surfaces of mesoporous scaffolds and produce hybrid organic-inorganic materials, the grafting and the co-condensation procedures.[30]

✓ *GRAFTING PROCEDURE*

In this method, the prepared mesostructured silica material is functionalized with the selected organic groups in a post- synthesis stage (See Figure 4).

[30] A. Vinu, K. Z. Hossain, K. Ariga, *Nanosci. Nanotech*., **2005**, *5*, 347.

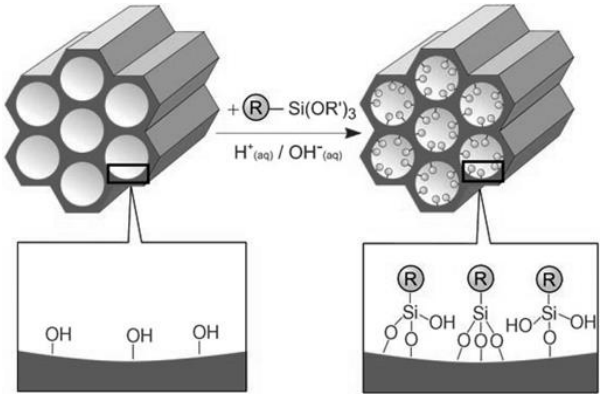

Figure 4. Grafting (postsynthetic functionalization) for organic modification of mesoporous pure silica phases with terminal organosilanes of the type $(R'O)_3SiR$. R=organic functional group. *Adapted from Angew. Chem. Int. Ed. 2006, 45, 3216. Copyright © 2006 Wiley.*

The advantage of this method is that the original structure of the mesoporous support is generally maintained after functionalization. On the other hand, when a final mesoporous material (after the template removal) is functionalized by grafting, the external surface is more accessible and is functionalized predominantly over the internal mesopore surface. This fact can in turn lead to a non-homogeneous distribution of the organic groups on the material surface, and a lower degree of occupation within the pores. Moreover, in cases when the grafting species are very bulky, the preferential external functionalization of the material can lead to complete closure of the pores.

In order to favor the internal surface functionalization, or to achieve a dual functionalization of the material, different strategies can be followed. To minimize the involvement of the external surface in reaction processes it is possible to passivate these surfaces first, before functionalizing the internal silanol groups. Other strategy for a selective functionalization of external and internal MCM-41 surfaces is to use the as-synthesized mesoporous sieve, whose pores were still filled with the surfactant template, in the first step of functionalization. Then, the surfactant template can be removed by extraction and a second step of functionalization can be performed. The suitability of these methods depends on the properties of the grafting species (size, reactivity...).

✓ *CO-CONDENSATION PROCEDURE*

This procedure is an alternative method to synthesize organically functionalized mesoporous silica phases in one-pot synthesis. In this case, the precursor functional group ($(R'O)_3$-Si-R) is incorporated into the synthesis at the same time as the corresponding tetraalkoxysilanes ($(RO)_4$-Si , TEOS or TMOS). In aqueous medium, the alkoxy groups are hydrolyzed and reacted with the silica skeleton precursors, and a simultaneous condensation of both takes place. The resulting material presents homogeneously distributed organic groups R which are bonded to silicon atoms of the internal and external material surfaces (Figure 5).

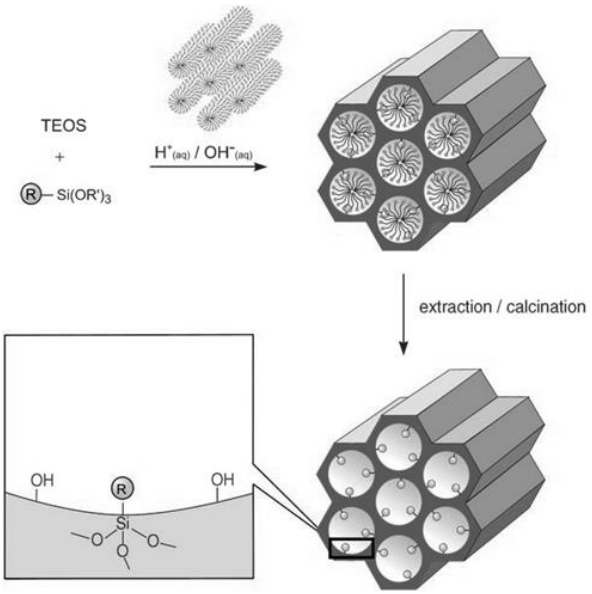

Figure 5. Co-condensation method (direct synthesis) for the organic modification of mesoporous pure silica phases. R=organic functional group. *Adapted from Angew. Chem. Int. Ed. 2006, 45, 3216. Copyright © 2006 Wiley.*

The co-condensation method enables the incorporation of a relatively high amount of functional groups. However, it is necessary to note that the presence of functional groups decorating the walls of the material also significantly influence the mechanism of interaction with the surfactant. In extreme cases, the presence of a high amount of functional groups may even prevent the formation

of the desired mesoporous structure. In addition, only suitable extractive methods can be used to remove the template in order to avoid the organic functionality destruction. Other disadvantage is the increase of homo-condensation reactions between silane groups. As a consequence, the proportion of terminal organic groups that are incorporated into the pore-wall network is generally lower than would correspond to the starting concentration in the reaction mixture.

Another way to incorporate organic compounds onto silicas is the production of *Periodic Mesoporous Organosilicas* (PMOs), but, using this method, a disordered pore system is obtained. In these materials, the organic units in this case are incorporated in the three-dimensional network structure of the silica matrix through two covalent bonds and thus distributed homogeneously in the material (Figure 6).

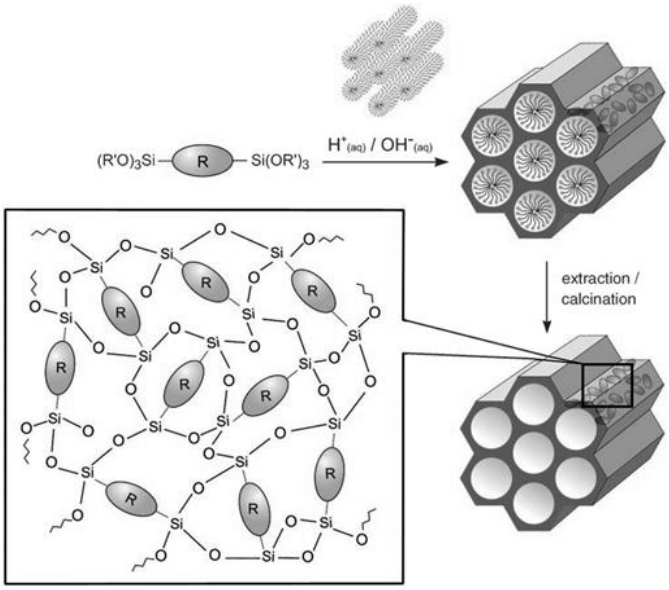

Figure 6. General synthetic pathway to PMOs that are constructed from bissilylated organic bridging units. R=organic functional group. *Adapted from Angew. Chem. Int. Ed. 2006, 45, 3216. Copyright © 2006 Wiley.*

1.2.4 Characterization of mesoporous materials

Once the hybrid material is prepared, several characterization techniques are employed to study the properties of the mesoporous architecture and to analyze the anchored organic moieties.

Regarding to the mesoporous structure, the surface area, pore size, pore volume, and, to some extent, pore shape of the material are measured using the nitrogen adsorption isotherms (amount of gas adsorbed on the solid plotted versus the relative pressure). The isotherms can be grouped into six types.[31] Within the ishoterms IV and V (porous materials), the presence of the adsorption hysteresis loops are also classified and it is widely accepted that there is a correlation between their shape and the texture (e.g., pore size distribution, pore geometry, and connectivity) of the material. The application of the Brunauer-Emmet-Teller (BET)[32] method to the adsorption isotherm is the most frequently used procedure to determine the surface area of the mesoporous systems. The pore size distribution of the mesoporous material is determined with the Barrett-Joyner Halenda (BJH)[33] method from nitrogen sorption isotherms.

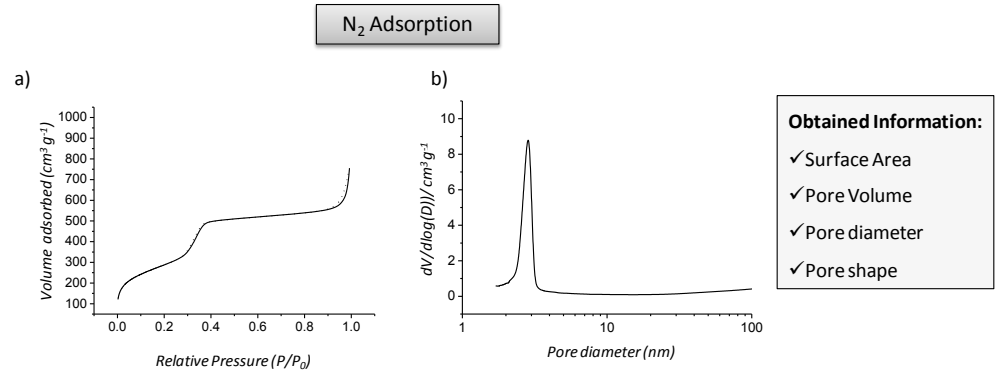

Figure 7. Typical N_2 adsorption Isotherm of MCM-41 material (a) and pore volume distribution graphic (b).

[31] K.S.W. Sing, D.H. Everett, R.A.W. Haul, L. Moscou, R.A. Pierotti, J. Rouquerol, T. Siemieniewska, *Pure & Appl. Chem.,* **1985**, *57* ,603.

[32] S. Brunauer, P.H. Emmett, T. Teller, *J. Am. Chem. Soc.*, **1938**, *60*, 309.

[33] E.P. Barrett, L.G. Joyner, P.P. Halenda, *J. Am. Chem. Soc.* **1951**, *73*, 373.

To characterize the structural properties and porous characteristics of the final materials powder X-ray diffraction (PXRD) and transmission electron microscopy (TEM) observations are commonly used. Kresge *et al.* proposed the combination of both techniques to solve the structure of the discovered M41S mesoporous supports.[14 a]

PXRD is used to study periodically ordered structures at atomic scales. In the case of the mesoporous silica materials, as amorphous materials, there are no periodic atomic planes, however the technique is useful for characterization of the ordered pore structure.

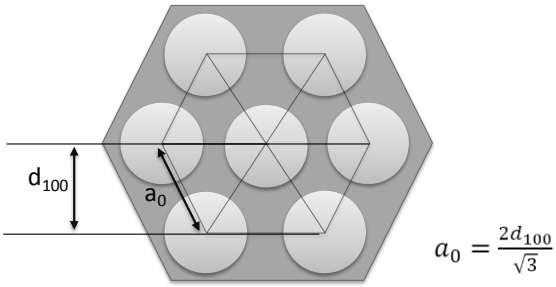

Figure 8. Schematic illustration of a hexagonal structure with the d_{100} spacing and unit cell parameter a_0.

The characteristic structural element of MCM-41 is the hexagonal packing of the mesopores (Figure 8). In PXRD experiments, this material gives reflections for low angles. As can be seen in Figure 9, a typical X-ray diffractogram of MCM-41 material shows four peaks which can be indexed as the (100), (110), (200) and (210) Bragg peaks of a *P6* space group. From the main interplanar distance d_{100}, it is possible to obtain the hexagonal structure parameter a_o through the unit cell equation. With a_o parameter and the pore diameter data (D_p), found from the adsorption isotherm, the wall thickness can be calculated.

This method implicitly assumes smooth walled mesopores, since the calculation of pore diameters from adsorption isotherms assumes an absence of micropores.

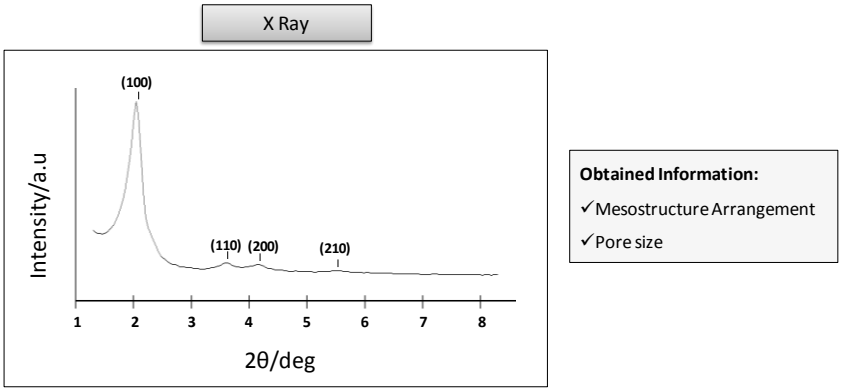

Figure 9. Powder small-angle X-ray diffractogram of MCM-41 material.

TEM microscopy is also useful to evaluate the formation of a particular phase. Figure 10 shows two examples of ordered and non-ordered mesoporous structures. As can be noted, the different mesophases can be distinguished and the shape and dimensions of the particles can be evaluated also by this technique.

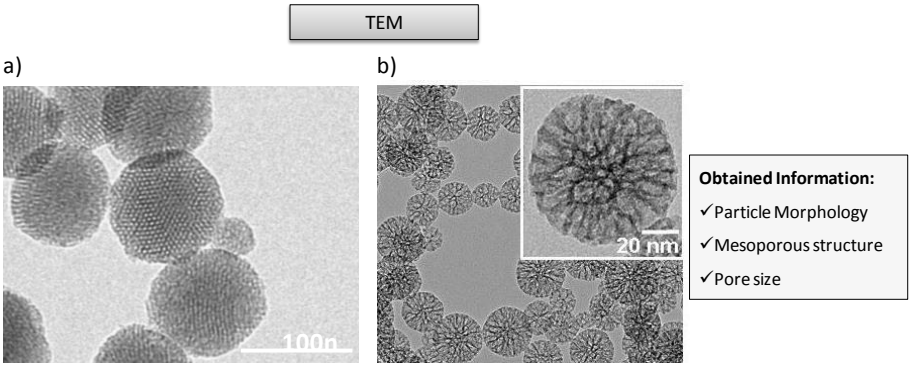

Figure 10. TEM micrographs of MCM-41 nanoparticles (a) and silica nanoparticles with a disordered distribution of mesopores (b).

In relation to the particle size, besides TEM, dynamic light scattering (DLS) can also be employed. In addition, the particle morphology can be also analyzed by using scanning electron microscopy (SEM).

The organic-inorganic ratio of the hybrid material can be evaluated with thermogravimetric (TGA) studies, elemental analysis (EA), Fourier transformed infrared spectroscopy (FT-IR), and, in some cases, by the use of scanning electron microscopy coupled with energy dispersive X-ray spectroscopy (SEM/EDX).

The characterization of both, the initial inorganic scaffold and the final hybrid material, allow verifying the preservation of the porous network after the loading and functionalization processes. In addition, besides the determination of the organic content by techniques such as EA and TGA, the decrease of the pore volume and surface area in the final material, in contrast to MCM-41 initial scaffold, is indicative of a correct pore filling and subsequent anchoring of the organic molecules on the surface.

1.2.5 Functional organic-inorganic mesoporous hybrid materials: Stimuli-responsive systems

Hybrid mesoporous silica materials are attractive for applications in several research fields. As mentioned above, these materials posses the advantageous properties of the ***inorganic scaffold*** (three dimensional structure with highly organized porosity, high surface area, high pore volume that grants high load capacity, tunable pore size, chemical inertness, thermal stability) and the possibility of modify the support with ***organic groups*** through well-known functionalization procedures, in order to obtain ***complex materials with desirable functionalities***. These hybrid organic-inorganic materials are very recently applied in several technological and scientific fields such as heterogeneous-catalysis,[34] controlled delivery of chemical species,[35] chemical and biochemical sensors[36] and environmental applications.[37]

[34] H. T. Chen , *Retrospective Theses and Dissertations*, Iowa State Univ., **2007**, Paper 15523. b) C. Y. Lai, *J Thermodyn Catal.,* **2013**, 5, 124.

[35] a) J. M. Rosenholm, E. Peuhu, L. T. Bate-Eya, J. E. Eriksson, C. Sahlgren, M. Linden, *Small,* **2010**, 6, 1234. b) M. Liong, J. Lu, M. Kovochich, T. Xia, S. G. Ruehm, A. E. Nel, F. Tamanoi, J. I. Zink, *ACS Nano*, **2008**, *2*, 889.

[36] B. J. Melde, B. J. Johnson and P. T. Charles, *Sensors*, **2008**, *8*, 5202.

One appealing concept is the development of ***stimuli-responsive*** hybrid materials, commonly reported as "***gated materials***".[38] A molecular o supramolecular-based gated material can be defined as a hybrid system in which mass transport or delivery can be triggered by a target external stimulus that controls the state of the gate (closed or open) on-command. These functional materials are formed by two subunits, a mesoporous support and certain molecular or supramolecular entities attached onto the outer surface. The mesoporous silica support act as a nanocontainer able to retain molecules in the inner of the pores. Besides, the molecular or supramolecular entities act as switchable "gate-like" moieties. The "gate-like" structures can control cargo delivery from the pores to the solution after the application of external stimuli. A schematic representation of a gate-like superstructure is shown in Figure 11.

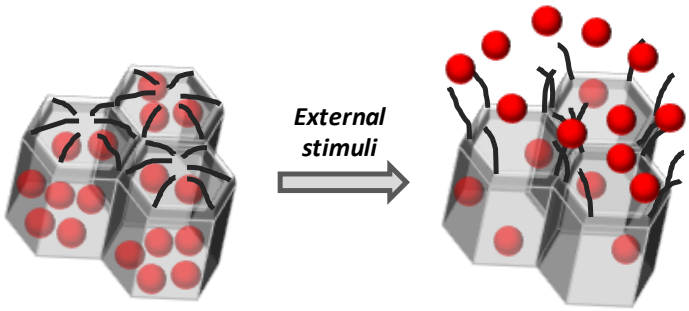

Figure 11. Schematic representation of the operation principle of a molecular gate.

Fujiwara and coworkers reported the first example of molecular gate in 2003.[39] The reported nanodevice consisted on a MCM-41 scaffold loaded with dye molecules, where the storage and release process were regulated through the photocontrolled and reversible intermolecular dimerization of coumarin derivatives attached to the pore outlets. The authors prepared MCM-41

[37] C. Coll, R. Martínez-Máñez, M. D. Marcos, F. Sancenón, J. Soto,R. K. Mahajan, *Eur. J. Inorg. Chem*., **2009,** *25*. 3770. b) S. E. Lehman, S. C. Larsen, Environ. Sci.: Nano., **2014,** *3*, 200.

[38] A. B. Descalzo, R. Martínez-Máñez, F. Sancenón, K. Hoffmann, K. Rurack, *Angew. Chem. Int. Ed.,* **2006**, *45*, 5924.

[39] a) N. K. Mal, M. Fujiwara, Y. Tanaka, Y. *Nature,* **2003**, *421*, 350. b) N. K. Mal, M. Fujiwara, Y. Tanaka, T. Taguchi, M. Matsukata, *Chem. Mater*. **2003**, *15*, 3385.

nanoparticles loaded with cholestane and externally functionalized with 7-[(3-triethoxysilyl)propoxy]coumarin, which can undergo [2+2] electrocyclic photoisomerization to give the more hindered cyclobutane derivatives upon irradiation with λ > 310 nm. The authors demonstrated that irradiation at wavelengths higher than 310 nm induced the formation of a cyclobutane derivative, which was bulkier than the starting monomers, preventing the delivery of the cargo entrapped in the pores of the scaffold. On the other hand, irradiation at 250 nm induced the cleavage of the cyclobutane dimer with subsequent cholestane release (see Figure 12).

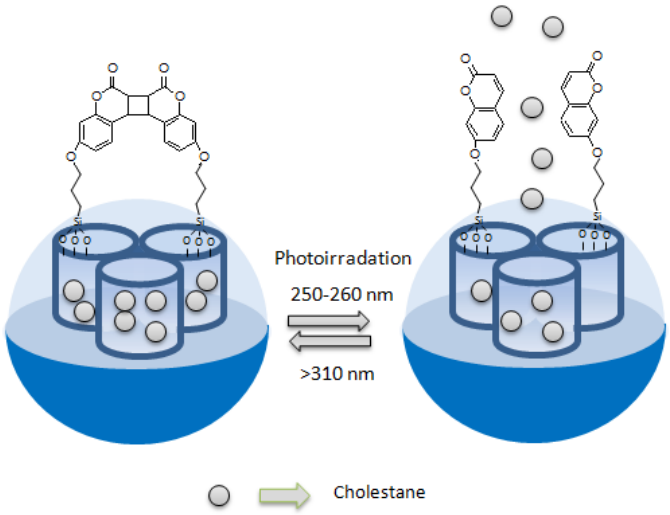

Figure 12. Schematic representation of a light-driven molecular gate. Coumarin fotoisomerization reaction (λ > 310 nm) induced the formation of a cyclobutane dimer that inhibit cargo release. Irradiation with UV light (250-260 nm) induced the photo-opening of cyclobutane ring with the subsequent cargo delivery

Since this pioneering example, numerous nanoscopic gated systems using mesoporous hybrid scaffoldings have been described. For example, inorganic nanoparticles,[40] polymers,[41] and larger supramolecular assemblies[42] have been

[40] a) C.-Y. Lai, B. G. Trewyn, D. M. Jeftinija, K. Jeftinija, S. Xu, S. Jeftinija, V. S.-Y. Lin, *J. Am. Chem. Soc.*, **2003**, *125*, 4451. b) S. Giri, B. G. Trewyn, M. P. Stellmaker, V. S.-Y. Lin, *Angew. Chem., Int. Ed.,* **2005**, *44*, 5038. c) E. Aznar, M . D. Marcos, R. Martinez-Manez, F. Sancenon, J. Soto, P. Amoros, P. Guillem, J. *Am. Chem. Soc.,* **2009**, *131*, 6833. d) J. L. Vivero- Escoto, I. I. Slowing, C. Wu, V. S.-Y. Lin, *J.Am. Chem. Soc.,* **2009**, *131*, 3462.

used as blocking caps that controls the opening/closing of pore entrances in mesoporous scaffolds. On the other hand, different stimuli, such as pH,[43] light,[44] redox potential,[45] temperature[46] and target molecules[47] have been applied as "triggers" for uncapping the pores and releasing guest molecules from mesoporous scaffolds.

In addition, in the last years, the design of stimuli-responsive gated systems involving biomolecules has attracted much attention. As it is shown in the next section enzymes[48] have been used as stimuli to uncap the gated-scaffolds,

---

[41] a) R. Liu, X. Zhao, T. Wu., P. Y. Feng, *J. Am. Chem. Soc.*, **2008**, *130*, 14418. b) C. L. Zhu, X. Y. Song, W. H. Zhou, H. H. Yang, X. R. Wang, *J. Mater. Chem.,* **2009**, *19*, 7765.

[42] a) T. D. Nguyen, Y. Liu, S. Saha, K. C. F. Leung, J. F. Stoddart, J. I. Zink, *J. Am. Chem. Soc.,* **2007**, *129*, 626. b) R. Liu, Y. Zhang, P. Y. Feng, *J. Am. Chem. Soc.,* **2009**, *131*, 15128.

[43] a) R. Casasus, M. D. Marcos, R. Martínez-Máñez, J. V. Ros-Lis, J. Soto, L. A. Villaescusa, P. Amorós, D. Beltrán, C. Guillem, J. Latorre, *J. Am. Chem. Soc.,* **2004**, *126*, 8612. b) A. Bernardos, E. Aznar, C. Coll, R. Martínez-Máñez, J. M. Barat, M. D. Marcos, F. Sancenón, J. Soto, *J. Control. Rel.,* **2008**, *131*, 181. c) Q.Yang, S. Wang, P. Fan, L. Wang, Y. Di, K. Lin, F.–S. Xiao, *Chem. Mater., 2005*, *17*, 5999. d) V. Cauda, C. Argyo, A. Schlossbauer, T. J. Bein, *J. Mater. Chem.,* **2010**, *20*, 4305. e) S. Angelos, Y.–W. Yang, K. Patel, J. F. Stoddart, J. I. Zink, *Angew. Chem. Int. Ed.,* **2008**, *47*, 2222. f) H. Meng, M. Xue, T. Xia, Y. –L. Zhao, F. Tamanoi, J. F. Stoddart, J. I. Zink, E. A. Nel, *J. Am. Chem. Soc.,* **2010**, *132*, 12690.

[44] a) E. Johansson, E. Choi, S. Angelos, M. Liong, J. I. Zink, *Sol-Gel Sci. Technol.,* **2008**, *46*, 313. b) Q. Lin, Q. Huang, C. Li, C. Bao, Z. Liu, F. Li, L. Zhu, L. *J. Am. Chem. Soc.,* **2010**, *132*, 10645. c) J. Lai, X. Mu, Y. Xu, X. Wu, C. Wu, C. Li, J. Chen, Y. Zhao, *Chem. Commun.,* **2010**, *46*, 7370.

[45] a) R. Hernandez, H. –R. Tseng, J. W. Wong, J. F. Stoddart, J. I. Zink, *J. Am. Chem. Soc.,* **2004**, *126*, 3370. b) R. Liu, X. Zhao, T. Wu, P. Feng, *J. Am. Chem. Soc.,* **2008**, *130*, 14418. c) R. Mortera, J. Vivero-Escoto, I. I. Slowing, E. Garrone, B. Onida, V. S.-Y. Lin, *Chem. Commun.,* **2009**, 3219.

[46] a) C. Liu, J. Guo, W. Yang, J. Hu, C. Wang, S. Fu, *J. Mat. Chem.,* **2009**, *19*, 4764. b) C. Chen, J. Geng, F. Pu, X. Yang, J. Ren, X. Qu, *Angew. Chem. Int. Ed.* **2011**, *50*, 882.

[47] a) R. Casasús, E. Climent, M. D. Marcos, R. Martínez-Máñez, F. Sancenón, J. Soto, P. Amorós, J. Cano, E. Ruiz, *J. Am. Chem. Soc.,* **2008**, *130*, 1903. b) E. Aznar, C. Coll, M. D. Marcos, R. Martínez-Máñez, F. Sancenón, J. Soto, P. Amorós, J. Cano, E. Ruiz, *Chem. Eur. J.,* **2009**, *15*, 6877. c) Y. Zhao, B. G. Trewyn, I. I. Slowing, V. S.-Y. Lin, *J. Am. Chem. Soc.,* **2009**, *131*, 8398. d) Y. L. Choi, J. Jaworsky, M. L. Seo, S. J. Lee, J. H. Jung, *J. Mater. Chem.,* **2011**, *21*, 7882.

[48] a) K. Patel, S. Angelos, W. R. Dichtel, A. Coskun, Y. –W. Yang, J. I. Zink, J. F. Stoddart, *J. Am. Chem. Soc.,* **2008**, *130*, 2382. b) A. Schlossbauer, J. Kecht, T. Bein, *Angew. Chem. Int. Ed.,* **2009**, *48*, 3092. c) C. Park, H. Kim, S. Kim, C. Kim, *J. Am. Chem. Soc.,* **2009**, *131*, 16614. d) P. D. Thornton, A. Heise, *J. Am. Chem. Soc.,* **2010**, *132*, 2024.

whereas other biomolecules such as sachharides,[49] peptides,[50] aptamers[51] or DNA[52] have been reported as capping molecules.

Moreover, very recently, gated materials have been applied in recognition and sensing protocols.[53] Several works reported the use of MSN as a carrier system loaded with a dye (for instance rhodamine, Rh) and capped with gate-like entities designed to be opened and release the cargo only in the presence of a target analyte. One selected example is the work reported by Martínez-Máñez *et al.* in which a novel aptamer-capped material for the fluorometric detection of α-thrombin was prepared (see Figure 13).[54] In vitro studies showed a limit of detection of 2 nM for α-thrombin and its accurate detection in human serum diluted with PBS.

[49] A. Bernardos, L. Mondragón, E. Aznar, M. D. Marcos, R. Martínez-Máñez, F. Sancenón, J. Soto, J. M. Barat, E. Pérez-Payá, C. Guillem, P. Amorós, *ACS Nano,* **2010**, *4*, 6353.

[50] a) C. Coll, L. Mondragón, R. Martínez-Máñez, F. Sancenón, M. D. Marcos, J. Soto, P. Amorós, E. Pérez-Payá, Angew. *Chem. Int. Ed.,* **2011,** *50,* 2138. b) F. Porta, G. E. M. Lamers, J. I. Zink, A. Kros, *Phys. Chem. Chem. Phys.,* **2011**, *13*, 9982.

[51] a) C. -L. Zhu, C. –H. Lu, X. –Y. Song, H. –H. Yang, X. –R. Wang, *J. Am. Chem. Soc.,* **2011**, *133*, 1278. b) V. C. Özalp, T. Schäfer, *Chem. Eur. J.,* **2011**, *17*, 9893.

[52] c) A. Schossbauer, S. Warncke, P. M. E. Gramlich, J. Kecht, A. Manetto, T. Carell, T. Bein, *Angew. Chem.Int. Ed.,* **2010**, *49*, 4734. d) Y. Zhang, Q. Yuan, T. Chen, X. Zhang, Y. Chen, W. Tan, *Anal. Chem.,* **2012**, *84*, 1956.

[53] a) R. Casasús, E. Aznar, M. D. Marcos, R. Martínez-Máñez, F. Sancenón, J. Soto, P. Amorós, *Angew. Chem.Int. Ed.,* **2006**, *45*, 6661. b) C. Coll, R. Casasús, E. Aznar, M. D. Marcos, R. Martínez-Máñez, F. Sancenón, J. Soto, P. Amorós, *Chem. Commun.,* **2007**, 1957. c) C. Coll, A. Bernardos, R. Martínez-Máñez, F. Sancenón, *Acc. Chem. Res.*, **2013**, *46*, 339. d) L. Pascual, I. Baroja, E. Aznar, F. Sancenon, M. D. Marcos, J. R. Murguia, P. Amoros, K. Rurack, R. Martinez-Manez, *Chemical Communications*, **2015**, *51*, 1414.

[54] M. Oroval, E. Climent, C. Coll, R. Eritja, A. Aviño, M. D. Marcos, F. Sancenón, R. Martínez-Máñez and P. Amorós, *Chem. Commun*., **2013**, *49*, 5480.

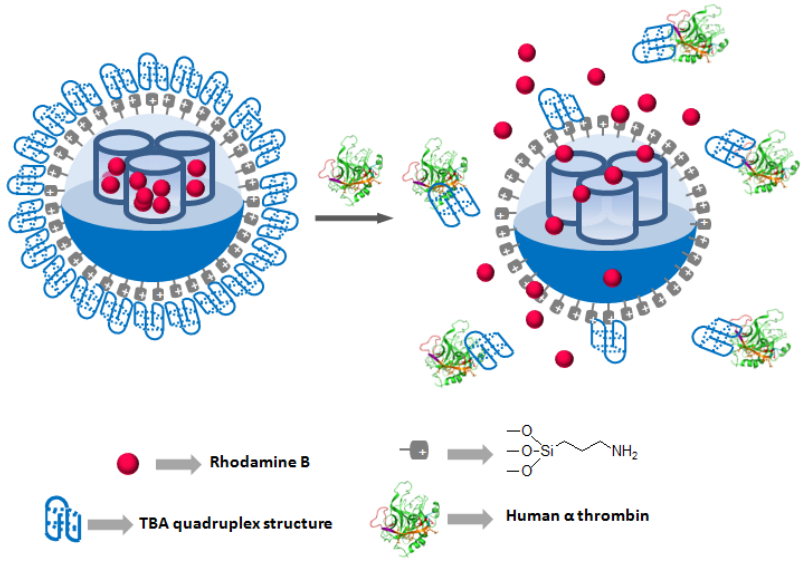

Figure 13. Schematic representation of the gated material capped with a TBA aptamer in the quadruplex state. The delivery of the entrapped guest is observed in the presence of α-thrombin. Adapted from *Chem. Commun.*, 2013, 49, 5480. *Copyright ©Royal Society of Chemistry*

Another potential use of stimuli-responsive materials is their application in the field of nanomedicine as drug delivery systems. In this case the mesoporous scaffold is able to enclose and protect hydrophobic and hydrophilic drugs during their transport, overcoming common issues such as poor solubility and stability of drugs or undesired side effects. In addition, surface functionalization with specific targeting moieties allows these nanodevices to gain selectivity towards specific cells types while sparing normal tissues. In order to do that, specific biomolecules whose receptors are overexpressed in the target cells can be anchored to the nanoparticles' surface.

The next section of the introduction is focused in critical aspects of gated materials to be considered in order to apply them in delivery protocols (of drugs or therapeutic agents) which can be used in innovative treatments for a wide variety of diseases.

1.3 **Gated nanoparticles as drug delivery systems (DDS)**

The development of innovative drug delivery strategies is a fundamental part of medicine and, in this context, nanotechnology will surely play an important role in the design of advanced therapies in a near future. Functional nanomaterials have the potential to dramatically improve the efficacy of therapeutic approaches. Consequently, during the past two decades a wide range of drug delivery systems (DDS) has been designed. DDS are usually based in liposomes,[55] micelles,[56] nanoemulsions,[57] nanoparticulated systems[58,59,60] and dendrimers,[61] which contains encapsulated, dispersed, adsorbed or conjugated, drugs and/or imaging agents.

The advantage of these advanced formulations is the possibility to design smart nanodevices able to control the rate, the exact time when the drug is delivered (i.e. time-release dosage) and to target specific areas of the body. These properties allow avoiding typical problems derived from the use of certain drugs:

- Poor selectivity, which is traduced in undesired side effects such multidrug resistance (MDR) and damage in normal tissues
- High drug concentration and dosing frequency
- Poor solubility
- Limited stability
- Rapid metabolization and excretion of the drug

Moreover, a large number of drugs currently being used would be improved if they were more efficiently delivered through appropriate application of

[55] Y. Malam, M. Loizidou, A.M. Seifalian, *Trends Pharmacol Sci.*, **2009**, *30*, 592.

[56] E. Blanco, C.W. Kessinger, B.D. Sumer, J. Gao, *Exp Biol Med (Maywood).,* **2009**, *234*, 123.

[57] M. Jaiswal , R. Dudhe , P. K. Sharma, *3 Biotech,* **2015***, 5,* 123.

[58] Z. Liu, Y. Jiao, Y. Wang, C. Zhou, Z. Zhang, *Adv Drug Deliv Rev.*, **2008**, *60*, 1650.

[59] P. Ghosh, G. Han, M. De, C.K. Kim, V.M. Rotello, *Adv Drug Deliv Rev*., **2008**, *60*, 1307.

[60] P. Yang, S. Gai, J. Lin, *Chem Soc Rev.,* **2012,** *41*,3679.

[61] B.K. Nanjwade,H.M. Bechra, G.K. Derkar, F.V. Manvi, V.K. Nanjwade, *Eur J. Pharm Sci.,* **2009**, *38*, 185.

nanotechnologies. As an example, more than 40% of substances discovered through combinatorial screening programs have poor solubility in water and therefore of limited use.[62]

Stimuli-responsive MSN are good candidates as drug delivery vehicles. On one hand, the properties of the material guarantee the efficient encapsulation and protection of the loaded drugs. On the other, the suitable decoration of nanoparticle surface with functionalities such as hydrophilic polymers, gate-keepers, targeting ligands, etc. yield multifunctional nanodelivery systems able to combine targeted drug delivery, disease diagnosis and molecular imaging actions (see Figure 14). These resulting theranostic nanodevices are expected to play a significant role in the dawning era of personalized medicine.[63]

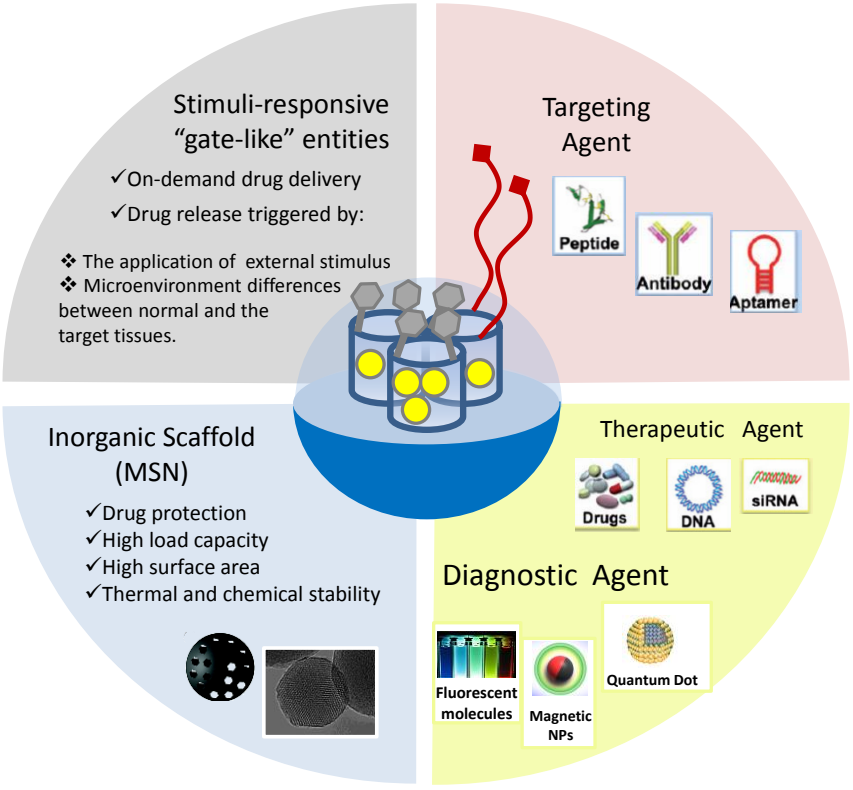

Figure 14. Schematic representation of multifunctional stimuli-responsive MSN components

[62] E.M. Merisko-Liversidge, G.G. Liversidge, *Toxicol. Pathol.,* **2008**, *36* 43.

[63] J. Xie , S. Lee , X. Chen, *Adv Drug Deliv Rev.,* **2010,** *62*, 1064.

The decoration of nanoparticle surface with stimuli-responsive "gate-like" entities allows designing drug delivery MSN able to release their payload under specific conditions. In addition, the immobilization of ligands on MSN surface, which recognize target cell -specific receptors, allow to achieve the targeted delivery and ensure the cellular uptake effectively. The incorporation of optical labeling or other detectable tracers allows the direct visualization of the delivery and their application as diagnostic tool.

1.3.1 Loading, transport and release of active molecules

MSN used as host systems for therapeutics provide high loading capacity and for instance MSN have been reported to store and transport hydrophobic molecules, antitumor drugs, enzymes, oligonucleotides or plasmids through biological media. These nanodevices prevent the premature release of guest entities, protect healthy tissues from toxic drugs and avoid the premature decomposition of drugs and biomolecules in certain environments.

Usually, the encapsulation of drugs and small biomolecules within the pores of MSN is carried out by physical adsorption from solution. The optimal solvent is chosen in terms of drug solubility and to facilitate pore wall-drug over solvent-drug interactions. The isoelectric point of the surface silanol groups is about 2–3. Therefore, electrostatic adsorption of positively charged molecules is an attractive method for incorporating water-soluble cargo into siliceous MSN. The loading of negatively charged molecules and hydrophobic drugs is typically carried out through the adsorption from organic solvents followed by vacuum drying in order to remove the solvent. The loading process performed in non-aqueous media allows avoiding repulsive forces between the drug and the pores walls due to electrostatic interactions and pH-dependencies. In addition, the textural properties of the mesoporous material determine the adsorption process. The pore properties limit the size of the molecule that can be adsorbed into the mesopores, whereas the surface area and the pore volume of the material are determining factors for the amount of adsorbed drug.[22 a]

Gate-keepers anchored on the external surface of the loaded particles inhibited the premature release of the entrapped drug but also allowed its spatio-temporal release upon the application of an external stimuli or when changes in one or more chemical features of the biological environment (in which the nanodevices are used) are produced. The next sections show several examples of gated nanoparticles that are able to release an entrapped cargo upon application of certain stimuli.

✓ *EXTERNAL STIMULI*

External stimuli are based on extracorporeal physical alterations, including temperature changes, application of magnetic fields, ultrasounds, as well as UV-vis (λ = 240-639 nm) and IR light (λ = 808 nm). This class of triggers confers a great control over the temporal and spatial release conditions into the targeted tissue or cells. However, the *in vivo* application of these triggers, as in the case of light stimuli, is limited by their tissue penetration ability.

A large variety of ***photoresponsive*** systems has been engineered in the past few years to achieve on-demand drug release in response to illumination of a specific wavelength. These systems take advantage of: (i) photodimerizations, *cis-trans* photoconversions; (ii) photocleavage of chemical bonds directly or assisted by photosensitizers; or (iii) photoinduced heating of gold nanoparticles to control mass transport from pore voids to a solution.

As an example, Zhao *et al.*[64] reported a light-responsive nanogated ensemble based on polymer grafted mesoporous hybrid nanoparticles. MSN were first loaded with fluorescein dye. The amine-terminated poly(*N*-isopropylacrylamide-*co*-2-nitrobenzyl acrylate) ((poly(NIPAMNBAE)) polymer, which contained photocleavable 2-nitrobenzyl groups, was coupled to a 3-(triethoxysilyl)propyl isocyanate, and then grafted to the pore outlet of MSN. The poly(NIPAMNBAE)

[64] J. P. Lai, X. Mu, Y. Y. Xu, X. L. Wu, C. L. Wu, C. Li, J. B. Chen, Y. B. Zhao, *Chem. Commun.,* **2010**, *46*, 7370.

polymer had a lower critical solution temperature (LCST) below the environmental temperature and was in a collapsed (insoluble) state, which inhibited cargo delivery. Upon UV irradiation (310 nm), the hydrophobic 2-nitrobenzyl acrylate moiety was photolysed into hydrophilic acrylate. As a consequence, the polymers changed to their coil (soluble) conformation and the gate was opened thereby allowing the entrapped molecules to escape (Figure 15).

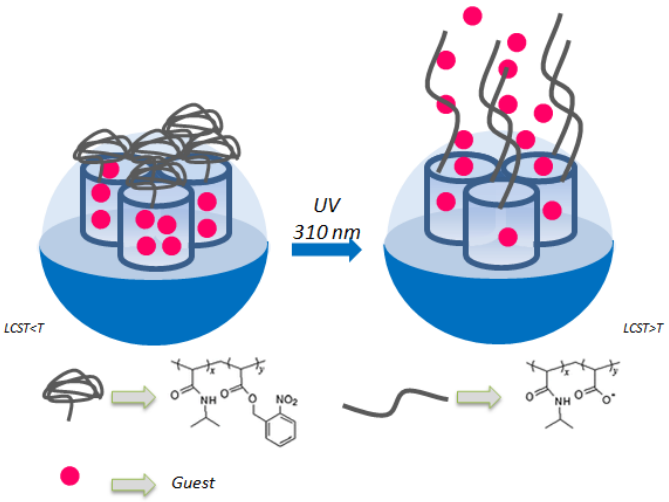

Figure 15. Light-responsive nanogated ensemble based on polymer grafted mesoporous silica.

Other example of light-driven controlled release system was reported by Yan and coworkers.[65] These authors developed a gated system based on azobenzene-modified nucleic acids as gate-like units. As the most popular phototransformable molecules, azobenzene and its derivatives can undergo reversible isomerization from the *trans* to *cis* forms under irradiation at 300–380 nm and from *cis* to *trans* using light at wavelengths > 400 nm. MSN were loaded with Rh 6G dye and functionalized with propyl isocyanate groups, which further reacted with amino-modified single-stranded DNA arms (arm-DNA). In a second step azo-DNA strands, which contained azobenzene moieties and segments complementary to the arm-DNA, were used to cap pores as can be seen in Figure 16. Under visible light

[65] Q. Yuan, Y. F. Zhang, T. Chen, D. Q. Lu, Z. L. Zhao, X. B. Zhang, Z. X. Li, C. H. Yan, W. H. Tan, *ACS Nano.,* **2012**, *6*, 6337.

irradiation (λ = 450 nm), azobenzene molecules were in the *trans* form and azo-DNA was hybridized with arm-DNA capping the pores. However, upon UV irradiation (λ = 365 nm), azobenzenes turned to the *cis* form, which induced dehybridization and pore opening with the subsequent Rh 6G release. These DNA/mesoporous silica hybrid nanostructures were also exploited as carriers for the cancer cell chemotherapy drug doxorubicin (DOX) in human acute lymphoblastic leukemic CCRF-CEM cells and human lung adenocarcinoma A549 cells, due to its stimuli-responsive property as well as good biocompatibility. Cells were treated with DOX-loaded azo-DNA MSN of different concentrations and, without UV light treatment, no cytotoxicity to both CEM cells and A549 cells was detected. After UV irradiation particles showed dose-dependent cytotoxicity in both cell lines.

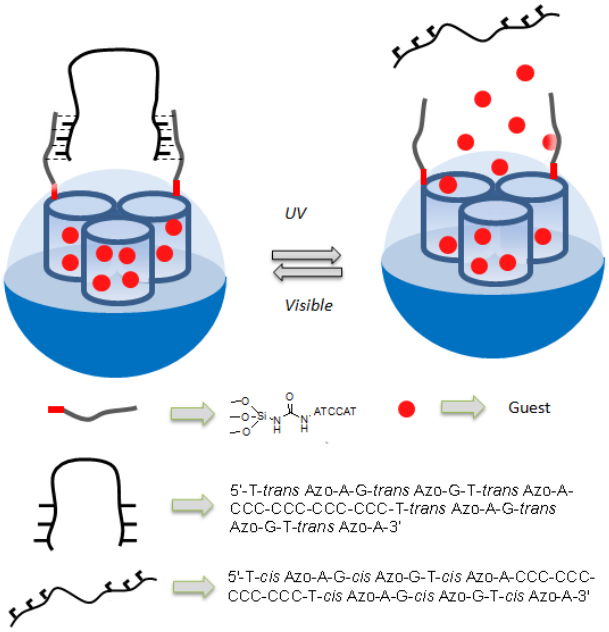

Figure 16. MSN loaded with Rh 6G or DOX and capped with an azobenzene derivatized-DNA strand. Cargo was released upon irradiation at 365 nm.

As it was commented above, the main drawback of light-triggered drug delivery is the low penetration depth (~10 mm) that results from the strong scattering properties of soft tissues in the ultraviolet–visible region of the spectrum. For this

reason, in recent years, researchers have focused their attention on developing more bio-applicable systems by using photosensitive groups that respond to higher wavelengths or exploiting two-photon technology.[66] These novel systems allow replacing the ultraviolet–visible light source by a NIR laser (700–1,000 nm range) with deeper tissue penetration, lower scattering properties and minimal harm to tissues.

Thermosensitive drug delivery is among the most investigated stimuli-responsive strategies, and has been widely explored in oncology. Most of these capped materials use thermosensitive polymers that are able to deliver cargo after a temperature-dependent phase transition. Some other interesting examples, involve melting ds-DNA sequences,[67] or also melting other organic coatings such as paraffins.[68] Ideally, thermosensitive nanocarriers should retain their load at body temperature (~37 °C), and deliver the drug within a locally heated area.

Aznar and coworkers prepared a family of paraffin-capped MSN as thermoresponsive-driven hybrid systems.[65] In a first step, MSN were loaded with safranine-O dye and then functionalized on the external surface with octadecyltrimethoxysilane to render them sufficiently hydrophobic to cap the system with selected paraffins. In a second step, different solids capped with heneicosane, docosane and tetracosane were prepared. These paraffins, with melting points of 39, 42 and 49 ^{o}C respectively, were able to form a hydrophobic layer around the pore outlets that inhibits cargo release. An increase of the temperature above the paraffin melting point resulted in the release of the entrapped guest. Moreover, heneicosane-capped nanoparticles were able to release safranine O in HeLa cells when incubation was carried out at temperatures

[66] J. Croissant, A. Chaix, O. Mongin, M. Wang, S. Clement, L. Raehm, J.-O. Durand, V. Hugues, M. Blanchard-Desce, M. Maynadier, *Small*, **2014,** *10*, 1752.

[67] a) A. Schlossbauer, S. Warncke, P. M. E. Gramlich, J. Kecht, A. Manetto, T. Carell, T. Bein, *Angew. Chem. Int. Ed.* **2010**, *49*, 4734. b) C. Chen, J. Geng, F. Pu, X. Yang, J. Ren, X. Qu, *Angew. Chem. Int. Ed.* **2011**, *50*, 882. c) Z. Z. Yu, N. Li, P. P. Zheng, W. Pan, B. Tang, *Chem. Commun.* **2014**, *50*, 3494.

[68] E. Aznar, L. Mondragón, J. V. Ros-Lis, F. Sancenón, M. D. Marcos, R. Martínez-Máñez, J. Soto, E. Pérez-Payá, P. Amorós, *Angew. Chem. Int. Ed.,* **2011**, *50*, 11172.

above 39 °C. Heneicosane-capped nanoparticles were also loaded with DOX and used to release this chemotherapeutic agent in HeLa cells after heating. A schematic mechanism of the function of these temperature-responsive systems is depicted in Figure 17.

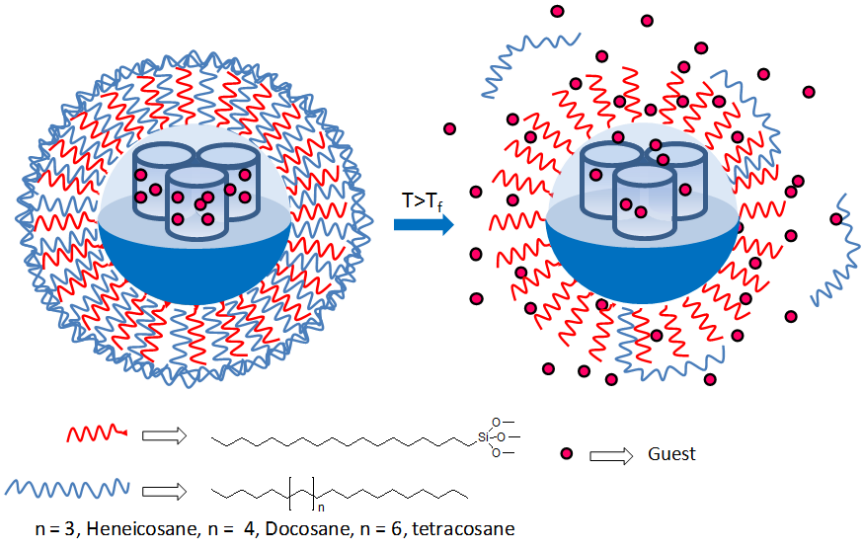

Figure 17. Schematic representation of the gated material functionalized with octadecyltrimethoxysilane and capped with paraffins. The delivery of the entrapped guest (safranine O) is triggered when temperature rises above paraffin melting point. Adapted from *Angew. Chem. Int. Ed.,* **2011**, *50***,** 11172. Copyright © 2011 WILEY-VCH Verlag GmbH & Co. KGaA, Weinheim.

Within external stimuli, ***ultrasounds and magnetic fields*** are commonly used for on-command controlled delivery. These techniques are non-invasive, can penetrate depth in tissues and can be carefully controlled by changing frequency, power, cycles and time of application. Magnetic guidance is typically obtained by focusing an extracorporeal magnetic field on the biological target during the injection of a magnetically responsive nanocarrier.[69] Moreover, there is the possibility of performing magnetic resonance imaging, and hence to associate diagnostics and therapy within a single system (the so-called theranostic approach). Furthermore, the application of an oscillating magnetic field is able to generate localized heating when it is applied over magnetic nanocrystals. This

[69] L. Zhang, T. Wang, L. Yang, C. Liu, C. Wang, H. Liu, Y.A. Wang, Z. Su, *Chemistry*, **2012,** *18*, 12512.

concept has been exploited to develop nanodevices that combine cytotoxic drugs therapy with the effect of localized heating (hyperthermia).

As an example, Zink *et al.* [70] reported a gated material that incorporates zinc-doped iron oxide nanocrystals within a mesoporous silica framework. MSN with a zinc-doped iron oxide core were loaded with Rh B dye or the cytotoxic drug DOX, and then the external surface was modified with *N*-(6-*N*-aminohexyl) aminomethyltriethoxysilane. Finally, pores were capped by adding cucurbit[6]uril, which interacted with the aminated stalks to seal pores (see Figure 18). Upon application of an alternating magnetic field (AMF) the nanocrystals generate local internal heating, causing the molecular machines to disassemble and allowing the cargos to be released. Finally, these authors assessed that gated nanoparticles were endocytosed by the MDA-MB-231 breast cancer cell line. When cells were treated with unloaded material, in the presence of an AMF the local heating caused by the magnetic cores induced only 16% of cells to die. However, cells treated with DOX-loaded material showed significant higher levels of death in the presence of AFM.

[70] C. R. Thomas, D. P. Ferris, J. H. Lee, E. Choi, M. H. Cho, E. S. Kim, J. F. Stoddart, J. S. Shin, J. Cheon, J. I. Zink, *J. Am. Chem. Soc.* **2010**, *132*, 10623.

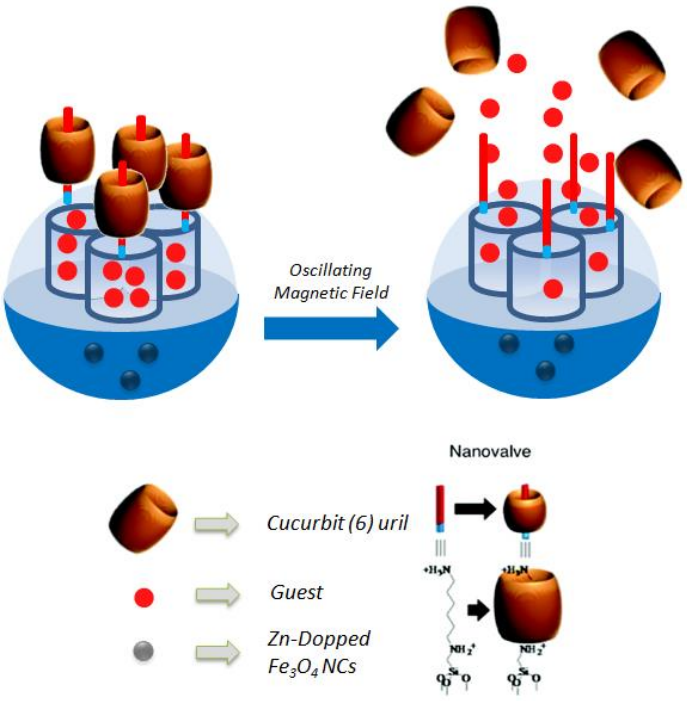

Figure 18. Scheme of a nanogated ensemble that is opened upon application of a magnetic field. Remote heating via the introduction of an oscillating magnetic field triggers the opening of nanovalves and guest is released.

Ultrasounds (US) also represent an effective method for attaining spatio-temporal control of drug release at the desired site, thus preventing harmful side effects to healthy tissues. Ultrasound waves can trigger the release of the drug through the thermal and/or mechanical effects generated by cavitation phenomena or radiation forces.

As an example, Chen, Shi *et al.*[71] reported a multifunctional system based on hollow MSN for high intensity focused ultrasound (HIFU) therapy. To prepare the gated materials the authors loaded the pores of hollow MSN with pyrene and perfulorohexane (PFH). Then capped the pores with gold nanoparticles (AuNPs) and, finally, functionalized the external surface of the capping agent with thiol-functional polyethylene glycol (PEG) molecules (see Figure 19). Application of

[71] X. Wang, H. Chen, Y. Zheng, M. Ma, Y. Chen, K. Zhang, D. Zeng, J. Shi, *Biomaterials*, **2013**, *34*, 2057.

ordinary US irradiation triggered the release of the loaded drug through the alteration of acoustic and thermal properties of the attached AuNPs. Moreover, the irradiation of the nanocarrier with US converted PFH nanoemulsion into microbubbles. The bubbles, formed through acoustic droplet vaporization, promoted the appearance of cavitations which, in turn, also conferred the nanomaterial with contrast-intensified US imaging properties. US-guided HIFU therapy *ex vivo* and *in vivo* with the nanomaterial was found to be highly efficient on rabbit VX2 xenograft tumor ablation due to the high thermal energy accumulation and increased mechanical/thermal effects. The system induced significant cytoclasis and enhanced drug release, served as contrast-intensified US imaging agent and enabled efficient US-guided HIFU tumor ablation therapy.

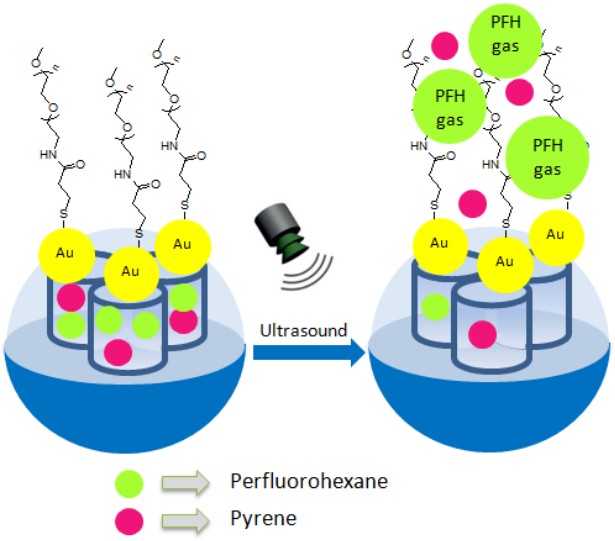

Figure 19. Hollow MSN loaded with pyrene and PFH, and capped with PEG-AuNPs. Cargo delivery was observed upon ultrasound irradiation.

✓ *INTERNAL STIMULI*

Internal stimulus arises from the microenvironment differences between normal and target tissues. Endogenous stimuli such as difference in pH, change in redox potential, reaction with some molecules or an increased level of certain enzymes

are used to trigger the delivery of species from nanoscale gated devices. This trigger mechanism allows designing on-demand drug delivery systems able to recognize their microenvironment and react in a dynamic way, mimicking the responsiveness of living organisms.

Redox-responsive molecular gates have been widely studied as drug delivery systems. The presence of reducing agents found at the intracellular level makes redox sensitive nanodevices suitable to deliver molecules within the cells. In addition, an increase in the concentration of redox-active species has been directly related with some diseases such as cancer. Due to the wide bio-applicability of redox-responsive capped systems, a large number of examples have been described during the last decade in this area, and they can be summarized into two main fundamental groups: (i) systems based in the reduction and consequent breakage of disulfide bonds (that linked the capping molecule to the mesoporous scaffold) or (ii) systems where the movement of certain capping molecules, via the oxidation/reduction of suitable groups, induced cargo release.

One of the first redox-driven capped materials was presented in 2003 by Lin and coworkers. The reported system was based on MSN loaded with bioactive molecules (vancomycin or Adenosine triphosphate **(**ATP)) and capped with CdS nanocrystals through a disulfide linker.[72] To prepare the gated material, MSN modified with mercaptopropyl groups were synthesized via a co-condensation method. Then the external surface was functionalized with 2-(pyridyldisulfanyl)ethylamine to obtain the linker 2-(propyldisulfanyl)ethylamine. Finally, the material was loaded and then MSN were capped with mercaptoacetic acid-coated CdS nanocrystals via an amidation reaction The addition of reductors, such as dithiotheritol (DTT) or mercaptoethanol (ME), induced the breaking of the disulfide bridges that linked the CdS nanoparticles with the hybrid materials, with the subsequent uncapping and cargo release (Figure 20). The biocompatibility and

[72] C. Y. Lai, B. G. Trewyn, D. M. Jeftinija, K. Jeftinija, S. Xu, S. Jeftinija, V. S. Y. Lin, *J. Am. Chem. Soc.* **2003**, *125*, 4451.

delivery efficiency of MSN with neuroglial cells (astrocytes) were tested. Astrocytes cultured in the presence of CdS-capped MSN with ATP molecules encapsulated inside the pores significantly increased intracellular Ca^{2+}, which indicated that the ATP molecules released from the nanomaterial reached their receptors on the cell surface and triggered the corresponding ATP receptor-mediated increase in the intracellular calcium concentration. No changes in intracellular calcium were detected in the astrocytes incubated in the presence of CdS-capped MSN without encapsulated ATP.

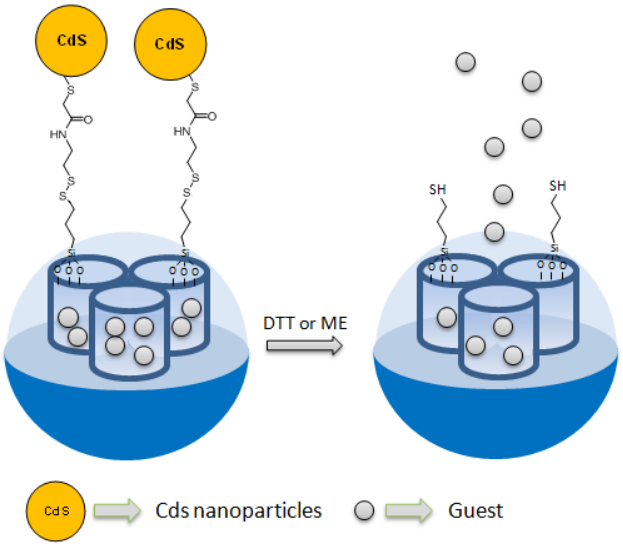

Figure 20. Delivery of vancomycin or ATP from CdS-capped MSN due to the cleavage of disulfide bonds in the presence of reducing agents.

The stabilization/destabilization of supramolecular complexes via the oxidation/reduction of suitable groups is one of the fundamental approaches used in redox-responsive gated materials. The supramolecular systems that better fit with this paradigm are rotaxanes and pseudo-rotaxanes.

One of the first examples of controlled delivery systems based on the use of a pseudo-rodaxane as molecular gate was reported by Stoddart and coworkers.[45a] These authors prepared MSN loaded with an iridium complex dye and

functionalized the surface with a 1,5-dioxynaphtalene derivative (DNPD). Pores were capped by the formation of an inclusion complex between the DNP derivative and cyclobis-(paraquat-*p*-phenylene) $CBPQT^{4+}$. The addition of a reductive agent ($NaCNBH_3$) resulted in the rupture of the complex and the release of the entrapped dye (Figure 21).

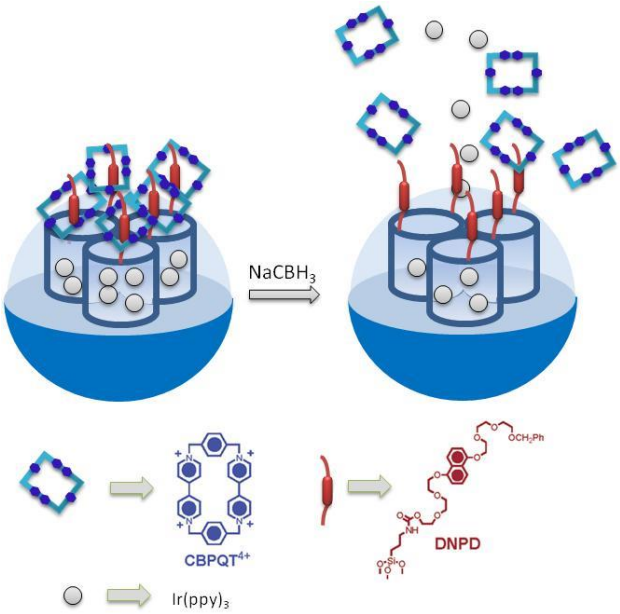

Figure 21. Schematic representation of the operation of redox nanovalves due to the destabilization of the supramolecular complex produced between $CBPQT^{4+}$ and DNPD.

Since the first example of pH-driven molecular gate reported by R. Martínez-Máñez and coworkers in 2004,[43a] ***pH-responsive*** nanodevices have been widely described as drugs delivery systems. Variations in pH have been exploited for the delivery of drugs to treat specific organs (such as vagina[73]), to achieve an intracellular delivery of molecules as well as to trigger the release of drugs when subtle environmental changes associated with pathological situations, such as cancer or inflammation, takes place.[74]

[73] N. Mas, I. Galiana, S. Hurtado, L. Mondragón, A. Bernardos, F. Sancenón, M.D. Marcos, P. Amorós, N. Abril-Utrillas, R. Martínez-Máñez, J.R. Murguía, *Int. J. Nanomedicine*, **2014**, *9*, 2597.

[74] S. Mura, J. Nicolas, P. Couvreur, *Nature Materials*, **2013**, *12*, 991

For example, there are large number of nanodevices for the targeted delivery of anticancer drugs that have taken advantage of the slight difference in pH between healthy tissues and the extracellular environment of solid tumours. While the intracellular pH of cells within healthy tissues and tumors is similar, the extracellular pH of normal tissues and blood is around 7.4, whereas the average extracellular tumor pH is between 6.0 and 7.0, which is mainly caused by high glycolysis rate and high level of CO_2.[75] In addition, at intracellular level, pH difference between the extracellular environment (pH 7) and endosomes and lisosomes (pH 5) is a useful tool to selectively release therapeutic agents directly in cells.

One example of pH-senstive gated MSN is the reported by Qu and co-workers.[76] These authors described a pH-responsive gated nanodevice using AuNPs, grafted onto mesoporous silica through acid-labile hydrazone bond, as caps. The hydrazone moiety, a typical acid-sensitive bond, undergoes hydrolysis when it is exposed to acidic conditions (such as those found in some inflammation and tumor tissues). For the synthesis of hybrid material, Fe_3O_4 nanoparticles were coated with a silica mesoporous layer and functionalized with aminopropyl moieties. The amino groups were reacted with mono methyl glutarate to obtain methyl ester groups. These were reacted with hydrazine and then with 4-mercapto-4-methyl-2-pentanone to obtain a stalk that contained the acid-labile hydrazone linkage and ended in thiol moieties. In the final step, the pores of nanoparticles were loaded with DOX and capped upon the addition of AuNPs (Figure 22). At neutral pH (7.4), the linker remains intact and the material showed very weak DOX release. However, at acidic pH (5.0), the hydrolysis of the hydrazone bond removed the caps allowing drug release. Studies with HeLa cells showed the endocytosis of the nanovehicle and the release of the entrapped DOX

[75] a)R. van Sluis, Z.M. Bhujwalla, N. Raghunand, P. Ballesteros, J. Alvarez, S. Cerdan, J.P. Galons, R.J. Gillies, *Magn. Reson. Med.,* **1999**, *41*, 743. b) R. A. Cardone, V. Casavola, S. J. Reshkin, *Nat. Rev. Cancer*, **2005***, 5*, 786.

[76] L. Cui, H. M. Lin, C. Y. Yang, X. Han, T. Zhang, F. Y. Qu, *Eur. J. Inorg. Chem.*, **2014**, 6156.

in the acidic environment of the endosomes, with a subsequent reduction in cell viability.

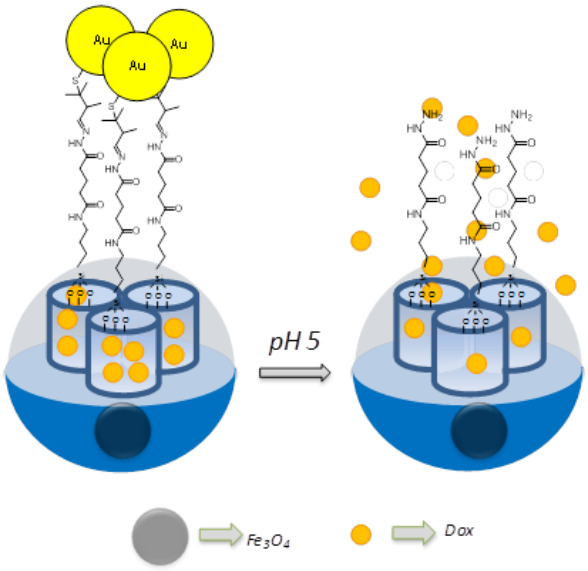

Figure 22. Schematic illustration of pH-responsive nanogated ensemble based on gold-capped mesoporous silica through a hydrazone linker.

Due to the broad range of pH found throughout the gastrointestinal tract, pH-responsive systems have also been used for the oral delivery of target molecules. In this case, designed nanodevices may protect drugs from the harsh conditions found in the gastric cavity avoiding their premature release and improving their absorption in the intestine.

One example is the use of gated nanodevices as a folic acid (FA) delivery system. Pérez-Esteve e*t al.*[77] compared the suitability of different silica supports (MCM-41, SBA-15, UVM-7 and hollow silica microspheres) caped with pH-responsive molecular gates (polyamines) to encapsulate FA and to achieve a controlled and sustained release of the vitamin under digestive conditions. In this work, the silica

[77] É. Pérez-Esteve, M. Ruiz-Rico, C. de la Torre, L. A. Villaescusa, F. Sancenón, M. D. Marcos, P. Amorós, R. Martínez-Máñez, J. M. Barat, *Food Chemistry,* **2016**, *196,* 66.

supports were loaded with FA and functionalized on the surface with 3-[2-(2-aminoethylamino) ethylamino]propyltrimethoxysilane. At low pH values (pH 2) polyamines were transformed to polyammonium groups. Due to the coulombic repulsions produced between closely located chains, the anchored moieties adopted a rigid-like conformation that blocked the pores and inhibited the release of the vitamin (see Figure 23). In contrast, at pH 7.5 (pH of the intestine), the conformation of the gate changed with the subsequent uncapping of the pores and FA delivery.

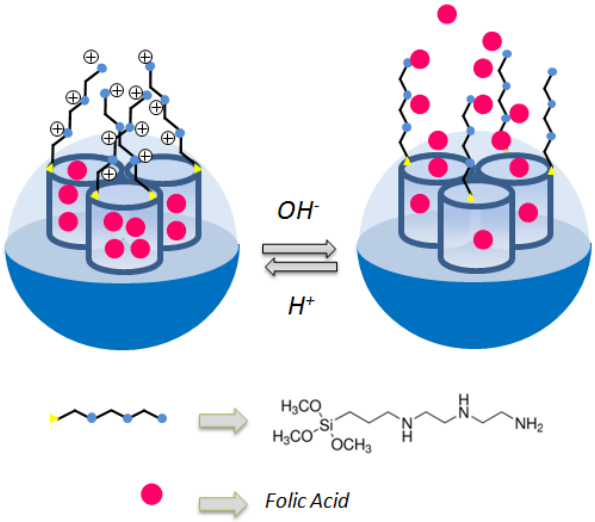

Figure 23. pH-responsive nanogated material for the delivery of folic acid.

Gated nanodevices activated under the ***presence of certain molecules and biomolecules*** have also been broadly described. Among different possibilities, some of the most commonly used molecules for the development of bio-gated hybrid materials are enzymes. The possibility of designing advanced gated systems capped with tailor-made molecular sequences that would be degraded by specific enzymes has a large potential. As an example, an altered expression profile of specific enzymes (such as proteases, phospholipases or glycosidases) is observed in some pathological conditions, such as cancer or inflammation. The altered level of these biomolecules can be exploited to achieve enzyme-mediated drug release with accumulation of drugs at the desired biological target. Most of

the systems devoted to enzyme-mediated drug delivery exploited the presence of enzymes in the cellular environment.

The first example of gated mesoporous system that responds to an enzyme was described by Stoddart *et al.* and was based on mesoporous support with a [2]rotaxane capped with an ester-linked adamantyl stopper.[48a] The addition of porcine liver esterase, which was able to hydrolyze the ester group, resulted in the removal of the adamantly moiety and the subsequent cargo delivery.

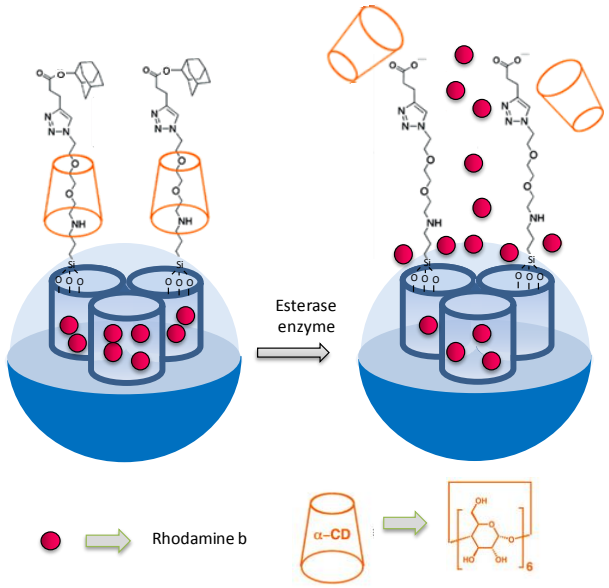

Figure 24. Controlled cargo release from an enzyme-responsive snap-top system. Adapted from J. Am. Chem. Soc., 2008, 130, 2382, Copyright © 2008 American Chemical Society

Martínez-Máñez and coworkers demonstrated that the attachment of a lactose derivative as gatekeeper on the surface of silica mesoporous supports provided a suitable method for the design of mesoporous systems that were able to deliver entrapped guests by a bio-controlled uncapping using β-D-galactosidase, due to the enzymatic hydrolysis of the glycosidic bond in the anchored lactose (see Figure 25).[78] Some years later, the same authors developed nanoscopic MCM-41

[78] A. Bernardos, E. Aznar, M. D. Marcos, R. Martínez-Máñez, F. Sancenón, J. Soto, J. M. Barat, P. Amorós, *Angew. Chem. Int. Ed.,* **2009**, *48*, 5884.

silica supports loaded with a dye and functionalized, on the pore outlets, with different commercially available hydrolyzed starch derivatives.[49] These materials were tested for the controlled cargo release in intracellular media in HeLa and LLC-PK1 cells.

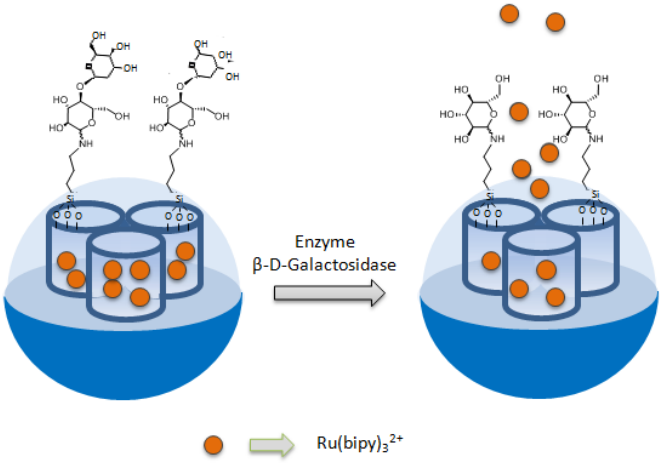

Figure 25. Controlled cargo release from lactose-capped MSN triggered by the hydrolysis of glycosidic bonds.

The same authors reported the preparation of a new biomaterial based on the combination of suitable 3D supports and gated MSN with potential applications in bone tissue engineering.[79] The biomaterial was composed by a macroporous scaffold and capped MSN designed to deliver the cargo in the presence of acid phosphatase (APase) enzyme. This enzyme is used to assess osteoclast activity in bone remodeling processes and as a biochemical marker for the presence of bone metastases. MSN were loaded with tris(2,2′-bipyridyl)ruthenium(II) chloride dye and the external surface of the silica mesoporous nanospheres was functionalized with 3-[2-(2-aminoethylamino)ethylamino] propyl-trimethoxy silane. Then, the material was treated with ATP. Coordination of ATP with the grafted polyamines (through electrostatic interactions and hydrogen bonds) induced pore closure and inhibited dye release. However, in the presence of APase enzyme dye release was observed due to ATP hydrolysis and subsequent decoordination from the grafted

[79] N. Mas , D. Arcos , L. Polo , E. Aznar , S. Sánchez-Salcedo , F. Sancenón , A. García , M. D. Marcos , A. Baeza , M. Vallet-Regí , R. Martínez-Máñez, *Small*, **2014**, *10*, 4859.

polyamines. Dye delivery of the final 3D material was also studied *in vitro* in the absence or the presence of APase (Figure 26). Finally, the biocompatibility of the scaffold was assessed in human osteoblast-like cell line (HOS) concluding that the macroporous architecture and the structure thickness was appropriate for the scaffold colonization by HOS cells.

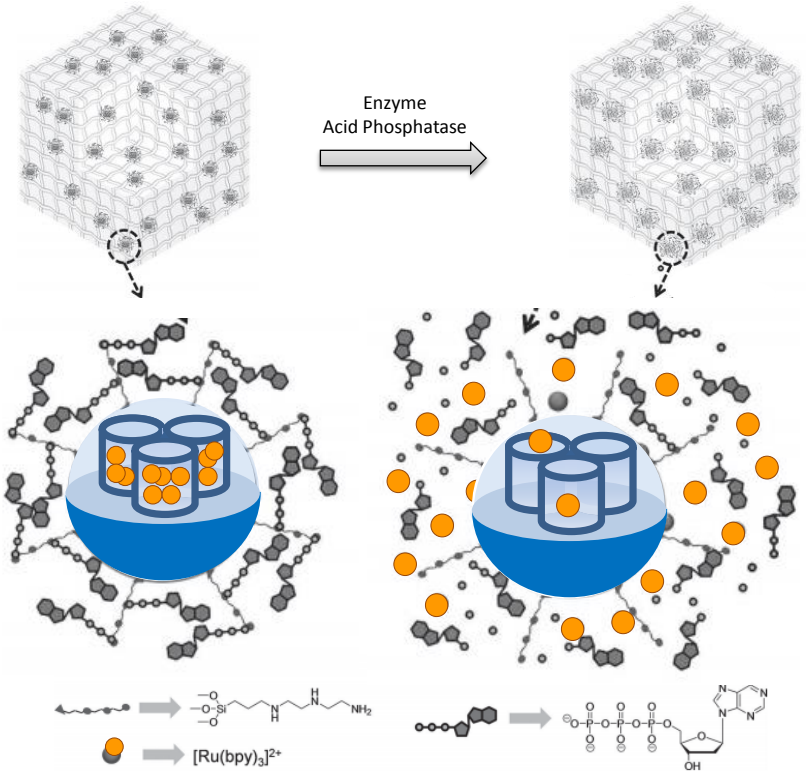

Figure 26. Schematic representation of an APase-driven MSN system. *Adapted from Small,* **2014**, *10*, 4859.

With the objective to achieve a high grade of selectivity toward particular cellular lines, polypeptide sequences were introduced as molecular gates, and specific peptidases used as triggers. Peptidases are enzymes capable of inducing the hydrolysis of peptide bonds that link amino acids in a polypeptide chain. As an example, Martínez-Máñez and coworkers[80] prepared a gated material based on

[80] C. de la Torre, L. Mondragón, C. Coll, F. Sancenón, M. D. Marcos, R. Martínez-Máñez, P. Amorós, E. Pérez-Payá, M. Orzaez, *Chem. Eur. J.,* **2014**, *20*, 15309.

MCM-41 loaded with safranine O dye or DOX and functionalized with peptide sequences designed for cathepsin B hydrolysis. Cathepsin B is a lysosomal enzyme that is highly associated with cancer development and metastasis. After loading, MSN were functionalized with 3-(azidopropyl)triethoxysilane. The final gated material was obtained through the reaction of azidopropyl groups on the surface with an alkynyl-derivatized peptide (alkynyl-GIVRAKEAEGIVRAK-OH) via a click chemistry reaction. Aqueous solutions of this material were unable to release the entrapped dye, whereas addition of lysosomal extracts that contained cathepsin B induced the enzymatic hydrolysis of the peptide sequences with the subsequent diffusion of the entrapped guest (Figure 27). In addition, cell internalization and delivery studies in HeLa cells and primary culture cells of mouse embryonic fibroblasts were performed with the safranin-loaded peptide-capped nanomaterial. A proper internalization of nanoparticles and a dye release associated with cathepsin B presence was demonstrated. Interestingly cell treatment with the capped nanoparticles loaded with cytotoxic drug DOX efficiently triggered cell death in both HeLa and MEF cells.

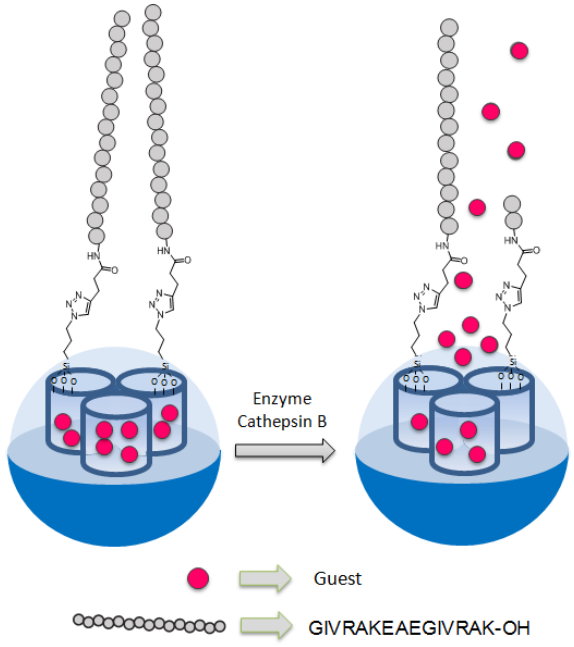

Figure 27. Controlled cargo release induced by cathepsin B from MSN capped with a peptide sequence.

1.3.2 Targeting and cellular uptake

Many research groups have reported that MSN can be internalized by a variety of mammalian cells, including cancer cells (HeLa, CHO, lung, PANC-1, MCF-7, RIN-5F) and non-cancerous cells (liver, endothelial, skin fibroblast).[40 b,d, 81] However, understanding of cellular internalization mechanisms has not yet been fully unveiled. MSN have been found to enter cells through endocytosis pathways in the majority of cases.[82] Endocytosis is a very complex process and several factors, such as the size and morphology of the silica nanoparticles[83] and the functional groups on the external particle surface[84] influence the intracellular endocytosis of MSN materials. Besides the delivery control provided by the molecular gates anchored on the material surface, other strategies are able to provide enhanced targeting to specific cells and tissues and to favor the nanocarrier accumulation in desired areas. The targeted drug delivery to damaged cells or specific tissues can be accomplished by using active or passive mechanisms.[85]

✓ *PASSIVE TARGETING*

Passive targeting is a result of enhanced permeability and retention effect (EPR) which is characteristic of leaky tissues of tumors. Tumor vasculature presents an increased permeability and is lacking of effective lymphatic drainage. These characteristics allow a preferential passive bioaccumulation of particles of certain sizes, such as liposomes, nanoparticles, and macromolecular drugs, in tumor tissues. Moreover, surface-functionalization methodologies can improve the stabilization of nanoparticles to remain in the bloodstream long enough to accumulate at the tumor site. As an example, the surface decoration with PEG

[81] a) D.R. Radu, C.-Y. Lai, K. Jeftinija, E.W. Rowe, S. Jeftinija, V.S.-Y. Lin. *J. Am. Chem. Soc.,* **2004,** *126*, 13216. b) I.I. Slowing, B.G. Trewyn, V.S.-Y. Lin. *J. Am. Chem. Soc.,* **2006**, *128*,14792. c) I.I. Slowing, B.G. Trewyn, V.S.-Y. Lin. *J. Am. Chem. Soc.,* **2007**, *129*, 8845.

[82] A. Prokop, J.M. Davidson. *J. Pharm. Sci.,* **2008,** *97,* 3518.

[83] a) B.G. Trewyn, J.A. Nieweg, Y. Zhao, V.S.-Y. Lin, *Chem. Eng. J.,* **2008**, *137*, 23. b) F. Lu, S.-H. Wu, Y. Hung, C.-Y. Mou, *Small*, **2009**, *5*, 1408.

[84] A. Verma, F. Stellacci, *Small,* **2010**, *6, 12.*

[85] F. Danhier, O. Feron, V. Préat, *J. Control. Release,* **2010**, *148*, 135.

chains induce the steric repulsion of blood circulating components (opsonins) that enhance phagocytosis, and endows the nanocarriers with *in vivo* longevity.[86]

✓ *ACTIVE TARGETING*

Active targeting can be achieved by covalent attachment of targeting molecules (ligands) to the particle surface. This strategy takes advantage of the overexpression of certain receptors on the surface of pathological cells (such tumor cells) and can promote specific and active nanocarrier binding and cellular uptake. As an example, FA has been widely used as targeting ligand, as folate receptors are known to be overexpressed in several types of human cancer, including ovarian, endometrial, colorectal, breast and lung.[87] In several works, the use of FA-conjugated MSN has shown a notable enhancement in uptake efficiency of the nanocarriers.[88] Besides FA, MSN have also been conjugated with other ligands such as sugar moieties,[89] the monoclonal antibody *anti*-HER2/neu[90] and DNA aptamers[91] for active targeting purposes.

Enhanced target selectivity of nanocarriers through passive or active mechanisms decreases unwanted side effects because of the avoiding of nonspecific toxicity to normal cells and thus, the therapeutic efficacy of drugs is expected to increase (Figure 28).

[86] S. Salmaso, P. Caliceti, *Journal of Drug Delivery*, **2013**, 19

[87] J. Sudimack, R. J. Lee. *Adv. Drug Deliv. Rev.,* **2000,** *41*, 147.

[88] Y. Matsumura, H. Maeda, *Cancer Res.*, **1986,** *46*, 6387

[89] a) I. Y. Park, I. Y. Kim, M. K. Yoo, Y. J. Choi, M.-H. Cho, C. S. Cho, *Int. J. Pharm.,* **2008**, *359*, 280, b) D. Brevet, M. Gary-Bobo, L. Raehm, S. Richeter, O. Hocine, K. Amro, B. Loock, P. Couleaud, C. Frochot, A. Morere, P. Maillard, M. Garcia, J. O. Durand*, Chem. Commun.,* **2009**, *12*, 1475

[90] C.-P. Tsai, C.-Y. Chen, Y. Hung, F.-H. Chang, C.-Y. Mou, *J. Mater. Chem.,* **2009**, *19*, 5737

[91] C.-L. Zhu, X.-Y. Song, W.-H. Zhou, H.-H. Yang, Y.-H. Wen, X.-R. Wang, *J. Mater. Chem.,* **2009**, 19, 7765.

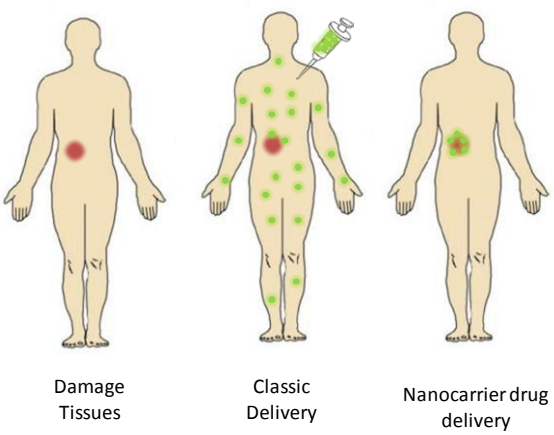

Figure 28. Scheme of ideal targeted drug delivery compared with classic delivery of drugs.

In some studies, such as that reported by Li and coworkers,[92] the advantages of nanoparticulate devices compared with marketed drugs have been demonstrated. In this work, PEGylated FITC-labeled docetaxel (Dtxl) loaded hollow MSN (SN-PEG-Dtxl), were tested for systemic toxicity and therapeutic efficacy along with Taxotere, the docetaxel-containing formulation, which has been on the market since 1996. Systematic toxicities of Taxotere and SN-PEG-Dtxl were evaluated in healthy female ICR mice by intravenous (i.v.) administrations (20 mg/kg Dtxl) in a span of 9 days. Special attention was drawn to circumvent hematological adverse effects and liver toxicity caused by Taxotere during the course of chemotherapy. The results indicated that SN-PEG-Dtxl showed lower toxicity than the Taxotere with equivalent Dtxl concentration. Additionally empty MSN and Dtxl loaded MSN did not cause any changes in organ morphology after a single dose of 40 mg/kg. Moreover, *in vivo* therapeutic efficacy for liver cancer was assessed using the marine hepatocarcinoma 22 (H22) subcutaneous model. In these experiments, both Taxotere and SN-PEG-Dtxl demonstrated a significant reduction of xenotransplanted hepatocarcinoma, but the tumors in the SN-PEG -Dtxl group were smaller than that in the Taxotere group. The average inhibition rate calculated from tumor weight by Taxotere was about 57%, while that of the SN-PEG-Dtxl group was as high as 72%.

[92] L. Li, F. Tang, H. Liu, T. Liu, N. Hao, D. Chen, X. Teng, J. He, *ACS Nano*, **2010**, *4*, 6874.

The above mentioned results reflect the possibilities of MSN-based nanodevices for *in vivo* enhancement of therapy efficacy and for reducing the systematic toxicity of antitumor drugs.

1.3.3 Biocompatibility

Silica is abundantly distributed in nature, has good compatibility, is accepted as "generally recognized as safe" (GRAS) by the U.S. Food and Drug Administration (FDA) and has been widely used in cosmetics and as FDA-approved food additives. Moreover, the physical and chemical properties of MSN and their design versatility makes this support an interesting drug delivery vehicle with clinical application prospects. The applicability and the biological performance of MSN drug delivery systems have been reported by numerous works. However, in order to bring this technology closer to the clinic, a comprehensive and extensive investigation of biodistribution safety and therapeutic efficacy of this drug delivery system is still needed.

Due to the huge possible variations of features in this class of materials, the study of how modulation of parameters influence in the compatibility and safety of nanodevices is very important for the design of efficient and safe drug delivery systems. Parameters such as particle structure, particle size, pore size and geometry, surface features, and particle shape have a complex influence on *in vitro* cellular uptake, intracellular translocation and cytotoxicity, and *in vivo* biodistribution, biodegradation, excretion, and toxicity (see Figure 29).[93] Research about the effects of certain parameters has been carried out, however, due to the complexity of nanotoxicity measurements, no definite conclusions can be made at this stage.

[93] F. Tang, L. Li, D. Chen, *Adv. Mater.,* **2012**, *24*, 1504.

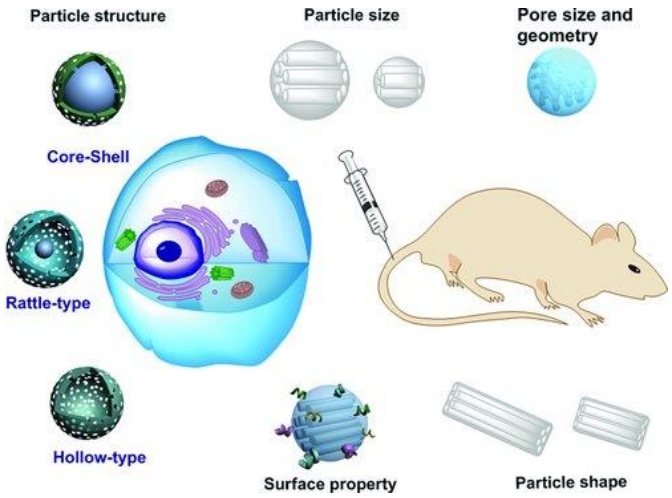

Figure 29. Schematic illustration of biocompatibility and biotranslocation of MSN. *Reprinted with permission from Adv. Mater.*, **2012**, *24*, 1504. *Copyright © 2012 WILEY-VCH Verlag GmbH & Co. KGaA, Weinheim.*

At this respect, Yu and coworkers[94] studied the single-dose, acute toxicity of engineered SiO_2 of various shapes, porosities, and surface features upon intravenous injection to immune-competent mice. The authors found out that *in vivo* toxicity was mainly influenced by MSN's porosity and surface characteristics. The maximum tolerated dose (MTD) increased in the following order: mesoporous silica particles at 30–65 mg/kg < amine-modified mesoporous particles at 100–150 mg/kg < unmodified or amine-modified non-porous particles at 450 mg/kg. The authors claimed that the adverse reactions were due to mechanical clogging of the vasculature followed by organ failure. They demonstrated that the hydrodynamic size of the particles could be linked to the impact on the vasculature and the tolerance threshold. The larger hydrodynamic size of the particles the lower the MTD.

In other work, reported by Liu and coworkers,[95] the systematic single and repeated dose toxicity, biodistribution and clearance of hollow MSN *in vivo* were demonstrated after intravenous injection in mice. The authors found that for

[94] T. Yu, K. Greish, L. D. McGill, A. Ray, H. Ghandehari, *ACS Nano,* **2012**, *6*, 2289.

[95] T. Liu, L. Li, X. Teng, X. Huang, H. Liu, D. Chen, J. Ren, J. He, F. Tang, *Biomaterials*, **2011**, *32*, 1657.

single dose toxicity, lethal dose 50 (LD50) of hollow MSN was higher than 1000 mg/kg. Further repeated dose toxicity studies indicated that no death was observed when mice were exposed to hollow MSN at 20, 40 and 80 mg/kg by continuous intravenous administration during 14 days. However liver injury caused by hollow MSN at high dose was observed (500 and 1280 mg/kg single administration). These results suggested low toxicity of hollow MSN when intravenous injection at single dose or repeated administrations. Furthermore, this study generated important data on MSN' biodistribution and compartmentalization in spleen and liver macrophages, and defined the 4 week period as sufficient for 50% nanoparticle clearance from the body, as determined by silica content reduction in different tissues.

Although wide knowledges of biodistribution safety and therapeutic efficacy of these nanodevices are still needed, these type of studies increases scientific reliability for the following research. Moreover, the first silica based diagnostic nanoparticles in the form of “C-dots” (Cornell dots) has been recently FDA approved for stage I human clinical trial. This represents an important step towards clinical acceptance of silica-based nanoparticles.[96]

[96] M. Benezra, O. Penate-Medina, P. B. Zanzonico, D. Schaer, H. Ow, A. Burns, E. DeStanchina, V. Longo, E. Herz, S. Iyer, J. Wolchok, S. M. Larson, U. Wiesner, M. S. Bradbury, *J. Clin. Invest.*, **2011**, *121*, 2768.

2. Glucose-Triggered Release Using Enzyme-Gated Mesoporous Silica Nanoparticles

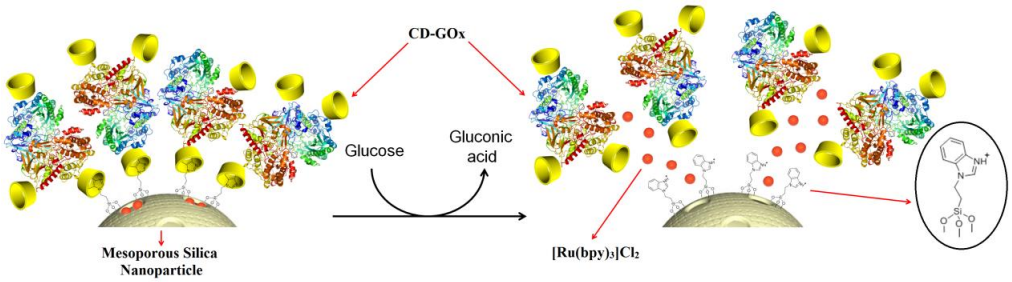

This chapter is derived from the adaptation of the following manuscript:

*Chem. Commun., **2013**, 49, 6391*

Reprinted with permission from Royal Society of Chemistry.

2.1 Introduction

As we have seen in Chapter 1, the potential use of nanostructured materials in nanomedicine as drug delivery systems has drawn considerable attention in the last years. Especially, the development of gated systems has demonstrated to be an excellent approach for the development of smart nanodevices for advanced delivery applications.[1] In this context, silica mesoporous supports are widely used as inorganic scaffolds thanks to their unique characteristics.[2] Moreover, via decoration of the mesoporous material with a wide collection of organic moieties, linkers and capping agents, researchers have prepared nanovalves that can inhibit the premature release of the entrapped drug but also allow its spatio-temporal release upon the application of a physical external stimulus or in response to changes in one or more chemical or biochemical features of the surrounding environment.

In this context, the design of systems capable of responding to changes in the concentration of specific analytes enables the development of drug delivery systems that mimic biological functions and are able to achieve self-regulated cargo release. This concept is particularly important in the non-invasive management of some disease such as diabetes, which requires a system that triggers the release of insulin according to blood-glucose levels.

One appealing approach in the realm of bioinspired stimuli-responsive materials is the development of enzyme-responsive bio-gated MSN. In most of the previously reported examples of enzyme responsive systems, tailor-made sequences anchored on the mesoporous support are hydrolized by target enzymes allowing

[1] a) C. Coll, A. Bernardos, Martínez-Máñez, F. Sancenón, *Acc. Chem. Res.,* **2013**, *46*, 339; b) E. Aznar, R. Martínez-Máñez, F. Sancenón, *Expert Opin. Drug Deliv.,* **2009**, *6,* 643; c) K. Cotí, M. E. Belowich, M. Liong, M. W. Ambrogio, Y. A. Lau, H. A. Khatib, J. I. Zink, N. M. Khashab, J. F. Stoddart, *Nanoscale*, **2009**, *1*, 16.

[2] C. T. Kresge, M. E. Leonowicz, W. J. Roth, J. C. Vartuli, J. S. Beck, *Nature,* **1992**, *359*, 710.

the selective release of the entrapped cargo.[3] However, and as a new approach, we envisioned the potential design of gated materials in which the enzymes could act as caps and the uncapping process would be triggered by the product obtained by the enzyme's activity on a target substrate. The combination of the promising features of silica mesoporous supports as containers, enzymes as caps and substrates as trigger would result in a sophisticated but simple way to prepare selective substrate-responsive gated mesoporous materials for different applications, such as the development of self-regulated drug delivery systems.

As a proof-of-concept, we have selected herein glucose oxidase (GOx) as capping enzyme and glucose as the substrate to trigger cargo release. We take advantage of the enzymatic reaction between glucose and glucose oxidase resulting in the production of gluconic acid, which can confer glucose responsiveness to a pH-sensitive system containing glucose oxidase.

2.2 **Objectives**

In this Chapter our aim was to design a new glucose-responsive gated material based on hybrid MSN loaded with a dye in which enzymes act as caps, as a proof of concept of self-regulated drug delivery system.
In particular, our objectives were:

- Design and preparation of MSN capped with glucose oxidase enzyme.
- Characterization of prepared materials and *in vitro* validation of the aperture protocol
- Study the dye released as a function of the glucose concentration level
- Study the selectivity of the material

[3] a)A. Agostini, L. Mondragón, L. Pascual, E. Aznar, C. Coll, R. Martínez-Máñez, F. Sancenón, J. Soto, M. D. Marcos, P. Amorós, et al. *Langmuir,* **2012**, *28*, 14766–14776. b) Z. W. Chen, Z. H. Li, Y. H. Lin, M. L. Yin, J. S. Ren, X. G. Qu, *Chem. Eur. J.,* **2013**, *19*, 1778–1783.c) A. Hakeem, R. Duan, F. Zahid, C. Dong, B. Wang, F. Hong, X. Ou, Y. Jia, X. Lou, F. Xia, *Chem. Commun.,* **2014**, *50*, 13268–13271.

2.3 **Synthesis and Characterization**

2.3.1 Design of the system

The designed capped support is depicted in Figure 1. It is based on the use of mesoporous silica nanoparticles loaded with a suitable reporter (i.e. ruthenium bipyridine complex) and containing anchored propylbenzymidazole moieties on the pore outlets. The mesopores are then capped with an active cyclodextrin modified glucose oxidase (CD-GOx) through the formation of an inclusion complex between the cyclodextrins and the propylbenzymidazole group anchored to the solid support. The presence of the substrate glucose combined with the catalytic action of CD-GOx to produce gluconic acid was expected to induce protonation of the benzymidazole group that might result in the inclusion complex dethreating and the subsequent cargo release. In this context, to the best of our knowledge, the use of glucose as trigger for a gated system has only been described by Lin et. al. In their work, they reported a saccharide-responsive controlled release of insulin and cAMP using phenylboronic acid-functionalized silica mesoporous nanoparticles.[4] However, this later system was based in a simple displacement reaction yet no enzymes were used in its design.

[4] Y.Zhao, B.G. Trewyn, I.I. Slowing, V.S.Y. Lin, *J. Am. Chem. Soc.,* **2009**, *131*, 8398.

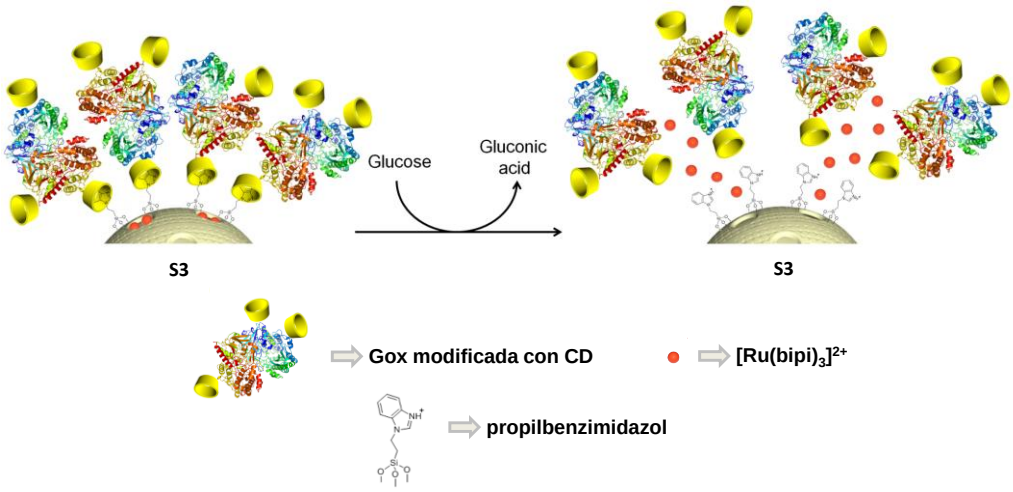

Figure 1. Solid **S3** expected performance.

2.3.2 Synthesis of the materials

In order to prepare the gated nanodevice, silica mesoporous (MCM-41-type) nanoparticles (ca. 100-150 nm) were selected as inorganic scaffold. The MCM-41 support was loaded with a suitable dye ($[Ru(bpy)_3]Cl_2$) and the external surface was functionalized with 3-iodopropyltrimethoxysilane (solid **S1**). Then, a nucleophilic substitution reaction of the anchored 3-iodopropyl moiety with benzimidazole resulted in a solid functionalised with 1-propyl-1-*H*-benzimidazole groups (solid **S2**).

For the preparation of the final gated material, CD-GOx was synthesized as previously reported[5] and a mixture of **S2** and CD-GOx in water at pH 7.5 was stirred for 24h. After that time, the capped solid was centrifuged and washed with water at pH 7.5 three times to obtain the orange final solid **S3**.

[5] M. Holzinger, L. Bouffier, R. Villalonga, S. Cosnier, *Biosens. Bioelectron.*, **2009**, *24*, 1128.

2.3.3 Characterization

Solids **S1** and **S2** were characterized using standard procedures. Figure 2 shows powder X-ray diffraction patterns of the as made nanoparticulated MCM-41 support, the template-free porous scaffolding and the **S1** and **S2** functionalized materials. Powder XRD of siliceous nanoparticulated MCM-41 as-synthesized (curve a) shows four low-angle reflections typical of a hexagonal array that can be indexed as (100), (110), (200) and (210) Bragg peaks. A significant displacement of the (100) peak in the powder XRD of the nanoparticulated MCM-41 calcined sample is clearly appreciated in curve b, corresponding to an approximate cell contraction of 6 Å. This displacement and the broadening of the (110) and (200) peaks are related to further condensation of silanol groups during the calcination step. Curve c corresponds to the **S1** powder XRD pattern. In this case, a slight intensity decrease and a broadening of the (110) and (200) reflections is observed, most likely related to a loss of contrast due to the filling of the pore voids with the dye. Nevertheless, the value and intensity of the (100) peak in this pattern strongly evidences that the loading process with the dye and the further functionalization with 3-iodopropyltrimethoxysilane have not damaged the mesoporous scaffolding. Finally, curve d corresponds to the **S2** powder XRD pattern in which the peak (100) is also observed confirming the preservation of the inorganic structure after the synthesis process.

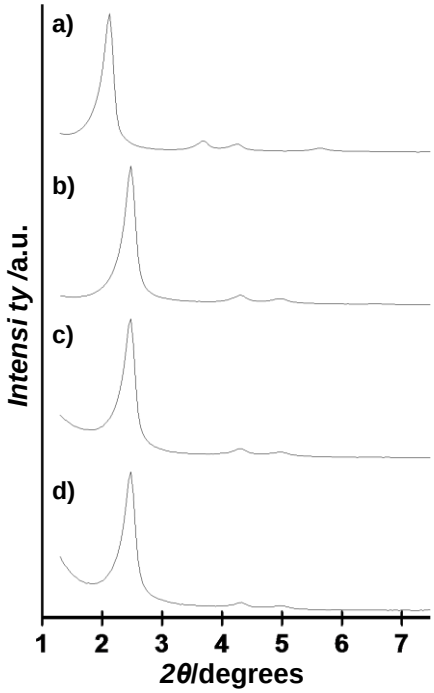

Figure 2. Powder X-ray diffraction patterns of the solids (a) MCM-41 as-synthesized (b) calcined MCM-41 (c) solid **S1** containing $[Ru(bpy)_3]Cl_2$ and 3-iodopropyltrimethoxysilane and (d) solid **S2** containing $[Ru(bpy)_3]Cl_2$ and 1-propyl-1-H-benzimidazole.

These results are consistent with TEM studies. Figures 3 (a) and (b) show a representative image of the calcined MCM-41 support and **S2** hybrid material, respectively. In these images, the typical hexagonal porosity of MCM-41 matrix can be observed. In addition, the images also evidence the spherical morphology of the particles and their diameter around 100 nm. Figure 3 (c) shows a representative image of solid **S3** where the enzyme coating that surrounds the mesoporous nanoparticle can be appreciated and the fact that inorganic structure has been maintained in the course of the materials synthesis is confirmed.

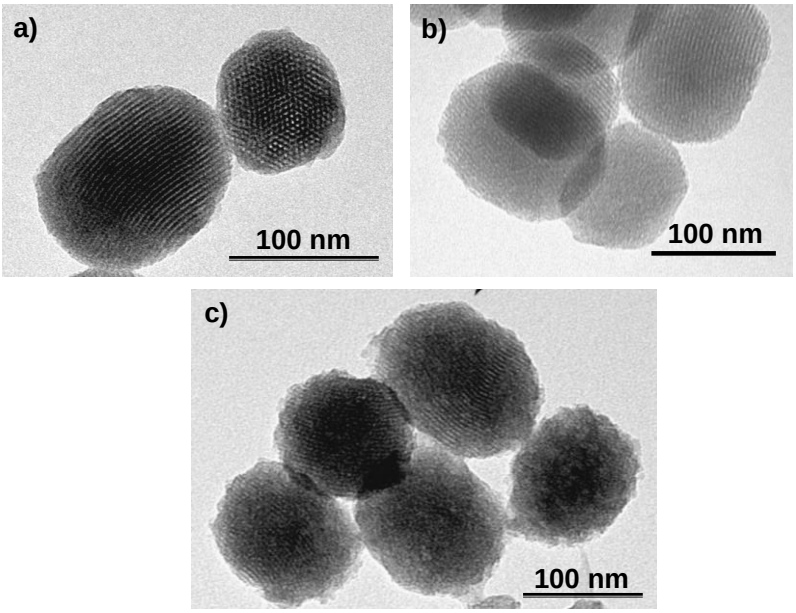

Figure 3.TEM images of (a) calcined MCM-41 sample (b) solid **S2** and (c) solid **S3** showing the typical hexagonal porosity of the MCM-41 mesoporous matrix.

The N_2 adsorption-desorption isotherms of the nanoparticulated MCM-41 calcined material shows two sharp adsorption steps. The isotherm shows a first step at intermediate P/P_0 value (0.1-0.4) typical of these solids (see Figure 4 curve a). This step can be related to the nitrogen condensation inside the mesopores by capillarity. The absence of a hysteresis loop in this interval and the narrow BJH pore distribution suggest the existence of uniform cylindrical mesopores with a pore volume of 0.76 $cm^3\ g^{-1}$ calculated by using the BJH model on the adsorption branch of the isotherm. The application of the BET model resulted in a value for the total specific surface of 1042 m^2/g. From the powder XRD, porosimetry and TEM studies, the a_0 cell parameter (3.56 nm), the pore diameter (2.38 nm) and a value for the wall thickness of 1.18 nm were calculated. In addition to this adsorption step associated to the micelle generated mesopores, a second feature appears in the isotherm at a high relative pressure ($P/P_0 > 0.75$). This second step corresponds to the filling of the large voids among the particles that must be considered as a textural-like porosity. In this case, curves show a characteristic H1 hysteresis loop and a wide pore size distribution.

The N_2 adsorption-desorption isotherm of **S2** is typical of mesoporous systems with filled mesopores (see Figure 4 curve b) and a significant decrease in the N_2 volume adsorbed and surface area (60.4 m^2/g) is observed. The most relevant feature is the absence of a sharp step at low-medium relative pressure ($0.1 < P/P_0 < 0.4$). In fact, this solid shows flat curves in that region when compared (at the same scale) to those of the MCM-41 parent material, which indicates a significant pore blocking and the subsequent absence of appreciable mesoporosity. Additionally, the curve shows a N_2 adsorption at high relative pressure similar to the calcined MCM-41, confirming that the textural porosity is preserved.

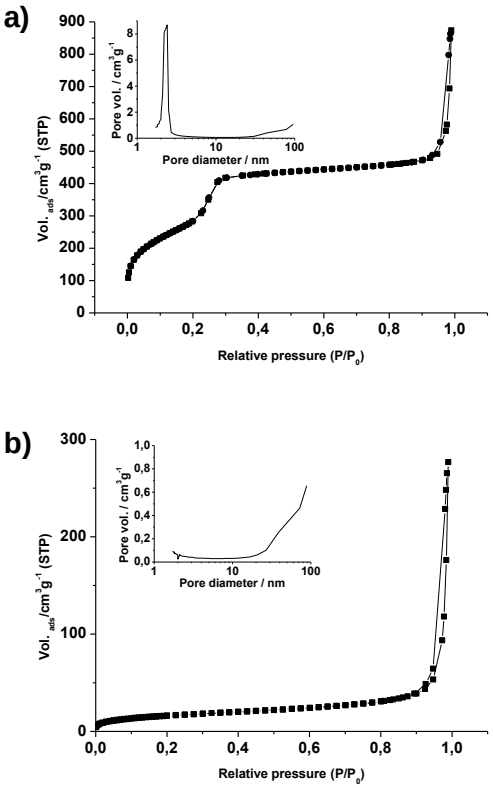

Figure 4. Nitrogen adsorption-desorption isotherms for (a) MCM-41 mesoporous material (b) **S2** material. Insets: Pore size distribution of the corresponding material.

BET specific surface values, pore volumes and pore sizes calculated from the N_2 adsorption-desorption isotherms for MCM-41 and **S2** are listed in Table 1.

Table 1. BET specific surface values, pore volumes and pore sizes calculated from the N_2 adsorption-desorption isotherms for selected materials.

	S_{BET} (m^2g^{-1})	BJH pore ($P/P_0 < 0.4$)[a] (nm)	BJH pore ($P/P_0 > 0.4$)[b] (nm)	Total pore volume[c] (cm^3g^{-1})	Pore volume ($P/P_0 < 0.4$)[d] ($cm^3\ g^{-1}$)	Pore volume ($P/P_0 > 0.4$)[e] ($cm^3\ g^{-1}$)
MCM-41	1042.1	2.38	50.78	1.16	0.76	0.40
S2	60.4	--	49.79	0.30	0.05	0.25

[a] Pore size estimated by using the BJH model applied on the adsorption branch of the isotherm, for $P/P_0 < 0.4$, which can be associated to the surfactant generated mesopores.

[b] Medium pore size estimated by using the BJH model applied on the adsorption branch of the isotherm, for $P/P_0 > 0.4$, which can be associated to the textural porosity.

[c] Total pore volume according to the BJH model.

[d] Pore volume for $P/P_0 < 0.4$, which can be associated to the surfactant generated mesopores.

[e] Pore volume for $P/P_0 > 0.4$, which can be associated to the textural porosity.

Ruthenium complex, 3-iodopropyl and 1-propyl-1-*H*-benzimidazole content in the prepared solids **S1,** and **S2** were determined by elemental analysis and thermogravimetric studies. Content values are detailed in Table 2.

Table 2. Ruthenium complex, 3-iodopropyl and 1-propyl-1-*H*-benzimidazole content in the prepared solids **S1** and **S2** in % wt.

Solid	**% [Ru(bpy)3]2+**	**% 3-iodopropyl**	**% 1-propyl-1-*H*-benzimidazole**
S1	19.7	2.2	-
S2	16.1	-	5.2

Taking into account that normal density of silanol groups in silica materials is 6 Si-OH nm^{-2} and that the reactive molecule had three reactive methoxy groups, the maximum density of 3-iodopropyl chains in the hybrid solids would be around 2 or

3 molecules per nm^2. From the content of 3-iodopropyl, it can be calculated that it is necessary around 104-156 nm^2 of surface to anchor all the 3-iodopropyl chains. As typical external surface for a nanoparticulated MCM-41 solid is ca.70 m^2g^{-1}, it is calculated that between 34-86 nm^2 of internal surface would additionally be modified with 3-iodopropyl chain. From TEM, we estimated that nanoparticles diameter was ca. 100 nm. Thus, the average mesopore length would also be 100 nm. Taking into account that each mesopores has two entrances, we can estimate that 3-iodoprpyl chain have penetrated and functionalized around 3.1 nm deep, allowing 93.8 nm without internal functionalization. From calculated data, it can be concluded that although 3-iodopropil chain could have slightly penetrated inside of the pores, its localization was reduced and limited by the presence of $[Ru(bpy)_3]Cl_2$ molecules in the pore voids.

2.4 **Results and discussion**

2.4.1 Delivery studies

In order to test the gating properties of the solid, portions of 150 µL of a suspension of **S3** (6.7 mg mL^{-1}) were diluted with 3 mL of water at pH 7.5 in the presence of glucose (0.1 mol L^{-1}) and stirred for a certain time. As a control experiment another portion of 150 µL of the suspension of **S3** was diluted in the same proportion and stirred. During the experiments, at a given time, 0.3 mL of each suspension was filtered, and the absorbance at 453 nm of the released $[Ru(bpy)_3]Cl_2$ was measured.

The delivery kinetics profile of the ruthenium dye in the presence and absence of glucose is shown in Figure 5. In absence of glucose (curve a) solid **S3** shows a very poor dye release, indicating tight pore closure. On the other hand, the delivery of the dye is induced when glucose is present in the solution (curve b) due to displacement of the CD-GOx as consequence of CD-GOx-induced oxidation of glucose to gluconic acid and protonation of the benzimidazole group. Additionally,

the figure also shows how release from the capped system can be triggered on command by adding glucose at a certain time (curve c).

The obtained results confirmed the triggering event hypothesis; i.e. whereas solid **S3** displayed no release, the presence of the substrate of the enzyme acting as cap induced the delivery of the entrapped cargo. Moreover, to confirm that the opening protocol was due to protonation of the benzimidazole, which induced the dethreating of the inclusion complex, pH changes in the final aliquots were measured. Thus, only in the experiments in which glucose was present a change from pH 7.5 to pH < 5.2 was observed confirming the enzyme-mediated conversion of glucose in gluconic acid. Additionally, generated gluconic acid was detected using a colorimetric assay, and release from solid **S3** at pH 5 was also tested. In that latter experiment, we found a massive release of the dye, confirming that the protonation of the benzimidazole moiety induces complex dethreating.

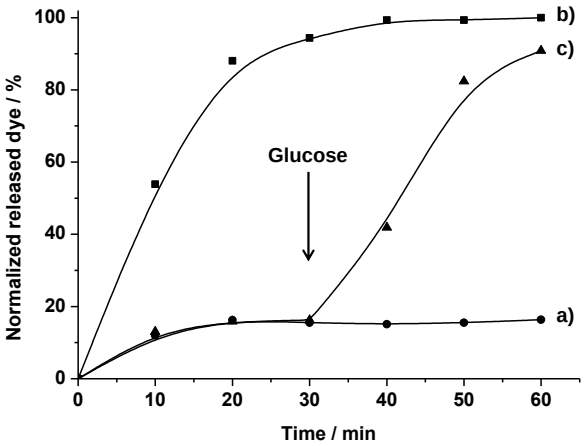

Figure 5. Release profile of $[Ru(bpy)_3]Cl_2$ from solid **S3** at pH 7.5 a) in the absence of glucose, b) in the presence of glucose c) with glucose addition at 30 min.

2.4.1 Delivery studies as a function of the glucose concentration

The capped nanoparticles **S3** or similar systems could be of application in the development of glucose-induced delivery systems or in the design of colorimetric probes for glucose determination. In this context, and as a further step in the characterization of the delivery system, the response of the hybrid material **S3** as a function of the glucose concentration was studied and the results are illustrated in Figure 6. From these data a linear release of the dye from **S3** in the $1x10^{-2}$ - $1x10^{-4}$ mol L^{-1} glucose concentration range was found. Moreover, a detection limit of glucose of $1.5x10^{-4}$ mol L^{-1} was calculated which was in the range of other glucose-responsive reported detection systems.[6] Taking into account that the general range of blood glucose concentration in healthy and diabetic humans is about 3–8 mol L^{-1} and 9–40 mol L^{-1}, respectively,[7] we can envision the potential of this enzyme-gated system for the design of chromo-fluorogenic probes for glucose detection.

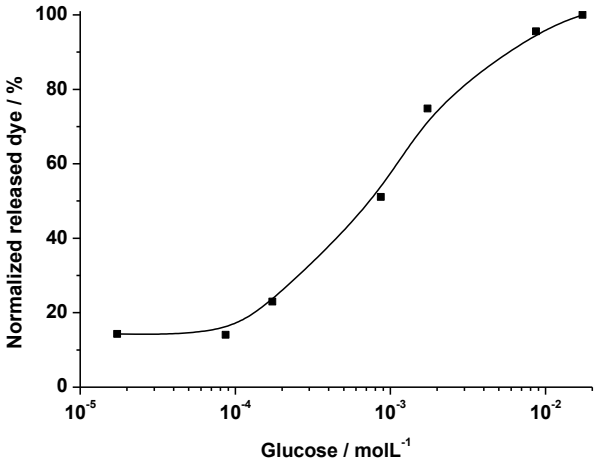

Figure 6. Released dye from solid **S3** in the presence of different glucose concentrations.

[6] a) N. S. Oliver, C. Toumazou, A. E. G. Cass and D. G. Johnston, *Diabetic Medicine*, **2009**, *26*, 197; b) Q. Wu, L. Wang, H. Yu, J. Wang, Z. Chen, *Chem. Rev.* **2011**, *111*, 7855.

[7] a) Y. Xu, P.E. Pehrsson, L. Chen, R. Zhang, W. Zhao, *J. Phys. Chem. C*, **2007**, *111*, 8638; b) C. Song, P.E. Pehrsson, W. Zhao, *J. Mater. Res.* **2006**, *21*, 2817; c) R. Badugu, J.R. Lakowicz, C.D. Geddes, *Anal. Chem.*, **2004**, *76*, 610.

2.4.1 Selectivity studies

Moreover, as it is well-known enzymes are selective catalytic centres. In our case, although numerous sugars and derivatives of glucose have been reported to be substrates of glucose oxidase, the enzyme shows far greater activity with glucose. In this scenario, the selectivity in the opening protocol in **S3** was tested in the presence of different saccharides such as mannose, fructose, galactose, maltose and saccharose at a concentration of $1x10^{-3}$ mol L^{-1} and following the same described procedure. As it can be seen in Figure 7 a selective uncapping was observed in the presence of glucose confirming the selective triggering.

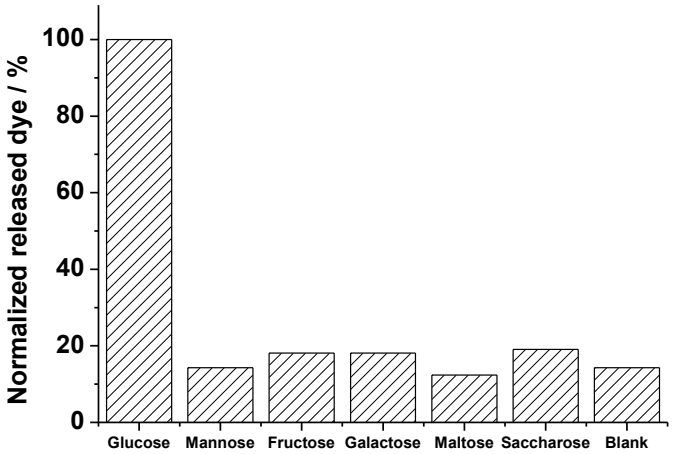

Figure 7. Released dye from 1 mg of solid **S3** in the presence of different analytes ($1x10^{-3}$ molL^{-1}).

2.5 **Conclusions**

In summary, we have reported a new approach for the development of gated materials using enzymes. In this proof-of-principle, the mesoporous material is capped with an active CD-modified-glucose oxidase (CD-GOx) through the formation of inclusion complexes between the cyclodextrins and the propylbenzymidazole group anchored to the solid support. In the presence of glucose as target substrate a cascade response results in a delivery of the

entrapped cargo. In particular, CD-GOx converts glucose to gluconic acid which induces the protonation of benzimidazole which results in a dethreating of the inclusion complex and delivery of the dye. The approach is simple and versatile and may allow to inspire the design of high selective on-command delivery systems based on enzyme's activity on target substrates for different applications

2.6 **Experimental Section**

2.6.1 Chemicals

The chemicals tetraethylorthosilicate (TEOS), *n*-cetyltrimethylammonium bromide (CTABr), sodium hydroxide (NaOH), tris(2,2'-bipyridyl)dichlororuthenium(II) hexahydrate, 3-iodopropyltrimethoxysilane, benzimidazole, triethylamine, glucose, mannose, fructose, galactose, maltose and saccharose were provided by Aldrich. Dry acetonitrile, toluene and ethyl acetate were provided by Scharlau. All reagents were used as received. β-cyclodextrin-modified glucose oxidase (CD-GOx) was synthesized as previously reported.5

2.6.2 General Characterization Techniques

Powder XRD, TG analysis, elemental analysis, transmission electron microscopy, N_2 adsorption-desorption and UV-visible spectroscopy techniques were used to characterize the prepared materials. X-ray measurements were performed on a Bruker AXS D8 Advance diffractometer using Cu-Kα radiation. Thermo-gravimetric analyses were carried out on a TGA/SDTA 851e Mettler Toledo equipment, using an oxidant atmosphere (Air, 80 mL/min) with a heating program consisting on a heating rate of 10 °C per minute from 393 K to 1273 K and an isothermal heating step at this temperature during 30 minutes. TEM images were taken with a Philips CM10 microscope working at 100 kV. N_2 adsorption-desorption isotherms were recorded on a Micromeritics ASAP2010 automated sorption analyser. The samples were degassed at 120 °C under vacuum overnight. The specific surface areas were calculated from the adsorption data in the low pressures range using the BET

model. Pore size was determined by following the BJH method. UV-visible spectroscopy was carried out with a Lambda 35 UV/vis spectrometer (Perkin-Elmer Instruments).

2.6.3 Synthesis of the materials

2.6.3.1 *Synthesis of the silica mesoporous nanoparticles support*

The MCM-41 mesoporous nanoparticles were synthesized by the following procedure: *n*-cetyltrimethylammoniumbromide (CTABr, 1.00 g, 2.74 mmol) was first dissolved in 480 mL of deionized water. Then, 3.5 mL of a NaOH 2.00 mol L^{-1} solution was added followed by an adjustment of the temperature to 80 °C. TEOS (5.00 mL, 22.4 mmol) was then added dropwise to the surfactant solution. The mixture was stirred for 2 hours to give a white precipitate. Finally the solid was collected by centrifugation, washed with deionized water and dried at 70 °C overnight (MCM-41 as-synthesized). To prepare the final porous material (MCM-41), the as-synthesized solid was calcined at 550 °C using an oxidant atmosphere for 5 hours in order to remove the template phase.

2.6.3.2 *Synthesis of **S1***

To synthesize the hybrid solid **S1**, 500 mg of the calcined MCM-41 support and 0.30 g (0.04 mmol) of tris(2,2'-bipyridyl)dichlororuthenium(II) hexahydrate were suspended in 25 mL of anhydrous acetonitrile and heated at 120 °C in a Dean–Stark apparatus to remove the adsorbed water under an inert atmosphere (Ar gas). The suspension was stirred for 24 hours at room temperature with the aim of loading the pores of the MCM-41 scaffolding. After this, an excess of 3-iodopropyltrimethoxysilane (196 µL, 1 mmol) was added and the suspension was stirred for 5.5 hours. The final orange solid (**S1**) was filtered off, washed with 5 mL of acetonitrile and dried at 70 °C overnight.

2.6.3.3 *Synthesis of **S2***

To prepare solid **S2**, 500 mg of **S1** were suspended in a 40 mL of a saturated solution of benzimidazole in toluene at 80 °C and containing triethylamine (benzimidazol and triethylamine in a 1:3 proportion). The suspension was refluxed and stirred during 72 hours. The final orange solid (**S2**) was filtered off, washed with 40 mL of acetonitrile and dried at 70 °C overnight.

2.6.3.4 *Synthesis of **S3***

To prepare solid **S3**, 10 mg of **S2** were suspended in 1mL of CD-GOx solution (1.56 mg/mL). The suspension was stirred during 24 hours at room temperature. The final capped orange solid (**S3**) was centrifuged (7500 rpm, 3 min) and washed with deionized water at pH 7.5 five times.

2.6.4 Release experiments

To perform the release studies, the freshly prepared **S3** solid (10 mg) was suspended in 1.5 mL of deionized water at pH 7.5. Then, each batch was prepared taking 150 µL of the suspension and diluting it to 3 mL with deionized water or the corresponding solution at pH 7.5. To monitor the ruthenium complex release, after a fixed time, 0.3 mL of the suspension were filtered off using 0.45 µm PTFE filters and the delivered cargo was registered via the $[Ru(bpy)_3]Cl_2$ absorbance at 453 nm.

2.6.5 Gluconic acid detection

Generated gluconic acid in the filtered aliquots after the triggering event was detected using the colorimetric assay described by Papandreou[8] and used by Ren and Qu.[9] In this experiment, 125 µL of solution 1 (5 mmol L^{-1} EDTA and 0.15 mmol

[8] E.T. Rakitzis, P. Papandreou, *Chem-Biol. Interact.,* **1998**, *113*, 205.

[9] Y. Lin, Z. Li, Z. Chen, J. Ren, X. Qu, *Biomaterials*, **2013**, *34*, 2600.

L^{-1} triethylamine in water) and 12.5 µL of solution 2 (3 mmol L^{-1} NH_2OH in water) were added to 200 µL of the filtered solution. After 25 min of incubation, 62.5 µL of solution 3 (1 mmol L^{-1} HCl, 0.1 mmol L^{-1} $FeCl_3$, and 0.25 mmol L^{-1} CCl_3COOH in water) was added to the above aqueous solution, and the reaction was allowed to proceed for 5 min before spectral measurements. Thus, an increment in the absorption band at 505 nm was observed confirming the gluconic acid presence and the enzyme-mediated conversion of glucose in gluconic acid.

3. Gated mesoporous silica nanoparticles for the controlled delivery of drugs in cancer cells

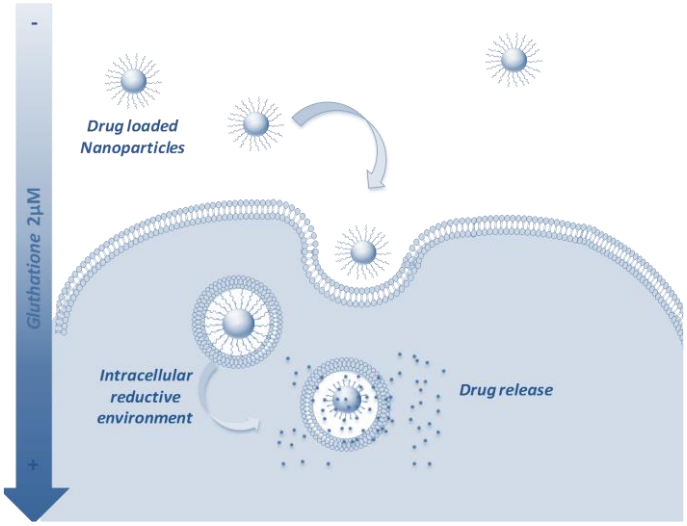

This chapter is derived from the adaptation of the following manuscript:

*Langmuir, **2015,** 31, 3753*

Reprinted with permission from American Chemical Society.

3.1 **Introduction**

The development of controlled release nanodevices for the encapsulation of therapeutic agents is especially appealing in the delivery of cytotoxic drugs for cancer treatment. Conventional chemotherapy is used to treat cancer using systemic application of free toxic compounds at their maximum tolerated dose. Chemotherapeutic drugs commonly exploit rapid cell division or other poorly selective criteria to obtain selectivity for cancer cells. Their broad distribution in the body and their non-specific activity, that kills many other healthy cell types, results in unacceptable side effects[1] and limits the drug doses tolerated and the treatment efficacy. Hereby, the possibility to deliver more of the drug dose towards tumor sites can dramatically improve the efficacy of the treatments and make anti-cancer therapies safer than conventional approaches.

Recently, the design of drug delivery systems for cancer therapy takes advantage of several characteristics that distinguish the microenvironment of a solid tumor from normal tissues.[2] As we mentioned in Chapter I, one characteristic is the abnormal vascular structure that tumors shown.[3] In normal tissues, pro-angiogenic and anti-angiogenic factors balance regulate and maintain an organized vascular system. To grow and surpass a critical size, tumors induce an imbalance in vascular regulation and develop new blood vessels to provide nutrients to rapidly dividing cancer cells.[4] But nevertheless, the resulting vasculature is disorganized, structurally flawed and presents leaky walls and a complete lack of lymphatics. [5]

[1] a) Marshfield Clinic. Retrieved January 2, **2014**

[2] Vaupel P. *Semin. Radiat. Oncol*. **2004**, *14*, 198.

[3] R. Cairns, I. Papandreou, N. Denko, *Mol. Cancer Res.*, **2006**, *4*, 61.

[4] J.H.E. Baker, K.E. Lindquist, L. Huxham, A.H. Kyle, J.T. Sy, A.I. Minchinton. *Clin. Cancer. Res.,* **2008**, *14*, 2171. b) M.R. Dreher, W.G. Liu, C.R. Michelich, M.W. Dewhirst, F. Yuan, A. Chilkoti, *J. Natl. Cancer Ins.*, **2006**, *98*, 335.

[5] R.K. Jain, T. Stylianopoulos, *Nat. Rev.,* **2010**, *7*, 653.

These characteristics result in large pores in the tumor architecture vasculature, ranging from 100 nm to several hundred nanometers in diameter, as compared to normal vessel junctions of 5-10 nm.[6] Consequently, the higher vascular permeability enables macromolecules such as nanoparticles to reach tumor cells. The impaired lymphatic system coupled with increased permeability of tumor vasculature (EPR effect) results in the accumulation of high molecular weight (≤ 40 kDa) long-circulating macromolecules and nanoparticles. This effect leads a passive targeting of drug nanocarriers and allows achieving higher intratumoral drug concentration and decreasing the toxicity in normal tissues.[7]

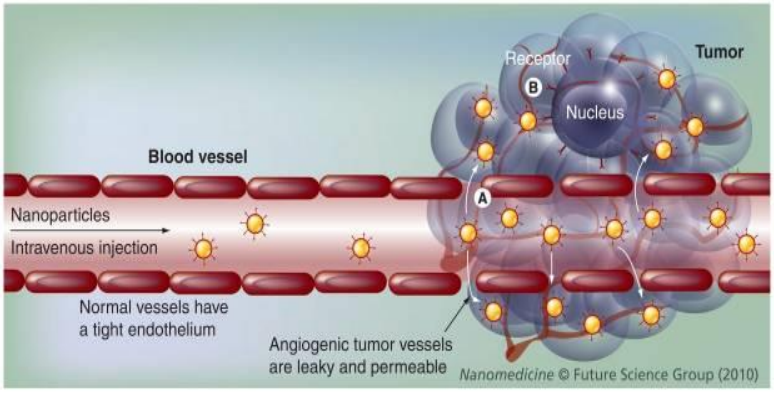

Figure 1: Enhanced drug delivery to solid tumors using nanoparticles. Reprinted with the permission of *Nanomedicine,* **2010**, *5,* 597. *Copyright ©2010 Future Science Group*

Based in these concepts, a number of nanodevices for encapsulation, transport and intracellular release of antineoplasic agents have been described based on different platforms such as liposomes, polymeric nanoparticles, lipid–polymer hybrid nanoparticles, dendrimers and inorganic nanoparticles.[8]

[6] S.K. Hobbs, W.L. Monsky, F. Yuan, *Proc. Natl. Acad. Sci. USA*, **1998**, *95*, 4607.

[7] a) K. Greish, *Methods Mol. Biol.* **2010**, *624*, 25. b) A. K. Iyer, G. Khaled, J. Fang, H. Maeda, *Drug Discov. Today,* **2006**, *11*, 812. c) R. K. Jain, T. Stylianopoulos, *Nat. Rev. Clin. Oncol.* **2010**, *7*, 653. d) H. Maeda, *Adv. Enzyme Reg.,* **2001**, *41*, 189.

[8] a) T. M. Allen, P. R. Cullis, *Adv. Drug Deliv. Rev.*, **2013**, *65*, 36. b) F. Gu, L. Zhang, B. A. Teply, N. Mann, A. Wang, A. F. Radovic-Moreno, R. Langer, O. C. Farokhzad, *Proc. Natl. Acad. Sci. USA,* **2008**,

In this context redox-responsive delivery systems are particularly appealing because intracellular delivery of therapeutic agents can be achieved by the reductive environment of the cytosol tied with a high concentration of glutathione (GSH). In fact, since Lin and coworkers reported the first redox-responsive gated material in which cadmium nanoparticles blocked the pore entrances of a silica mesoporous support and the release of the entrapped fluorescein was triggered by the rupture of a disulphide bond,[9] several capped systems driven by GSH and other reducing agents have been described.[10] GSH is a thiol-containing tripeptide capable of reducing disulfide bonds, and its intracellular concentration (10 mM) is significantly higher than its concentration in blood plasma (2 μM).[11] These differences in GSH concentration inside and outside the cell allows the design of GSH-driven nanovalves for drug transport that remain closed in extracellular environments whereas they open and deliver their cargo in intracellular medium.

105, 2586. c) K. Hadinoto, A. Sundaresan, W. S. Cheow, *Eur. J. Pharm. Biopharm*. **2013**, *85*, 427. d) H. Mattoussi, V. M. Rotello, *Adv. Drug Deliv. Rev.,* **2013**, *65*, 605. e) J. M. Montenegro, V. Grazu, A. Sukhanova, S. Agarwal, J. M. de la Fuente, I. Nabiev, A. Greiner, W. J. Parak, *Adv. Drug. Deliv. Rev*., **2013**, *65*, 677. f) O. L. Padilla De Jesús, H. R. Ihre, L. Gagne, J. M. Frechet, F. C. Jr. Szoka, *Bioconjug. Chem.,* **2002**, *13*, 453. g) C. E. Probst, P. Zrazhevskiy, V. Bagalkot, X. Gao, *Adv. Drug Deliv. Rev.,* **2013**, *65*, 703. h) V. P. Torchilin, *Nat. Rev. Drug Discov.,* **2005**, *4*, 145. i) L. Zhang, J. M. Chan, F. X. Gu, J. W. Rhee, A. Z. Wang, A. F. Radovic-Moreno, F. Alexis, R. Langer, O. C. Farokhzad, *ACS Nano,* **2008**, *2*, 1696. j) B. Mandal, H. Bhattacharjee, N. Mittal, H. Sah, P. Balabathula, L. A. Thoma, G. C. Wood, *Nanomedicine,* **2013**, *9*, 474.

[9] S. Giri, B.G. Trewyn, M.P. Stellmaker, V.S.Y. Lin, *Angew. Chem. Int. Ed.,* **2005**, *44*, 5038.

[10] a) A. N. Koo, H. J. Lee, S. E. Kim, J. H. Chang, C. Park, C. Kim, J. H. Park, S. C. Lee, *Chem. Commun.,* **2008**, *48*, 6570. b) R. Mortera, J. Vivero-Escoto, I. Slowing, E. Garrone, B. Onida, V. S. Lin, *Chem. Commun.,* **2009**, *22*, 3219. c) F. Porta, G. E. M. Lamers, J. I. Zink, A. Kros, *Phys. Chem. Chem. Phys.,* **2011**, *13*, 9982. d) T. Thambi, V. G. Deepagan, H. Ko, D. S. Lee, J. H. Park, *J. Mater. Chem.,* **2012**, *22*, 22028. e) K. Wang, Y. Liu, W. J. Yi, C. Li, Y. Y. Li, R. X. Zhuo, X. Z. Zhang, *Soft Matter,* **2013**, *9*, 692. f) Y.C. Wang, F. Wang, T.M. Sun, J. Wang, *Bioconj. Chem.,* **2011**, *22*, 1939. g) R. Hong, G. Han, J. M. Fernández, B. J. Kim, N. S. Forbes, V. M. Rotello, *J. Am. Chem. Soc.,* **2006**, *128*, 1078.

[11] D. P. Jones, J. L. Carlson, P. S. Samiec, Jr. P. Sternberg, Jr. V. C. Mody, R. L. Reed, L. A. S. Brown, *Clin. Chim. Acta,* **1998,** *275*, 175.

Moreover, the GSH levels in some cancer tissues have been found many-fold higher than those in normal tissues.[12]

In the same context, the preparation of controlled release nanodevices able to remain stable and bioavailable for long time in the human body environment is a pursued goal. As was commented in Chapter I, in this field, polyethylene glycol (PEG) has been widely used. This molecule is a highly hydrophilic polymer currently and thoroughly used in drug delivery formulations. It has been demonstrated that *PEGylation* of nanoparticles increases its solubility in buffer and serum due to the hydrophilic ethylene glycol moieties. Moreover, the presence of PEG groups on the surface of nanoparticles reduces the nonspecific binding of nanoparticles to blood proteins and macrophages, resulting in the so-called "stealth" behaviour. As a result, it has been described that the blood circulation half-lives of PEG-containing nanocarriers are prolonged and the passive targeting to cancer cells tied with EPR effect could be enhanced.

3.2 Objectives

Based in these concepts, our aim was to design a GSH-responsive gated material, based on MSN, as a simple to prepare and stable delivery systems for cytotoxic agents. In particular our objectives were:

- Design and preparation of MSN loaded with a dye and with a drug, capped with PEG chains through disulphide linkage.
- Characterization of prepared materials and *in vitro* validation of the aperture protocol.
- Study the intracellular aperture and cargo release in HeLa cancer cells.

[12] a) J. M. Estrela, A. Ortega, E. Obrador, *Critical Rev. Clin. Lab. Sci.,* **2006**, *43*, 143. b) C. C. Yeh, M. F. Hou, S. H. Wu, S. M. Tsai, S. K. Lin, L. A, Hou, H. Ma, L.Y. Tsai, *Cell Biochem. Funct.,.* **2006**, *24*, 555.

3.3 Synthesis and Characterization

3.3.1 Design of the system

We report herein the preparation of a hybrid material consisting of MSN loaded with a cargo (a dye or drug) and functionalized with PEG chains in the pore outlets using a disulfide linkage. The proposed paradigm is depicted in Figure 2. It was expected that the size of PEG chains would be enough to block the pores and to inhibit cargo release. Moreover, as illustrated in Figure 2, the presence of the intracellular reducing agent GSH is expected induce the uncapping of the pores and the delivery of the entrapped guest.

In this study, we selected spherical nanometric MSN from the MCM-41 family as support. In relation to the capping ensemble, as stated above, we aimed to develop a gate-like platform that could be triggered by the GSH present in cells. As capping molecules we selected two different sized polyethylene glycol chains of number average molecular weights (Mn) of 350 and 800, containing a terminal thiol group. Moreover different solids loaded with safranin O (**S1** and **S2**) or with doxorubicin (**S3**) were prepared.

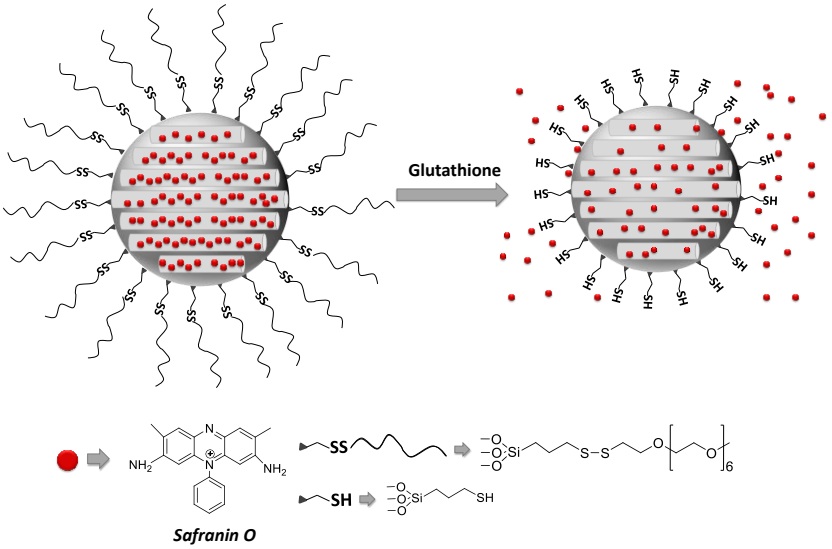

Figure 2. Schematic representation of the gated material **S1** capped with PEG chains via disulfide linkage.

3.3.2 Synthesis of the materials

MSN were synthesised by using tetraethyl orthosilicate (TEOS), which acts as an inorganic precursor, and hexadecyltrimethylammonium bromide (CTAB) as a structure-directing agent. The subsequent removal of the surfactant by calcination in air at high temperature resulted in the starting mesoporous inorganic nanoparticles. To prepare the capped material containing the dye Safranin O in the pore voids and the 350 Mn PEG in the pore outlets (**S1**), we followed a four-step synthetic procedure (see Figure 3). As a first step, calcined MSN were added to a water solution containing a high safranin O concentration and were stirred for 24 h to achieve an efficient loading of pores. The loaded solid was treated with 3-mercaptopropyltrimethoxysilane and then with 2,2'-dipyridyl disulfide to obtain 2-pyridinyldisulfanylpropyl-functionalized MSN. Finally, grafting of polyethylene glycol chains onto the external surface was achieved through the formation of a disulfide linkage by reaction with O-(2-mercaptoethyl)-O-methyl-hexa(ethyleneglycol). The nanoparticles were washed with abundant water and dried under vacuum to obtain the final solid **S1**. The hybrid material **S2** was synthesized following the same procedure as **S1**, but in this case, PEG of 800 Mn was used. Finally, PEG-capped doxorubicin-containing hybrid material **S3** was prepared following the same procedure as **S1**, but using the drug doxorubicin as cargo.

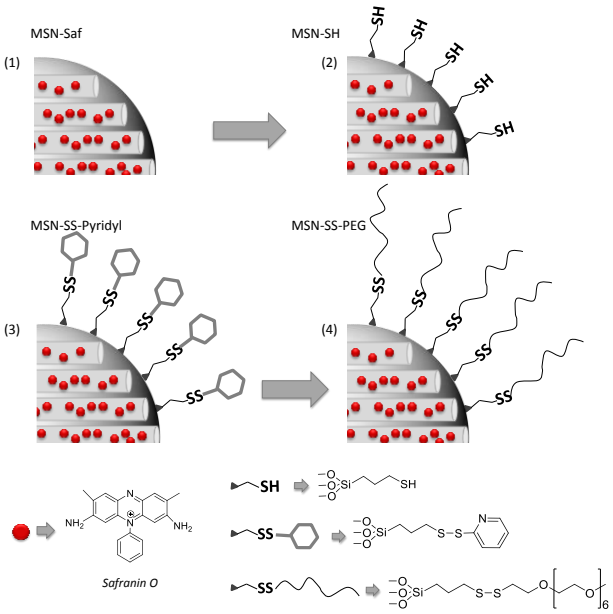

Figure 3. Synthetic route for preparing the final solid **S1**.

3.3.3 Characterization

The prepared solids were characterized using standard techniques. Powder X-ray diffraction (PXRD) patterns of the as-synthesized MSN, calcined MSN, and the final materials **S1**, **S2** and **S3** are shown in Figure 4. As it can be appreciated, the PXRD of synthesized MSN (Figure 4a) shows the four low-angle reflections attributed to the typical MCM-41 hexagonal array that can be indexed as (100), (110), (200), and (210) Bragg peaks. From these data, a d_{100} spacing of 42.25 Å can be calculated. In a further step, the PXRD of calcined MSN (Figure 1b) shows a significant displacement of the (100) peak, that can be attributed to an approximate cell contraction of 3.64 Å. This displacement and broadening of the (110) and (200) peaks found in calcined MSN is related to further condensation of silanol groups during the calcination step. Finally, Figures 1c to 1e show the PXRD patterns for solid **S1**, **S2** and **S3** respectively. In these curves, the reflections (110) and (200) are practically lost, most likely due to a reduction in contrast as a consequence of the pore loading with the Safranin O dye (for **S1** and **S2**) or

doxorubicin (for **S3**) and the functionalization with the corresponding polyethylene glycol chains. Nevertheless, the presence of the (100) peak in the PXRD pattern indicated that the process of pore loading and the additional functionalization with PEG did not modify the mesoporous structure of the MSN support in a large extent. The mesoporous structure of the prepared solids was also confirmed using transmission electron microscopy (TEM) analysis. As it can be observed in representative images of Figure 4, for solids **S1** and **S2**, MSN were obtained as spherical particles with a diameter of ca. 90 nm. Moreover, the typical MCM-41-like hexagonal arrangement of the mesopores can also be observed.

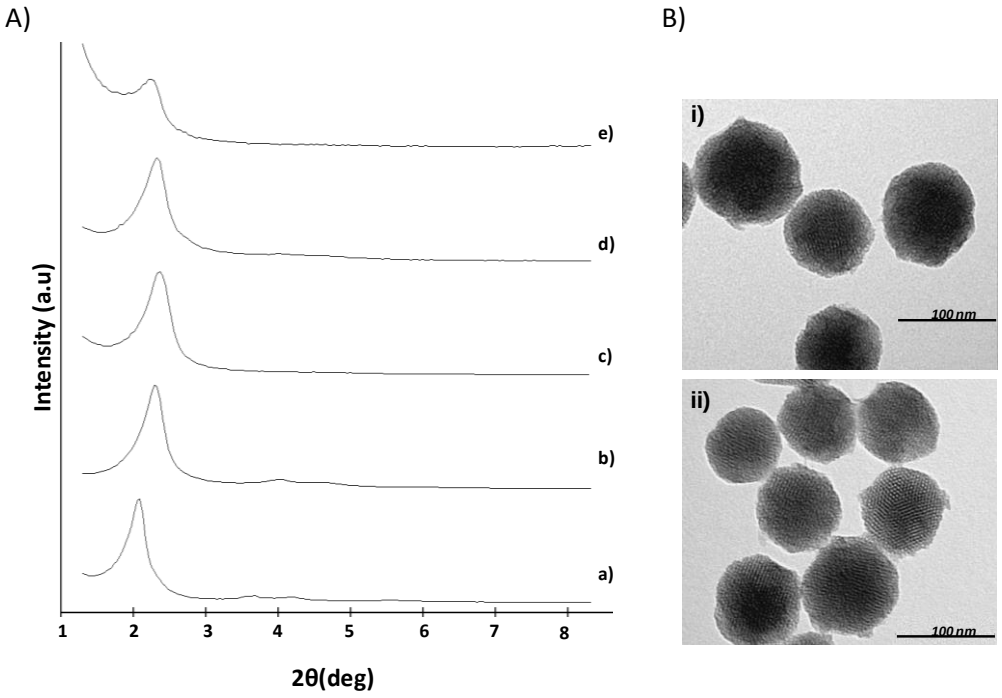

Figure 4. A) Powder X-ray pattern of a) MSN, b) calcined MSN, c) solid **S1** containing safranin O and functionalized with PEG (Mn 350), d) solid **S2** containing safranin O and functionalized with PEG (Mn 800) and e) solid **S3** containing doxorubicin and functionalized with PEG. B) Transmission electron microscopy (TEM) images of i) solid **S1**, and ii) solid **S2** showing the typical porosity of the MCM-41 matrix.

In addition, N_2 adsorption–desorption isotherms of calcined MSN were registered. As it can be seen in Figure 5a, a typical curve for MCM-41-like mesoporous solids

was obtained. In particular, a sharp adsorption step was recorded at intermediate P/P_0 values (0.25–0.4). This feature corresponds to a type IV isotherm, indicating the nitrogen condensation inside the mesopores by capillarity. Moreover, the free nitrogen release from the mesopores is confirmed by the absence of a hysteresis loop in this interval, suggesting the presence of uniform cylindrical mesopores. Using the adsorption branch of the porosimetry data, the Barrett–Joyner–Halenda (BJH) model was applied and a narrow pore distribution centred at 2.76 nm was calculated. Furthermore, the application of the Brunauer, Emmett and Teller (BET) model resulted in a value of 1045.7 m^2g^{-1} for the total specific surface of calcined MSN. Taking into account the registered PXRD, porosimetry and TEM studies, an a_0 cell parameter of 4.45 nm and a wall thickness of 1.69 nm were calculated. These values are in agreement with typical MCM-41-type solids. In addition to the adsorption step associated to the micelle generated mesopores, a second feature can also be observed at a high relative pressure (P/P_0>0.85). This adsorption corresponds to the filling of the large voids among the particles and a main pore diameter of ca. 49.63 nm can be calculated in this case by using the BJH model.

N_2 adsorption-desorption isotherms for the capped solids **S1**, **S2** and **S3** showed no remarkable steps at low-intermediate relative pressure values if compared to the calcined MSN. When BET and BJH models were applied lower N_2 adsorbed volume and surface areas were found (see Table 1) for solids **S1**, **S2** and **S3** as expected when compared with the starting MSN supports and due to the partial filling of the mesopores with the cargo.

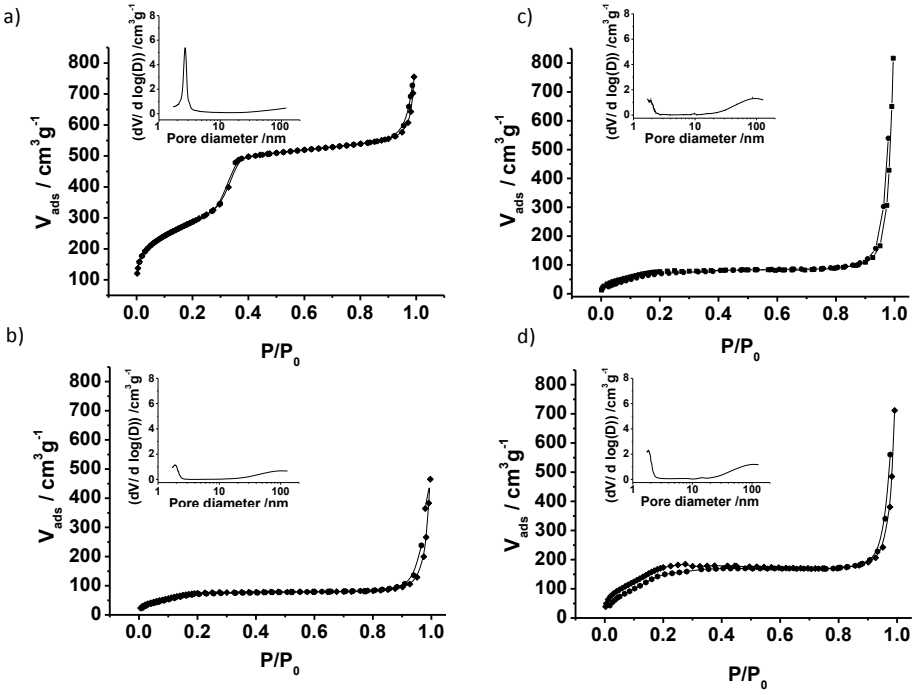

Figure 5. N_2 adsorption–desorption isotherms for a) MSN, b) **S1**, c) **S2** and d) **S3**. Inset: Pore-size distribution for each corresponding solid.

Table 1. BET specific surface values, pore volumes and pore sizes calculated from the N_2 adsorption-desorption isotherms for selected materials.

	S_{BET} (m^2g^{-1})	BJH pore ($P/P_0 < 0.4$)[a] (nm)	Total pore volume[b] (cm^3g^{-1})
MSN	1045.7	2.76	0.90
S1	299.7	2.11	0.16
S2	313.4	2.26	0.17
S3	718.5	1.96	0.16

[a] Pore size estimated by using the BJH model applied on the adsorption branch of the isotherm, for $P/P_0 < 0.4$, which can be associated to the surfactant generated mesopores.

[b] Total pore volume according to the BJH model.

Furthermore, the hydrodynamic diameter of calcined MSN, **S1** and **S2** was determined from Dynamic Light Scattering (DLS) studies (Figure 6). The diameter for calcined MSN was of ca. 94 nm while that found for **S1** was higher (126 nm). An even larger diameter was registered for **S2** (178 nm). These results are in agreement with the functionalization of the MNS and with the larger size of the PEG derivative used to cap **S2** when compared with the PEG used to prepare **S1**.

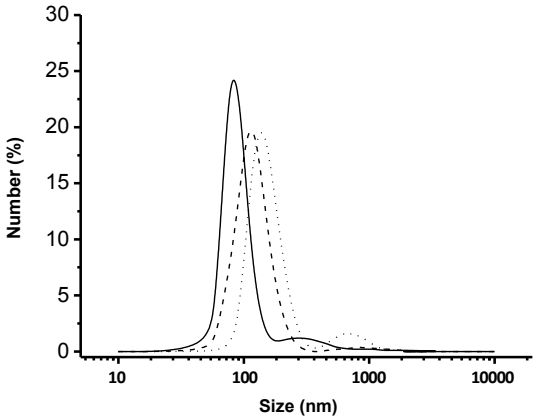

Figure 6. Statistical representation of particle size obtained by DLS (Dynamic Light Scattering) studies for calcined MSN (straight), **S1** (dash) and **S2** (dot).

Finally, the organic content in solids **S1**, **S2** and **S3** was determined by elemental analysis and thermogravimetric studies. Table 2 summarizes all the obtained data. Specifically, a content of 0.11 and 0.21 mmol g^{-1} SiO_2 of safranin O dye in solids **S1** and **S2** respectively and a content of 0.27 mmol g^{-1} SiO_2 of doxorubicin in solid **S3** were obtained. All the obtained values are within the range usually observed in previously reported gated systems.

Table 2. Organic content (α) of loaded molecules and corresponding PEG in mmolg^{-1} SiO_2 for solids **S1**, **S2** and **S3**

Solid	$\alpha_{Safranin\ O}$	$\alpha_{Doxorrubicin}$	α_{PEG}
S1	0.11	--	1.04
S2	0.21	--	0.38
S3	--	0.27	0.63

3.4 Results and discussion

*3.4.1 Delivery studies **S1***

As stated above, it was our aim the design of delivery systems triggered by a reductive environment in cells due to the presence of glutathione. In a first step release experiments in an aqueous solution were carried out with nanoparticles **S1** and **S2**. For example in a typical experiment **S1** material was suspended in water at pH 7.5 both, in the absence and presence of GSH (10 mM). At certain fixed times, aliquots were separated, filtered and the delivery of safranin O dye from the pore voids was observed via monitoring of the fluorescence band of safranin O at 585 nm (λ_{ex} = 520 nm) in the aqueous phase (see Figure 7). Solid **S1** displayed a poor release profile (curve a) in water, whereas it delivered the dye in the presence of GSH (curve b). In particular **S1** nanoparticles were able to remain stable at least for 24 h in a non-reductive environment, whereas in the presence of 10 mM GSH, a fast release of cargo was observed achieving 90% of the maximum release of the entrapped guest, corresponding to a 55% of the total loaded cargo, in less than 1 h. These results indicate that the anchored PEG chains form a dense barrier that inhibits cargo release effectively. In contrast, when GSH is present, the disulfide bond is cleaved allowing the release of the entrapped cargo.

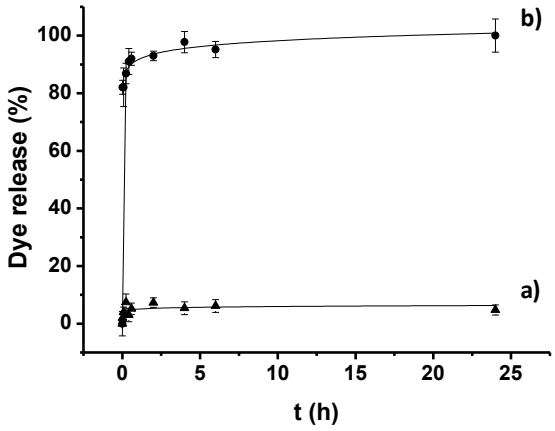

Figure 7. Kinetics of the release of safranin O from gated solid **S1** in water a) in the absence of GSH and b) in the presence of 10 mM GSH.

*3.4.2 Delivery studies **S1** as a function of GSH concentration*

Once proved the suitable behaviour of the capped design, we studied the influence of GSH concentration in the release of safranin O from **S1**. The percentage of safranin O released after 24 h in the presence of different concentrations of GSH is shown in Figure 8. As expected the amount of released safranin O from **S1** was GSH-concentration dependent. Furthermore, stability of **S1** in other competitive media such as phosphate buffered saline (pH 7.4) and simulated body plasma (SBP) was explored. As it can be appreciated in Figure 8, in the absence of GSH the leakage of safranin O from **S1** pore voids was negligible. The results obtained indicated that **S1** would remain tightly capped at typical GSH concentrations in plasma (ca. 2 μM), whereas is expected to display cargo delivery at intracellular GSH concentrations (ca. 10 mM).

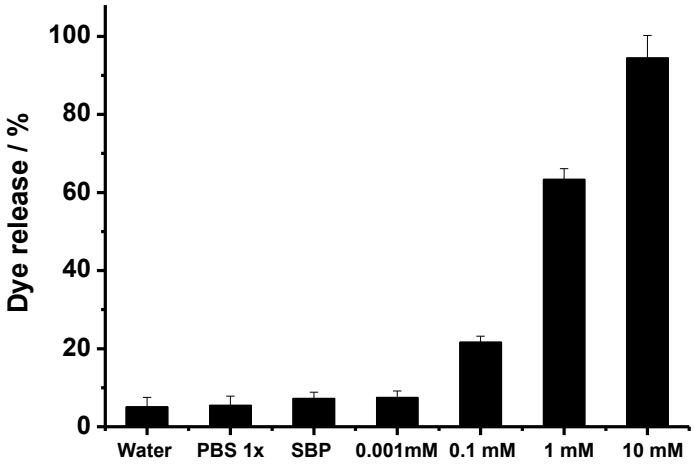

Figure 8. Relative fluorescence intensity of safranin O released from **S1** measured at 580 nm (λ_{ex}=585 nm) in water (pH 7.4), PBS 1x and SBP (pH 7.25), and in water (pH 7.4) as a function of GSH concentration.

3.4.3 Delivery studies **S2**

Using a similar experimental procedure the release behaviour of **S2**, capped with a longer PEG (Mn 800) derivative, was also studied. The difference in emission of safranin O in the presence and absence of GSH is displayed in Figure 9. The release profile of **S2** was very similar to that observed for **S1**; i.e. a poor release in absence of glutathione (curve a) and a fast cargo delivery in the presence of 10 mM GSH. The observed behaviour is consistent with the fact that the disulfide linker is positioned at the same relative distance of the surface as in solid **S1** and therefore both solids display a very similar delivery behavior.

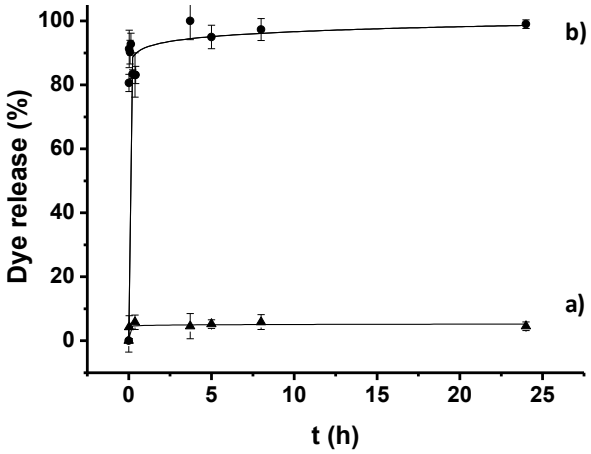

Figure 9. Kinetics of the release of safranin O dye from suspensions of gated solid **S2** in water a) in the absence of GSH and b) in the presence of GSH 10mM.

3.4.4 Delivery studies **S3**

Using a similar experimental protocol, delivery from solid **S3**, containing the drug doxorubicin, was studied in water both in the absence and presence of GSH. In this case cargo delivery was monitored through the fluorescence band of doxorubicin at 557 nm (λ_{exc} = 495 nm). The obtained experimental results are shown in Figure 10. As above a flat baseline was found in the absence of glutathione, while a rapid cargo release was observed in the presence of GSH.

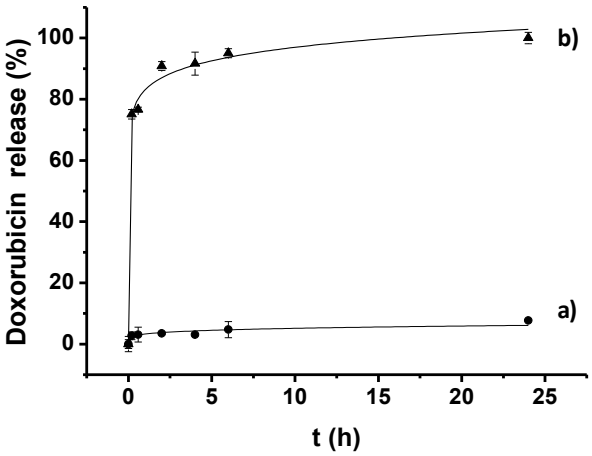

Figure 10. Kinetics of the release of doxorubicin from solid **S3** a) in the absence of GSH and b) in the presence of GSH 10mM.

3.4.5 In vitro studies of the capped materials in cancer cells.

After the in vitro characterization the capped mesoporous **S1** and **S3** nanoparticles were used for further *ex vivo* assays. For these experiments, the tumour cell line HeLa was used. HeLa is an immortal cell line derived from cervical cancer cells. This line is the oldest and most commonly used human cell line in scientific research. Cells were seeded in 6-well culture plates at a density of 150000 cells per well and allowed to adhere for 24 h. After that time, cells were incubated with solid **S1** at a final concentration of 75 μg/mL for additional 24h. In these experiments, cells were also stained with the DNA-associated dye Hoechst 33342. The cellular uptake and intracellular release of **S1** was determined by confocal laser scanning microscopy (CLSM) by tracking safranin O associated fluorescence. As shown on Figures 11A and 11B, safranin O associated fluorescence (red) was clearly observed in the cellular cytosolic compartment indicating the internalization of nanoparticles, the rupture of the disulphide bond by the reductive environment, and the subsequent release of the entrapped dye.
Further studies with **S1** were performed to exclude any toxic effect. HeLa cells were treated with **S1** for 24 h at final concentrations of 20, 50, 150 and 200 μg/mL, respectively. After that time, a cell viability assay using WST-1 was

performed. This yellow reagent (tetrazolium salt) can be reduced by mitochondrial enzymes to give a soluble orange product (formazan salt). This conversion only occurs in viable cells. Therefore, measuring the absorbance at 450 nm against a background control allows an accurate measurement of the number of metabolically active cells in the culture. As expected from previous reports,[13] treatment of cells with **S1** nanoparticles showed non-toxicity effect in concentrations up to 200 µg/ml after 24 hours (Figure 11C).

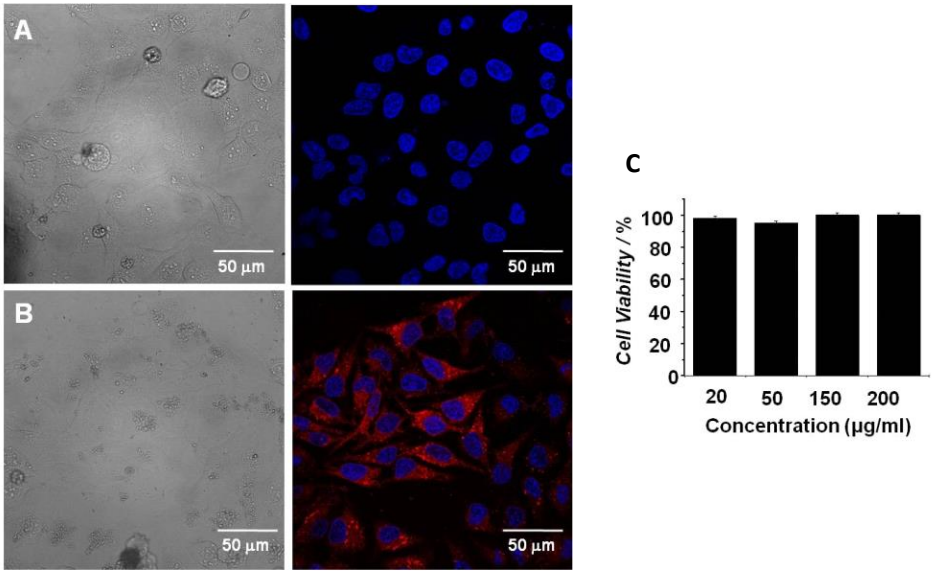

Figure 11. Cell viability and cellular internalization of **S1** gated-nanoparticles. A) Confocal microscopy images corresponding to untreated HeLa cells as a control of autofluorescence, and B) HeLa cells treated with solid **S1** at 75 µg/mL concentration. The cellular uptake of the nanoparticles was evidenced by safranin O associated fluorescence (red) in the presence of DNA marker Hoechst 33342 (blue). C) WST-1 cell viability assay. HeLa cells were incubated for 24 h with **S1** at the indicated concentrations. Cell viability was quantified by employing the WST-1 reagent. Three independent experiments each one done in duplicates were performed and the data are represented as (mean ± SE).

[13] a) E. Aznar, L. Mondragón, J. V. Ros-Lis, F. Sancenón, M. D. Marcos, R. Martínez-Máñez, J. Soto, E. Pérez-Payá, P. Amorós, *Angew. Chem. Int. Ed.* **2011**, *50*, 11172. b) L. Mondragón, N. Mas, V. Ferragud, C. de la Torre, A. Agostini, R. Martínez-Máñez, F. Sancenón, P. Amorós, E. Pérez-Payá, M. Orzáez, *Chem. Eur. J.* **2014**, *20*, 5271.

To further characterize cargo delivery from **S1** in cells we performed a time course experiment of dye release in Hela cells. Accordingly 20 minutes after incubation with **S1** material, cell culture medium was removed and cells were washed with PBS. Then, slides were mounted and visualized by confocal microscopy. Series of images of the same XY field were taken every two minutes. The obtained images revealed that the nanoparticles gradually internalized into cells, and produced a bright red fluorescence that increase in cells as a function of lapsed time (Figure 12).

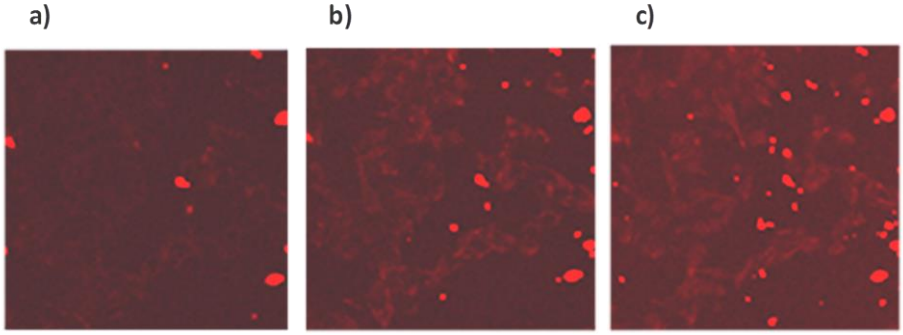

Figure 12. CLSM-fluorescent images of HeLa cells incubated with **S1** for 20 minutes and washed with PBS. Then images of the cells were taken each two minutes. There is shown the images of the kinetics at 0 minutes (a), 20 minutes (b) and 40 minutes (c).

Once studied the intracellular uptake and performance of the gated material **S1**, HeLa cells were also used to demonstrate the possible cellular internalization of **S3** and its ability to release loaded doxorubicin. Doxorubicin treatment causes malfunctioning of the mitochondria by non-specific oxidative damage to the outer and the inner membranes, and by direct interaction with the mitochondrial DNA or enzymes involved in cell respiration.[14] Doxorubicin delivery from **S3** in cells is expected to result in a decrease of cell viability. HeLa cells were treated with 20, 50, 150 and 200 µg/ml of **S3** for 24 h and the cytotoxic effect of the released

[14] a) J. Finsterer, P. Ohnsorge, *Regul Toxicol Pharmacol*, **2013**, 67, 434-445. b)] F. Yang, S.S. Teves, C. J. Kemp, S. Henikoff, *Biochim. Biophys. Acta* **2014**, *1845*, 84-89.

doxorubicin was evaluated by WST-1 assays. As it can be observed in Figure 13C a concentration-dependent decrease in living cells was found when compared to the untreated cells (100% viability). As an example when cells were treated with **S3** at a concentration of 150 µg/ml, around 60% of cells were effectively killed. Furthermore, the cytotoxic effect of **S3** was also clearly noted through changes in cell morphology and cells detachment, when compared with the untreated cells (control, see Figure 13A). CLSM images of HeLa cells incubated with **S3** at a concentration of 75 µg/mL for 24h showed a dotted fluorescent pattern, suggesting the internalization of nanoparticles and the GSH-triggered release of doxorubicin (see Figure 13B).

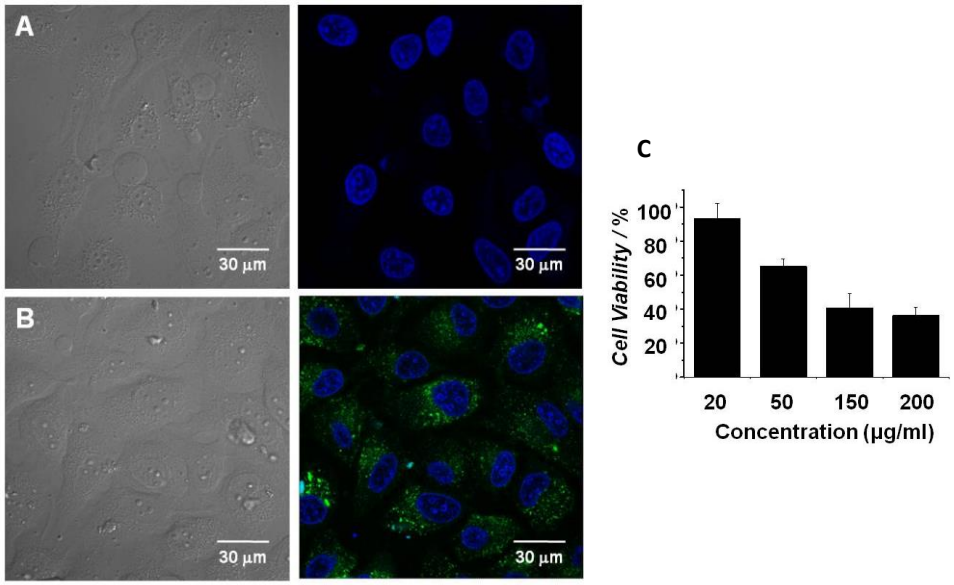

Figure 13. Cellular internalization and cell viability of **S3** gated-nanoparticles. A) Confocal microscopy images corresponding to untreated HeLa cells as a control of autofluorescence, B) HeLa cells treated with solid **S3** at 75 µg/mL concentration for 24h. Cellular uptake of the nanoparticles was evidenced by doxorrubicin associated fluorescence (green) in the presence of DNA marker Hoechst 33342 (blue). C) WST-1 cell viability assay. HeLa cells were incubated for 24 h with **S3** at the indicated concentrations. Three independent experiments were performed and the data are represented as (mean ± SE).

3.5 Conclusions

In summary, we have described herein a new GSH-responsive, simple-to-prepare delivery system based in PEG-capped MSN. More specifically, hybrid materials with the dye safranin O or the anticancer agent doxorubicin as payloads and functionalized with PEG chains of different sizes in the pore entrances, were prepared. The preservation of the mesostructure in the final materials **S1**, **S2** and **S3** and the presence of capped pores were fully confirmed using typical characterization techniques. The performance of the gated systems was assessed by kinetics release studies. The anchored PEG chains formed a dense barrier that inhibits the release of the cargo effectively. In contrast, when GSH was present, the disulfide bonds were cleaved allowing the release of the entrapped cargo. Moreover, as this active group is located near to the silica surface, the loaded safranin O can escape rapidly from the pore voids upon reduction of the S-S bond, achieving 90% of the maximum release of the entrapped guest in less than 1 h for **S1**. Finally, the performance of solids **S1** and **S3** in a cellular context was tested. The uptake of the gated nanoparticles, their aperture in the intracellular reductive environment and their ability to deliver the cargo in a controlled manner was confirmed. The results reported herein confirm that the use of simple disulphide bonds combined with highly hydrophilic and bio-compatible PEG derivatives is an easy way to design capped MSN that remain closed in non-reductive environments (for instance in plasma) yet deliver the cargo in an efficient way in the presence of a high concentrations of GSH (for instance in intracellular media).

3.6 Experimental Section

3.6.1 Chemicals

The chemicals tetraethylorthosilicate (TEOS), *n*-cetyltrimethylammonium bromide (CTAB), sodium hydroxide (NaOH), gluthathione (GSH), safranin O, (3-mercaptopropyl)trimethoxysilane, 2,2'-dipyridyl disulfide , O-(2-mercaptoethyl)-O-methyl-hexa(ethylene glycol) (Mn 350) (mPEG thiol) and poly(ethylene glycol)

methyl ether thiol (Mn 800) were provided by Aldrich. Doxorubicin hydrochloride was provided by Sequoia Research Products. The analytical-grade solvents were provided from Scharlab (Barcelona, Spain). All reactives were used as received.

3.6.2 General Techniques

Powder XRD, TG analysis, elemental analysis, TEM, and N_2 adsorption-desorption techniques were employed to characterize the prepared materials. Powder X-ray measurements were performed on a Philips D8 Advance diffractometer using CuKα radiation. Thermo-gravimetric analysis were carried out on a TGA/SDTA 851e Mettler Toledo equipment, using an oxidant atmosphere (Air, 80 mL/min) with a heating program consisting on a heating ramp of 10 °C per minute from 393 K to 1273 K and an isothermal heating step at this temperature for 30 minutes. Elemental analysis was performed in a CE Instrument EA-1110 CHN Elemental Analyzer. Transmission electron microscope (TEM) images were performed in a Philips CM-10. N_2 adsorption-desorption isotherms were recorded on a Micromeritics ASAP2010 automated sorption analyser. The samples were degassed at 120 °C under vacuum overnight. The specific surface areas were calculated from the adsorption data in the low pressures range using the BET model. Pore size was determined following the BJH method. DLS measurements were performed in a Zetasizer Nano instrument from Malvern. Fluorescence measurements were carried out in a JASCO FP-8500 Spectrophotometer.

Buffer Solutions

Phosphate buffered saline 1x (PBS 1x) consisting in 137 mM NaCl, 1.47 mM KH_2PO_4, 7.85 mM Na_2HPO_4, 2.68 mM KCl (pH 7.5) and simulated body plasma (SBP) prepared with NaCl 137 mM, $NaHCO_3$ 27 mM, KCl 3 mM, $K_2HPO_4.3H_2O$ 1 mM, $MgCl_2.6H_2O$ 1.5 mM, $CaCl_2$ 2.5 mM, Na_2SO_4 0.5 mM, $NH_2C(CH_2OH)_3$ 50 mM and HCl 45 mM were used for controlled release experiences.

3.6.3 Synthesis of the materials

3.6.3.1 *Synthesis of mesoporous MCM-41 nanoparticles*

Mesoporous MCM-41 nanoparticles were synthesised by the following procedure: *n*-cetyltrimethylammonium bromide (CTAB, 1.00 g, 2.74 mmol) was first dissolved in deionized water (480 mL). Then, NaOH (3.5 mL, 2.00 mol L^{-1}) in deionized water was added to the CTAB solution, followed by adjusting the solution temperature to 80 °C. TEOS (5.00 mL, 2.57 x 10^{-2} mol) was then added dropwise to the surfactant solution. The mixture was stirred for 2 h to give a white precipitate. Finally, the solid product was centrifuged, washed with deionized water and ethanol, and dried at 60 °C (MSN as-synthesized). To prepare the final porous nanoparticles (calcined MSN), the as-synthesized solid was calcined at 550 °C using an oxidant atmosphere for 5 h in order to remove the template phase.

3.6.3.2 *Synthesis of **S1** and **S2***

For the preparation of solids **S1** and **S2**, 500 mg of calcined MSN and safranin O dye (140.34 mg, 0.40 mmol) were suspended in distilled water (17 mL) in a round-bottomed flask. The mixture was sonicated in an ultrasonic bath for 10 minutes and stirred for 24 h at room temperature, filtered off and dried under vacuum. Afterward, this loaded solid (250 mg) was re-suspended in acetonitrile (8.5 mL) in the presence of an excess of safranin O and (3-mercaptopropyl) trimethoxysilane (464.38 µL, 2.5 mmol) was added. The suspension was stirred for 5.5 h at room temperature and then, 2,2'-dipyridyl disulfide (550.77 mg, 2.5 mmol) was added to the reaction mixture. After stirring for 12 h at room temperature, the resulting solid was filtered off and dried under vacuum. Finally, a mixture of this prepared solid (50 mg) and O-(2-mercaptoethyl)-O'-methyl-hexa(ethylene glycol) (1.4 mmol) for **S1**, or poly(ethylene glycol)methyl ether thiol (0.15 mmol) for **S2** were suspended in acetonitrile (3.33 mL) in the presence of an excess of safranin O. The mixture was stirred for 12 h and the final materials **S1** and **S2** were isolated by centrifugation, washed with abundant water and dried at 40°C for 12 h. The

prepared solids were easily redispersed by 1 min of mild sonication in an ultrasonic bath.

3.6.3.3 *Synthesis of **S3***

Solid **S3** was prepared following the same procedure described for **S1** but, in this case, MSN was loaded with doxorubicin drug instead of safranin O. In particular 50 mg of calcined MSN and doxorrubicin (10 mg, 0.017 mmol) were suspended in distilled water (0.8 mL) in a round-bottomed flask. The mixture was stirred for 24 h at room temperature, isolated by centrifugation and dried under vacuum. Afterward, this loaded solid was re-suspended in acetonitrile (1.7 mL) and (3-mercaptopropyl) trimethoxysilane (92.87 µL, 0.5 mmol) was added. The suspension was stirred for 5.5 h at room temperature and then, 2,2'-dipyridyl disulfide (136.0 mg, 0.5 mmol) was added to the reaction mixture. After stirring for 12 h at room temperature, the resulting solid was isolated by centrifugation and dried under vacuum. Finally, a mixture of this prepared solid (28 mg) and O-(2-mercaptoethyl)-O'-methyl-hexa(ethylene glycol) (mPEG thiol) (113.12 µL, 0.08 mmol) were suspended in acetonitrile (1.885 mL) and the mixture was stirred for 12 h at room temperature. The final capped solid **S3** was isolated by centrifugation, washed with abundant water and dried under vacuum for 24 h. The prepared solid was easily redispersed by 1 min of mild sonication in an ultrasonic bath.

3.6.4 Dye release studies

Delivery experiments were carried out using the capped materials **S1**, **S2** and **S3**, in the absence or presence of gluthathione (GSH) as reducing agent. In a typical experiment, 0.5 mg of each material were suspended in 1.125 mL of distilled water at pH 7.5. After sonication, 125 µL of the corresponding GSH stock solution were added. The suspension was then stirred and, at a certain time, an aliquot was separated and centrifuged. Dye and drug delivery was monitored through the emission band of safranin O or doxorrubicin centred at 585 nm (λ_{exc} = 520 nm) and 557 nm (λ_{exc} = 495 nm) respectively.

3.6.5 Cell culture conditions

The HeLa human cervix adenocarcinoma cells were purchased from the German Resource Centre for Biological Materials (DSMZ). Hela cells were routinely grown in DEMEM supplemented with 10% FBS, at 37 °C in an atmosphere of 5% CO_2 and underwent passage twice a week.

3.6.6 WST-1 cell viability assay

Cells were cultured in sterile 24–well microtiter plates at a seeding density of 25 x 10^3 cells/well for HeLa and were allowed to settle for 24h. **S1** or **S3** was added to the cells at a final concentrations of 20, 50, 150 and 200 µg/mL. After 22 h, WST-1 (30 µL of a 50 mg/ml solution) was added to each well. Cells were further incubated for 2 h (a total of 24 h of incubation was therefore studied), and then shaked thoroughly for 1 minute on a shaker. After that, absorbance was measured at 450 nm against a background control as blank using a microplate ELISA reader. The reference wavelength was 690 nm.

*3.6.7 Live confocal microscopy **S1** and **S3** cellular internalization assays*

HeLa cells were seeded in 24 mm glass coverslips in 6-well microliter plates at a seeding density of 1.5 x 10^{-5} cells/well. After 24 hours, cells were treated with 75 µg/ml of **S1** or **S3**. After 20 minutes, the medium was removed to eliminate compounds and washed with PBS. Then, cells were incubated during 20 hours at 37 °C, and were visualized under a confocal microscope. Confocal microscopy studies were performed with a Leica TCS SP2 AOBS (Leica Microsystems Heidelberg GmbH, Mannheim, Germany) inverted laser scanning confocal microscope using oil objectives: 63X Plan-Apochromat-Lambda Blue 1.4 N.A. Two-dimensional pseudo colour images (255 colour levels) were gathered with a size of 1024x1024 pixels and Airy 1 pinhole diameter. All confocal images were acquired using the same settings. Identical experiments were done three times to obtain reproducible results.

4. Gated mesoporous silica nanoparticles for the controlled delivery of drugs in senescent cells

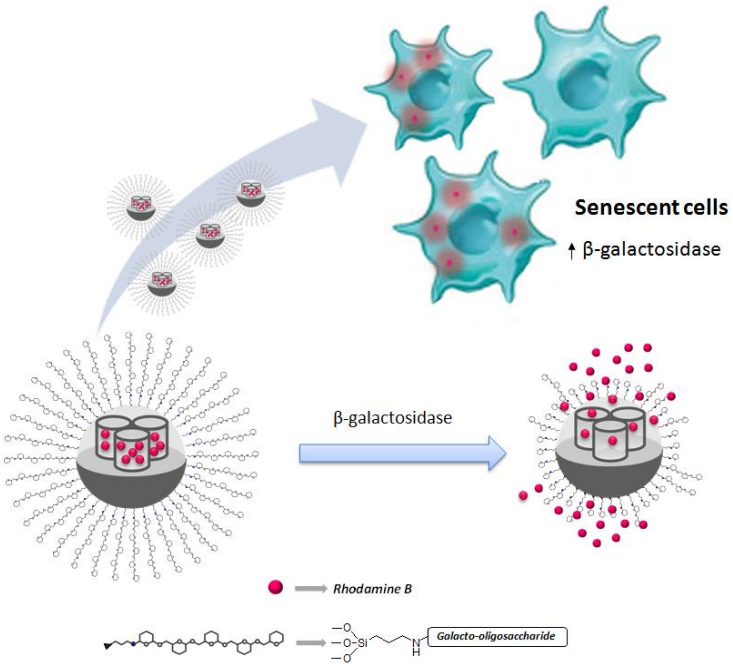

4.1 Introduction

The concept of cellular senescence was introduced in 1961 by Hayflick and Moorhead[1] when they showed that, in contrast to cancer cells, normal cells had a finite proliferative capacity in culture. The authors observed that after many cell doublings, human fibroblasts finally lost the ability to divide but remained viable for many weeks, living in a stable cell cycle arrest characterized by a lack of response to growth factors, sustained metabolic activity and changes in cell morphology[2]. They named this phenomenon "cellular senescence" and related it with the ageing of cells.

Today, it is known that cellular senescence is a state of permanent cell-cycle arrest that proliferating cells can adopt in response to cellular stresses as a measure to avoid the replication and proliferation of damaged cells. Thus, like apoptosis, senescence can be considered as an emergency defence system for elimination of unwanted cells. Several events have been demonstrated to induce the senescent phenotype such as oncogene activation, telomere shortening, oxidative stress, DNA damage, and/or the action of cytotoxic drugs. In addition, senescent cells present several markers such as the absence of proliferative markers, senescence-associated β-galactosidase (SAβ-Gal) activity, expression of tumour suppressors and cell cycle inhibitors and morphological changes.

D. Muñoz-Espín and M. Serrano[3] proposed that senescence is a key component of tissue remodelling both in normal development and physiology, and in multiple pathologies. They propose a unified model by which cellular senescence orchestrates tissue remodelling through three sequential processes. As a first step, senescent cells arrest their own proliferation in response to damage. Secondly, the senescence-associated secretory phenotype (SASP) recruits immune

[1] L. Hayflick, P. S. Moorhead, *Exp. Cell Res.,* **1961**, *25*, 585.

[2] a) A. Collad, M.Serrano. *Nature*, **2010**, *10*, 51. b) J. Campisi, F. d'Adda di Fagagna, *Nat. Rev. Mol. Cell Bio.*, **2007**, *8*, 729.

[3] D. Muñoz-Espín, M. Serrano, *Nature Rev. Mol. Cell Biol.,* **2014**, *15*, 482.

cells, including T-helper lymphocytes and macrophages that mediate clearance of senescent cells. Finally, the mobilization of nearby precursors repopulates and regenerates the damaged tissue.

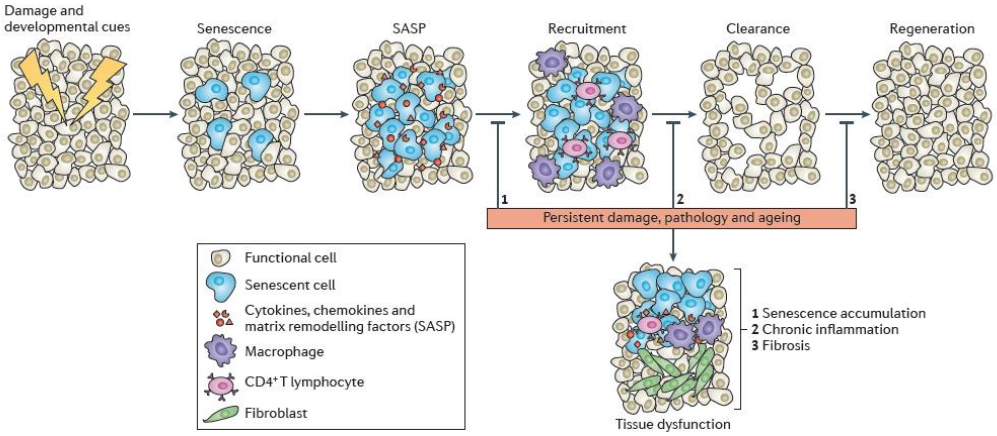

Figure 1. Unified model of senescence. *Reprinted with permission from Nat Rev Mol Cell Biol.* **2014**, *15*, 482. *Copyright © 2014, Rights Managed by Nature Publishing Group*

This model allows the restoration of damaged tissue in some cases. However, this sequence of events (senescence, followed by clearance and then regeneration) may not be efficiently completed upon persistent damage, in pathological contexts or ageing, thereby resulting in the accumulation of senescent cells and become part of the problem. This favours a chronic inflammation in part by the SASP and results in fibrosis and tissular dysfunction.[5]

In fact, during the last few years cellular senescence has been found in association with multiple chronic pathologies, including pulmonary and liver fibrosis, atherosclerosis, cardiac fibrosis after myocardial infarction, obesity, type 2 diabetes, renal diseases and neurological disorders, in which senescence have been reported to have beneficial effects (limit the extent of the pathological process) or detrimental effects (senescence contributes to the pathology). [5]

Thus, strategies to detect, remove or reprogramme senescent cells are of fundamental interest both for basic research and clinical applications. The detection *in vivo* of senescent cells is a powerful tool to diagnose senescent associated pathologies. In addition, J. M. van Deursen[4] demonstrated, for the first time, the beneficial effects of senescent cell removal from a genetically engineered progeroid mouse model with high levels of constitutive damage. In their study, they showed that the removal of p16-positive senescent cells rejuvenated some damaged tissues, such as muscle and fat, and avoided cataract.

In this context our group reported gated MSNs capable to release their payload in senescent cells with lack of toxicity. Our strategy involved the use of MSNs capped with a galactoligosaccharide (GOS) and the specific presence of SAβ-Gal enzyme in senescent cells.[5] As a first step, we demonstrated the target release of a fluorophore in β-galactosidase (β-Gal) overexpressing yeast cells and in human senescent cells (fibroblasts from X-linked Dyskeratosis Congenita patients).

Motivated by these encouraging results, we proposed to validate the nanodevice as drug delivery system for senescent cells *in vivo*. For this purpose we selected a murine model of Idiopathic Pulmonary Fibrosis (IPF).

The IPF is a chronic progressive interstitial lung disease with increasing prevalence, high mortality rates and poor treatment options. The diagnostic process is complex and often requires an interdisciplinary approach between different specialists. Despite many well-designed multicenter trials, no medical therapies have been found to be definitively effective for IPF. Therefore, there is an urgent need for new therapies and also for validation of prognostic markers that predict disease progression, survival and also response to antifibrotic drugs.

---

[4] D. J. Baker, T. Wijshake, T. Tchkonia, N. K. LeBrasseur, B. G. Childs, B. van de Sluis, J. L. Kirkland,J. M. van Deursen, *Nature,* **2011**, *479*, 232–236

[5] A. Agostini, L. Mondragón, A. Bernardos, R. Martínez-Máñez, M. D. Marcos, F. Sancenón, J. Soto, A. Costero, C. Manguan-García, R. Perona, M. Moreno-Torres, R. Aparicio-Sanchis and J. R. Murguía, *Angew. Chem. Int. Ed.* **2012**, *51*, 10556.

Recent published evidence links the pathogenesis of IPF with increased alveolar senescence and premature lung ageing.[6] The senescence hypothesis for IPF is supported by a variety of studies demonstrating telomere length abnormalities, as well as the *in situ* expression of senescent related cell cycle regulators such as p21 and p16.

In a first step, the selectivity and targeted delivery of GOS capped nanoparticles in senescent cells were studied with the cellular line ITM.[7] This new cell line exhibit induced senescence when it is treated with oestrogen analogue 4-hydroxytamoxifen (4OHT). Once validated in this senescent cellular model, we focused on implementing the *in vivo* use of MSNs to target specifically senescent cells in fibrotic lungs of an IPF murine model.

4.2 Objectives

Bearing in mind the concepts exposed below, our objectives in this chapter were to validate the *in vivo* use of the GOS capped MSNs to target specifically senescent cells in fibrotic lungs. Specifically, our objectives were:

- ✓ Synthesize and characterize GOS gated nanoparticles and nanoparticles capped with a saccharide derivative as a control nanodevice.
- ✓ Validate the targeted delivery in the senescent cellular model ITM.
- ✓ Evaluate the feasibility of GOS capped MSN to target senescent cells *in vivo* in IPF murine model.

[6] A.R. Tsang, H.D. Wyatt, N.S. Ting, T.L. Beattie, *Aging Cell*, **2012**, *11*,482

[7] M. Collado, J. Gil, A. Efeyan, C. Guerra, A. J. Schuhmacher, M. Barradas, A. Benguria, A. Zaballos, J. M. Flores, M. Barbacid, D. Beach and M. Serrano, *Nature*, **2005**, *436*, 642.

4.3 Synthesis and Characterization

4.3.1 Design of the system

The designed capped support is depicted in Figure 2-a. It is based on the use of mesoporous silica nanoparticles loaded with a suitable reporter (i.e. rhodamine b dye) and capped with galacto-oligosaccharide derivative chains (**MSN-GOS**). Our strategy involved the presence of β-Gal enzyme, a glycoside hydrolase enzyme which hydrolyzes the β-glycosidic bond, as triggering event. The overexpression of the endogenous lysosomal β-Gal that specifically occurs in senescent cells (SAβ-Gal) has been reported[8] and widely used as a senescent marker.

Therefore, we proposed that GOS-capped mesoporous nanoparticles may show "zero release", yet would selectively release their cargo in senescent cells because of β-galactosidase-mediated hydrolysis of the cap (Figure 2-a)

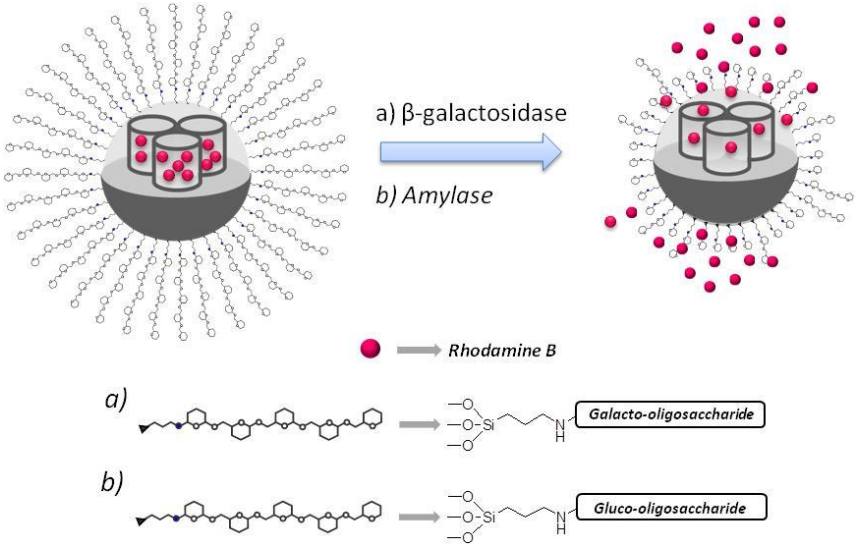

Figure 2: Representation of nanoparticles capped with a galacto-oligosaccharide (GOS) and the selective delivery mechanism in the presence of β-gal enzyme (a), and nanoparticles capped with gluco-oligosaccharides and dye delivery triggered by amylase enzyme (b).

[8] D. J. Kurz, S. Decary, Y. Hong, J. D. Erusalimsky, *J. Cell Sci.,* **2000**, *113*, 3613.

In addition, in order to carry out control experiments to verify the specificity of the **GOS-MSN** delivery system, mesoporous silica nanoparticles capped with gluco-oligosaccharides derivatives were also prepared (**Glu-MSN**). This nanodevice[9] rely on MSN loaded with the same fluorophore and capped with a hydrolyzed starch derivative. In this case, the anchored moieties were expected to inhibit cargo delivery until the presence of amylase enzyme located in cells lysosomes. Amylase is able to hydrolyze the 1➔4 glycosidic bond between β-D-glucoses present in the starch (Figure 2-b).

4.3.2 Synthesis of the materials

- GOS-MSN

For the preparation of the final capped nanodevice (**GOS-MSN**), MCM-41-based MSNs were selected as the inorganic scaffold. MCM-41 nanoparticles were prepared following out standard procedures. In a second step, calcined MSNs were suspended in a solution of rhodamine-B dye in order to achieve the maximum loading in the pores and then reacted with the capping oligosaccharide derivative. The capping molecule was prepared starting from a commercially available GOS oligomer which was first brought to pH 7.0 and then reacted with 3-aminopropyltriethoxysilane to give the corresponding alkylgluconamine derivative (GOS-d).

- Glu-MSN

In a similar procedure, to synthesize the material **Glu-MSN**, calcined MCM-41 nanoparticles were first suspended in a solution of rhodamine B dye in order to load the pores. In this case the capping molecule was prepared starting from a commercially available Glucidex-47 oligolymer which was first brought to pH 7.0 and then reacted with 3-aminopropyltriethoxysilane to give the corresponding alkylgluconamine derivative (Glu-d).

[9] A. Bernardos, L. Mondragón, E. Aznar, M. D. Marcos, R. Martínez-Máñez, F.Sancenón, J. Soto, J. M. Barat, E. Pérez-Payá, C. Guillem, P. Amorós, *ACS Nano,* **2010,** *4*, 6353.

4.3.3 Characterization

All mesoporous nanoparticles were characterized following standard techniques. The powder X-ray diffraction (PXRD) pattern of the different synthesized solids is shown in Figure 3. In relation to the siliceous MCM-41 nanoparticles as synthesized, the four low-angle reflections typical of a hexagonal array, indexed as (100), (110), (200), and (210) Bragg peaks were observed (curve a). The PXRD of calcined MSN (Figure 1b) shows a significant displacement of the (100) peak, that can be attributed to an approximate cell contraction of 4 Å. This displacement found in calcined MSN is related to further condensation of silanol groups during the calcination step (curve b). Finally, the PXRD pattern of both functionalized solids **GOS-MSN** and **Glu-MSN** can be found in curves c) and d), respectively. An intensity decrease and practically loss of the (110) and (200) reflections is appreciated, related to a loss of contrast due to the filling of the pore voids with the rhodamine B dye and the external surface functionalization. Even so, the presence of the (100) peak in this pattern strongly indicates that the mesoporous structure of the MCM-41 scaffold has not been modified after the loading and functionalization processes in the final materials.

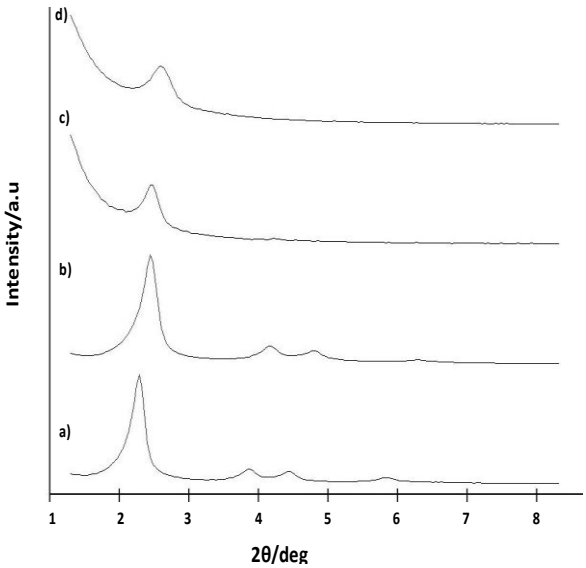

Figure 3. Powder X-Ray pattern of (a) MCM-41 as made, (b) MCM-41 calcined and (c) **GOS-MSN** material and (d) **Glu-MSN** material.

Moreover, the presence of the mesoporous structure was confirmed by TEM analysis of the prepared solids. As it can be observed in Figure 4, the typical channels of the MCM-41 matrix can be visualised as alternate black and white stripes in which the typical hexagonal porosity of the MCM-41 calcined material can also be observed (Figure 4 b). TEM images also show that the prepared MCM-41-based support is obtained as spherical nanoparticles with diameters ranging from 80 to 100 nm.

Preservation of the mesoporous structure in the final functionalized solids **GOS-MSN** and **Glu-MSN** was also confirmed by TEM (Figure 4 c and d respectively). In these images, although the contrast between the black and white strips has decreased due to the loading of the pores and surface functionalization, it can be confirmed that the spherical shape of the nanoparticles and their typical mesoporous structure remains.

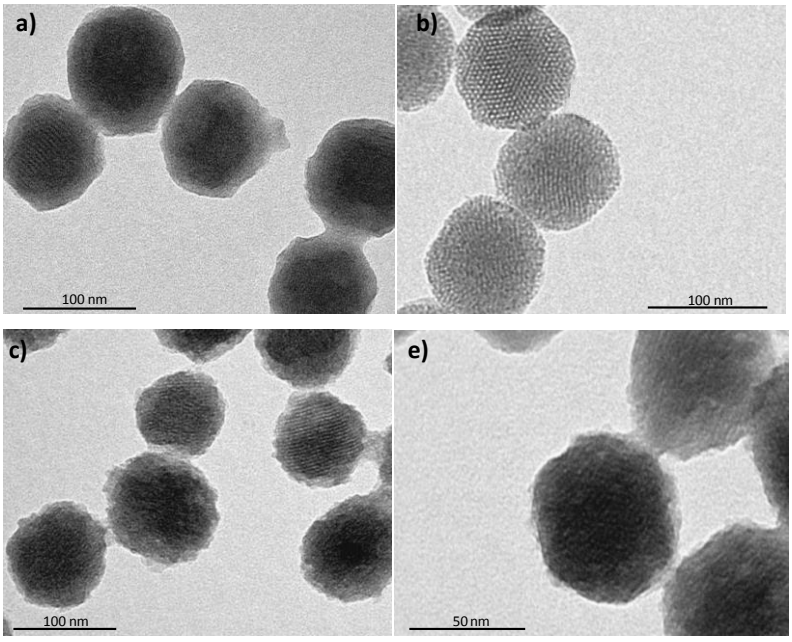

Figure 4. Representative TEM image of a) the inorganic as made MCM-41 matrix, b) calcined MCM-41 nanoparticles, c) **GOS-MSN** gated material and d) **Glu-MSN** material.

N_2 adsorption-desorption isotherms for calcined MCM-41 nanoparticles and the gated solids **GOS-MSN** and **Glu-MSN** were registered and are shown in Figure 5. Curve a) corresponds to the calcined matrix showing a sharp adsorption step with a P/P_0 value between 0.2 and 0.4, corresponding to a type IV isotherm, typical of these mesoporous materials. This first step is due to nitrogen condensation in the mesopore inlets. With the BJH model on the adsorption curve of the isotherm, the pore diameter and pore volume were calculated to be 2.51 nm and 0.72 $cm^3\ g^{-1}$, respectively. The absence of a hysteresis loop in this pressure range and the low BJH pore distribution (see inset in Figure 5 a) is due to the cylindrical uniformity of mesopores. The total specific area was 995.6 $m^2\ g^{-1}$, calculated with the BET model. Also using the a_0 cell parameter (4.17 nm) calculated from PXRD measurements and the pore diameter (2.51 nm), a wall thickness value of 1.66 nm, was calculated. Other important feature of the curve is the characteristic H1 hysteresis loop that appears in the isotherm at a high relative pressure (P/P_0> 0.8) which can be closely associated with a wide pore size distribution which corresponds to the filling of the large pores among the nanoparticles due to textural porosity. In the case of the final **GOS-MSN** material, the N_2 adsorption desorption isotherm is typical of mesoporous systems with filled mesopores (see Figure 5, curve b). In this way, and as it was expected, a lower N_2 adsorbed volume (BJH mesopore volume = 0.43 $cm^3\ g^{-1}$) and surface area (197.1 $m^2\ g^{-1}$) were determined, when compared with the initial MCM-41 material. As it can be observed in the curve, this solid presents a function with no gaps at low relative pressure values if compared to the mother MCM-41 array (curve a). A remarkable data is that **MSN-GOS** did not show a maximum in the pore size distribution curve, which can be explained by the presence of closed pores because of the entrapped dye and the functionalization moieties in the external surface. Similarly, the N_2 adsorption desorption isotherm of **Glu-MSN** material shows also a low N_2 adsorbed volume (BJH mesopore volume = 0.26 $cm^3\ g^{-1}$), and a low surface area (131.9 $m^2\ g^{-1}$) compared to the mother MCM-41 material. In addition, as in the case of **GOS-MSN**, the **Glu-MSN** material did not show a maximum in the pore size distribution curve. These results suggest that the loading and

functionalization processes were carried out effectively and the pores are blocked.

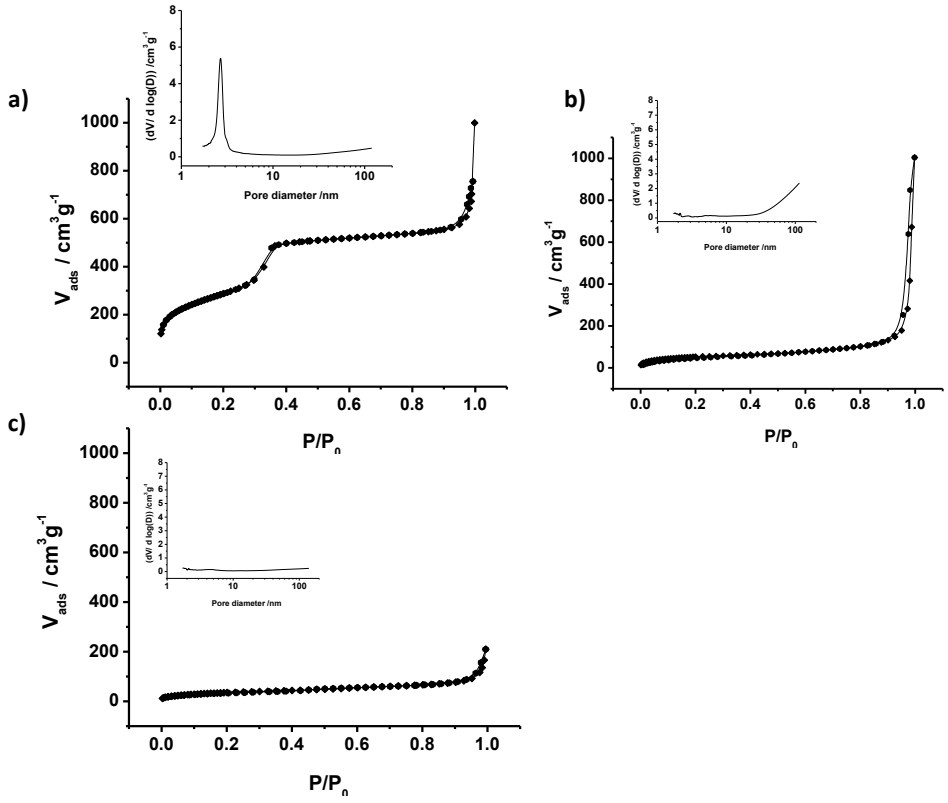

Figure 5. Nitrogen adsorption-desorption isotherms for (a) calcined MCM-41 mesoporous material (b) **GOS-MSN** gated material and (d) **Glu-MSN** material. Inset: Pore size distribution of each material.

BET specific surface values, pore volumes, and pore sizes calculated from the N_2 adsorption–desorption isotherms for MCM-41, **GOS-MSN** and **Glu-MSN** are listed in Table 1. It can be seen that **GOS-MSN**, and **Glu-MSN** solids show similar specific surface, pore volume, and pore size values that are indicative of similar pore blocking, due to the cooperative effect of guest molecules and functional groups in both active materials.

Table 1. BET specific surface values, pore volumes and pore sizes calculated from the N_2 adsorption-desorption isotherms for selected materials.

	S_{BET} (m^2g^{-1})	BJH pore ($P/P_0 < 0.4$)[a] (nm)	Total pore volume[b] (cm^3g^{-1})
MSN	995.6	2.51	0.72
GOS-MSN	197.1	---	0.43
Glu-MSN	131.9	---	0.26

[a] Pore size estimated by using the BJH model applied on the adsorption branch of the isotherm, for $P/P_0 < 0.4$, which can be associated to the surfactant generated mesopores.

[b] Total pore volume according to the BJH model.

The content of organic matter in the final hybrid solids **GOS-MSN** and **Glu-MSN** were calculated by elemental and thermogravimetric analysis. Values are detailed in Table 2. In addition, the content of rhodamine B in both **GOS-MSN**, and **Glu-MSN** solids were also determined by UV-visible studies; the content of the dye present in the washing solutions of each solid was quantified and subtracted to the quantity used in their loading process.

Table 2. Organic content (α) of loaded molecules and corresponding capping molecule in mg g^{-1} SiO_2 for solids GOS-MSN and Glu-MSN.

Solid	$\alpha_{Rhodamine\ B}$	$\alpha_{capping\ molecule}$
GOS-MSN	76.64	110.59
Glu-MSN	95.80	72.91

4.4 Results and discussion

4.4.1 Delivery studies

The prepared nanodevice **GOS-MSN** and the control solid **Glu-MSN**, are composed of a mesoporous matrix, containing rhodamine B in the pores and capped with galacto-oligosaccharide and gluco-oligosaccharides moieties respectively. It was expected that the capping molecules would block the pores and would subsequently avoid cargo delivery. Furthermore, the presence of the corresponding enzyme may induce saccharide hydrolysis and release of the entrapped guest. In order to confirm the designed aperture mechanism of the gated nanoparticles, release kinetics studies were carried out.

4.4.1.1 *Delivery studies of GOS-MSN material*

Studies of the delivery of the rhodamine B cargo from the **GOS-MSN** in water in the presence and absence of β-Gal were performed (Figure 6). For these studies, the enzyme β-Galactosidase from *Kluyveromyces lactis* was used.

In a typical experiment, **GOS-MSN** material was suspended in water at pH 7.5 and β-Gal enzyme was added. The suspension was then stirred and the amount of dye released was determined by monitoring the emission of the rhodamine B in the solution as a function of time (λ_{ex} = 550 nm, λ_{em} = 580 nm). The same procedure was performed without adding the enzyme. In the absence of the enzyme β-Gal a flat baseline was found indicating that rhodamine B remained in the nanoparticles without release. In contrast, in the presence of β-Gal, release of the cargo was shown as an increase of the rhodamine B fluorescence as a function of time. This behavior was assigned to the galactosidase-induced hydrolysis of the glycosidic bonds of the anchored GOS derivative, which results in a reduction of the size of the attached groups allowing delivery of the entrapped dye.

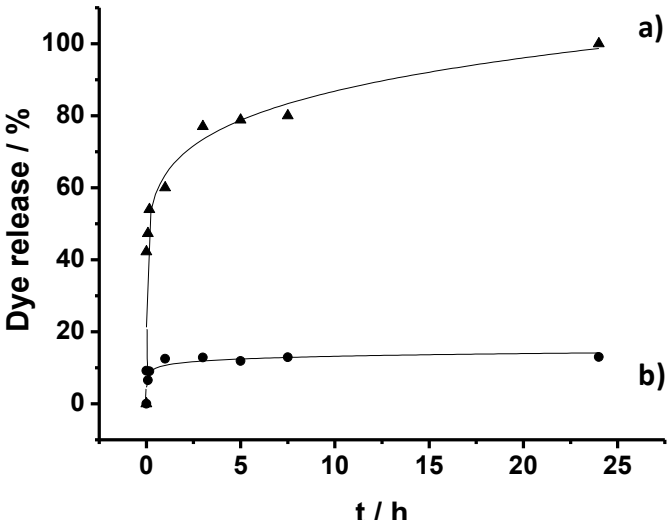

Figure 6. Release profiles of rhodamine-b dye from **GOS-MSN** in the absence (a) and in the presence (b) of β-Gal enzyme in water at pH 7.5 at room temperature.

4.4.1.2 *Delivery studies of Glu-MSN material*

In a similar procedure, the delivery of rhodamine B from **Glu-MSN** material was studied in the presence and in the absence of amylase enzyme. For these studies, pancreatin from porcine pancreas (a mixture of amylase, lipase, and proteases) was used. **Glu-MSN** material was suspended in water at pH 7.5 and the enzymatic mixture pancreatin was added. The amount of dye released was determined by monitoring the emission of the rhodamine B in the solution as a function of time (λ_{ex} = 550 nm, λ_{em} = 580 nm). As a control experiment, dye release was also determined by using of suspensions of **Glu-MSN** under similar conditions but in the absence of pancreatin. The difference in dye delivery in both experiments is displayed in Figure 7. As can be seen, in the absence of esterase a low release of the rhodamine B dye was observed. However, in the presence of pancreatin a high release of the dye was found as a consequence of the enzyme-induced hydrolysis of the anchored gate.

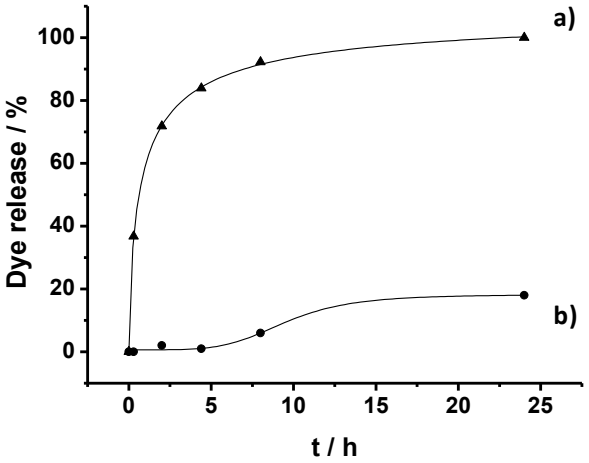

Figure 7. Release profiles of rhodamine b dye from **Glu-MSN** in the absence (a) and in the presence (b) of pancreatin in water at pH 7.5 at room temperature.

4.4.2 Delivery studies of the capped materials in ITM cells.

After confirming the effective release of rhodamine B from capped materials **GOS-MSN** and **Glu-MSM** in the presence of β-Gal and pancreatin enzymes, respectively, cargo release studies in the cellular line ITM7 were performed. This cell line exhibit oncogene-induced senescence (OIS) as a response when it is treated with oestrogen analogue 4-hydroxytamoxifen (4OHT).

To perform the experiments, cells were seeded and treated for 72h with 4OHT as reported,[7] in order to induce senescence with 80-100% of efficiency. Senescence is accompanied by phenotypic and transcriptional changes that identify senescent cells *in vivo*. As can be seen in Figure 8, treated cells showed significant changes in morphology: cells acquired a more rounded shape about their elongated morphology usual spindle shaped and become smaller. These phenotypic changes are indicative of cellular senescence.

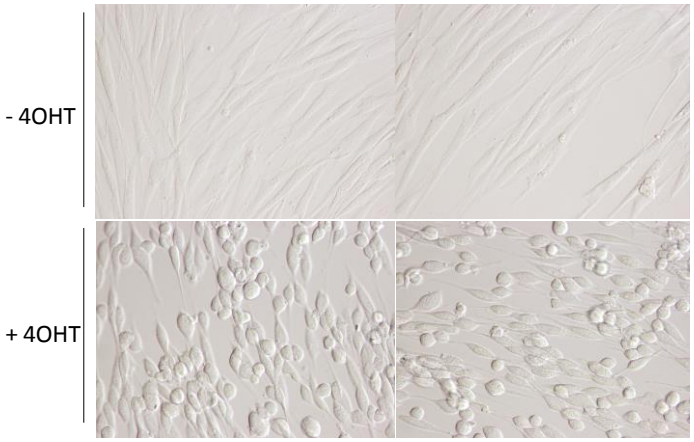

Figure 8: Optical microscope images of ITM cells untreated (-4OH) and treated (+4OHT) with 4-hydroxytamoxifen 100 nM for 72h.

4.4.2.1 *Validation of the GOS-MSN targeted delivery in senescent cells*

The selectivity and targeted delivery of GOS capped nanoparticles in senescent cells were evaluated in ITM cells. Fluorescence microscope analyses were used to evaluate the internalization in senescent and no senescent cells by tracking rhodamine B associated fluorescence. For these studies, ITM cells were seeded and treated for 72h with 4OHT 100 nM (senescence cells, +4OHT) or seeded and maintained without treatment (control cells, -4OHT). Then, cells were treated with **GOS-MSN** nanoparticles at a final concentration of 50 μg/mL for 24h and examined for rhodamine B staining by fluorescence microscopy. Additionally, to confirm the effective induction of senescence, a visual assay of β-Gal activity was carried out. For this assay, cells were treated with the senescence β-Gal staining kit that contains the x-gal marker. X-gal staining (in blue) gives a histochemical detection of lysosomal β-GAL activity at a suboptimal pH (pH 6.0).8

As shown in Figure 10, senescence was efficiently induced in cells treated with 4-hydroxytamoxifen (+4OHT) which was noted through the expected changes in phenotype and the x-gal staining (blue) that confirms the overexpression of the senescence associated β-Gal enzyme. Remarkably, induced senescent cells (+4OHT) presented high levels of rhodamine B associated fluorescence when compared with control cells. These results show that, despite the fact that GOS

capped MSNs most likely internalized in both control and senescent cells, they release their cargo to a greater extent within SAβ-Gal overexpressing cells.

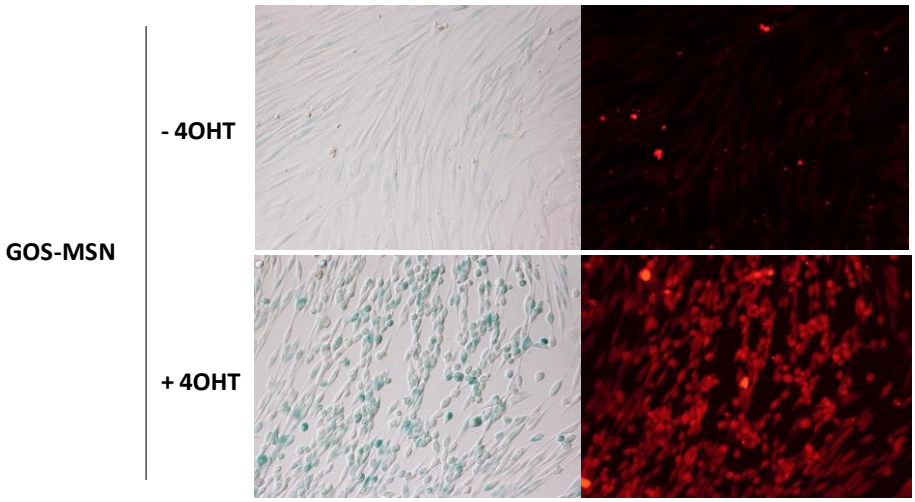

Figure 10. Microsope images of control cells (-4OHT) and senescent cells (+4OHT) treated with **GOS-MSN** (50 μg mL^{-1}) for 24h and stained with the β-Galactosidase activity marker x-gal (blue staining). Images of rhodamine B (red staining) by fluorescence microscopy (right) and differential interference contrast (DIC) microscopy (left) are shown.

Additionally, to demonstrate that the higher signal of rhodamine B staining in +4OHT cells was not an artifact of the conditions used, additional control experiments were performed. The same experiments to those described above were carried out using the prepared rhodamine-loaded MSN nanoparticles capped with hydrolyzed starch **Glu-MSN**. In this case it is expected that both control and senescent cells internalize **Glu-MSN** and trigger their cargo release in a similar way. As it is observed in Figure 11, clearly detectable rhodamine B staining was observed in both control (-4OHT) and senescent (+4OHT) cells. These results confirmed that rhodamine B release from **GOS-MSN** is ascribed to a selective cellular β-Gal enzyme-mediated mechanism.

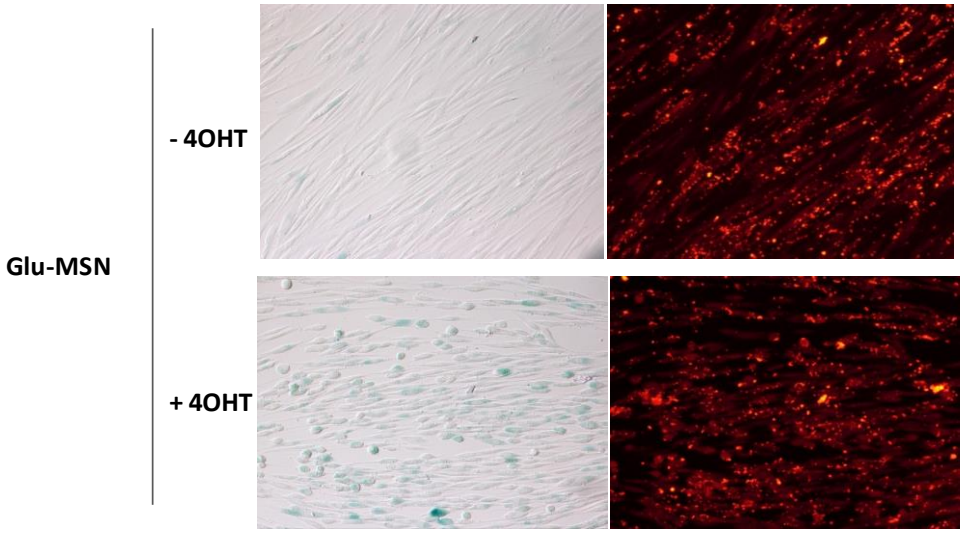

Figure 11. Microsope images of control cells (-4OHT) and senescent cells (+4OHT) treated with **Glu-MSN** (50 μg mL^{-1}) for 24h and stained with the β-Galactosidase activity marker x-gal (blue staining). Images of rhodamine B (red staining) by fluorescence microscopy (right) and DIC microscopy (left) are shown.

Confocal microscopy analyses were used to confirm the internalization of capped nanoparticles and to quantify cargo release differences between senescent and control cells by tracking rhodamine B fluorescence. In these experiments, cells were cultured and treated (+4OHT) or untreated (-4OHT) with 4OHT for 72h. Then cells were treated with the corresponding capped nanoparticles for 6h and examined by confocal microscopy. Additionally, cell nuclei were stained with DAPI. Diffuse fluorescent signal associated with intracellular rhodamine B release was observed (Figure 12) which suggests the internalization of nanoparticles. In these experiments, as in the case of the fluorescence microscope analyses, senescent cells exhibited a higher level of rhodamine B than control cells when they are treated with **GOS-MSN** (Figure12 A). In contrast, **Glu-MSN** presented the same internalization in senescent and control cells (Figure 12 C). Moreover, the fluorescence signal differences were quantified through the image analyses with Image J software.

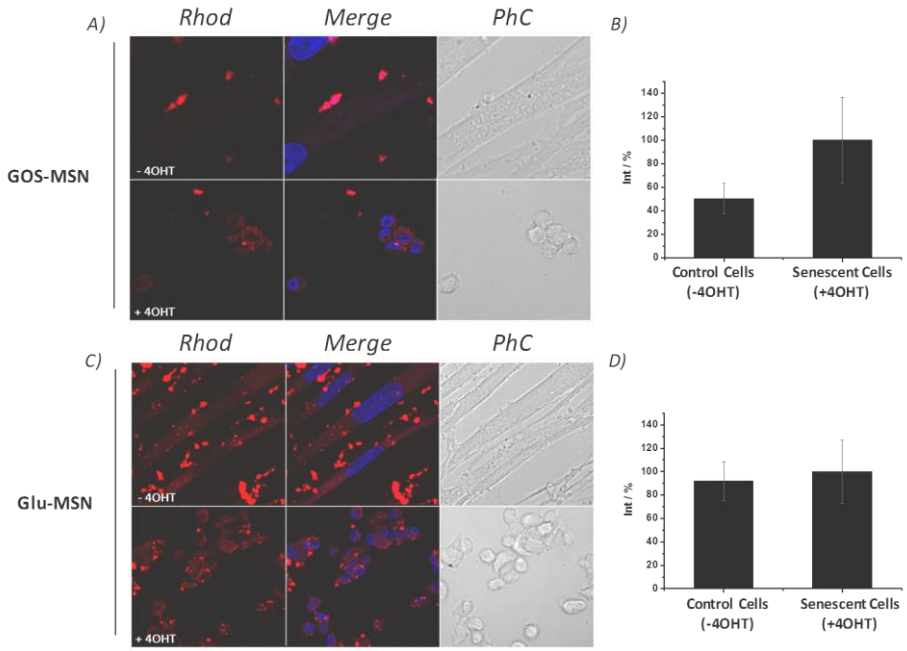

Figure 12. Internalization and release of cargo in control and senescent cells. A) Control (-4OHT) and induced senescent cells (+4OHT) were treated with **GOS-MSN** (50 μg mL^{-1}). Representative images at 6 h from phase contrast (PhC), Rhodamine (Rhod), and combined (Merge) are shown. B) Quantitation of rhodamine fluorescence intensity (% Int) of cells treated with **GOS-MSN** referenced on the maximum observed in the trial , as mean ± s intensity. C) Control (-4OHT) and induced senescent cells (+4OHT) were treated with **Glu-MSN** (50 μg mL^{-1}). Representative images at 6 h are shown. D) Quantitation of rhodamine fluorescence intensity (% Int) of cells treated with **Glu-MSN**, referenced on the maximum observed in the trial , as mean ± s intensity.

4.4.3 In vivo studies of the capped materials in IPF murine model

Once validated **GOS-MSN** in the senescent cellular model ITM, we focused on implementing the *in vivo* use of MSNs to target specifically senescent cells associated with IPF pathogenesis. For the studies *in vivo*, an animal model of pulmonary fibrosis by injection with the radiomimetic drug bleomycin was used. Bleomycin is a member of the glycopeptide antibiotic family that exerts potent antitumor activity. Nevertheless, bleomycin induces DNA strand breaks as a cytotoxic effect that triggers apoptosis and senescence as a response, which finally results in pulmonary inflammation, injury, and subsequent interstitial fibrosis. The intratracheal instillation (IT) of bleomycin into rodents is widely used

as an *in vivo* experimental model of pulmonary fibrosis owing to this model recapitulates all the phenotypic and metabolic alterations associated with IPF.[10]

Despite the fact that the induction of the SASP of alveolar epithelial cells in bleomycin-induced pneumopathy has been described[11], the presence of senescence in lungs after bleomycin treatment of mice was studied before to perform *in vivo* assays (see Figure 13). For this study, mice were treated intratraqueally with 25 µl of PBS or bleomycin at 2.5 mg/kg of weight body. After 7, 10 and 15 days mice were sacrificed and an exploratory x-gal staining in whole-mount lungs were performed. As is observed in Figure 13, after 15 days post treatment (p.t) with bleomycin, lungs showed intense blue staining signal which corresponded with high SAβ-Gal activity. Bearing in mind these results, we selected 15 days as p.t time before the treatment with **GOS-MSN**.

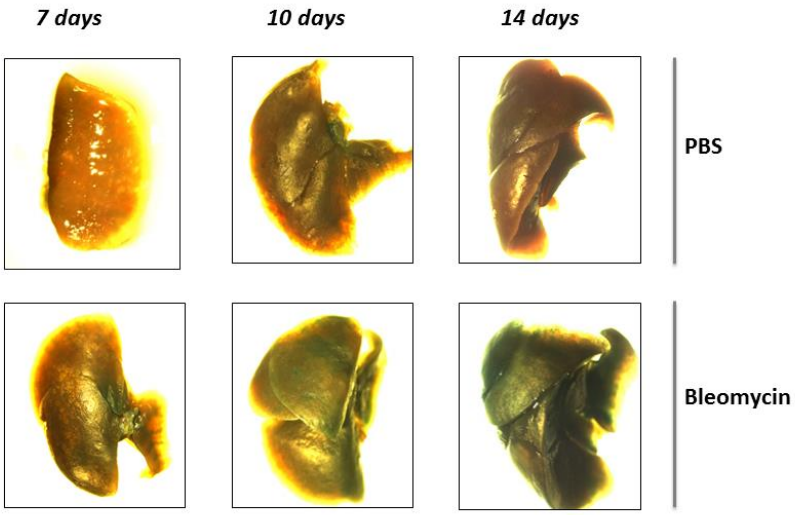

Figure 13. Staining of senescent cells (blue) with x-gal kit of lungs of control mice (treated with PBS) and lungs of fibrotic mice (treated with bleomycin) after 7, 10 and 15 days post treatment.

[10] D. M. Walters, S. R. Kleeberger, in *Current Protocols in Pharmacology*, John Wiley & Sons, Inc., 2001.

[11] K. Aoshiba, T. Tsuji, S. Kameyama, M. Itoh, S. Semba, K. Yamaguchi, H. Nakamura, *Experimental and Toxicologic Pathology*, **65**, 1053-1062.

4.4.3.1 *Biodistribution of GOS-MSN in control mice*

In order to obtain detailed knowledge about the biodistribution and *in vivo* behavior of **GOS-MSN** drug delivery system, biodistribution studies at different p.t times were performed in control mice. For these studies, each group of mice was injected *via* tail vein with 5 mg/mL of **GOS-MSN** suspension. Additionally, one group was injected with PBS in order to have a negative control. Then, mice were sacrificed at 3h, 6h, 24h, and 48h post injection (p.i), and brain, heart, lungs, esophagus, stomach, pancreas, spleen, small and large intestines, liver, kidney, bladder, muscle, serum, blood cells, skin, fat, thymus, bone and tail were extracted for Si detection. The tissues were weighed and digested. The Si concentrations in sample solutions were determined by inductively coupled plasma-atomic emission spectrometry (ICP-AES) and expressed as µg/g fresh tissue. The Si content in each organ after 3h p.i is presented in Figure 14. As can be observed, the amount of Si increased dramatically in highly perfused organs, such as lungs, liver and spleen, which could be accounted for as the combined activity of the circulating blood passing through organs, as well as that due to particle uptake by cells of the reticuloendothelial system (RES) recruited by these organs.

In Figure 15, the Si contents in lungs, spleen, liver and bladder at different p.i times is presented. Special attention was taken in the accumulation of **GOS-MSN** in lungs. At 24h after the intravenous administration of capped nanoparticles, a high decrease of Si content in lungs was observed, indicating that **GOS-MSN**s could be cleared from lungs. Taking into account these results, we chose to examine and sacrifice control and bleomycin treated mice after 6h p.i with **GOS-MSN**.

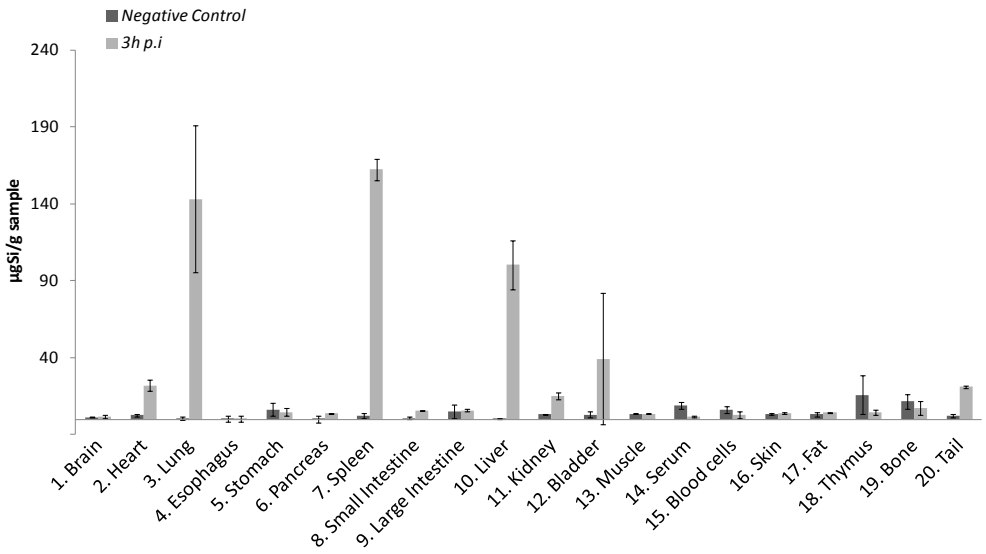

Figure 14. Biodistributions of Si in different tissues of mice after 3h p.i determined by ICP-AES. The mice were i.v injected with **GOS-MSN**. The contents of Si were expressed as µg/g fresh tissue. Values represent means ±SD.

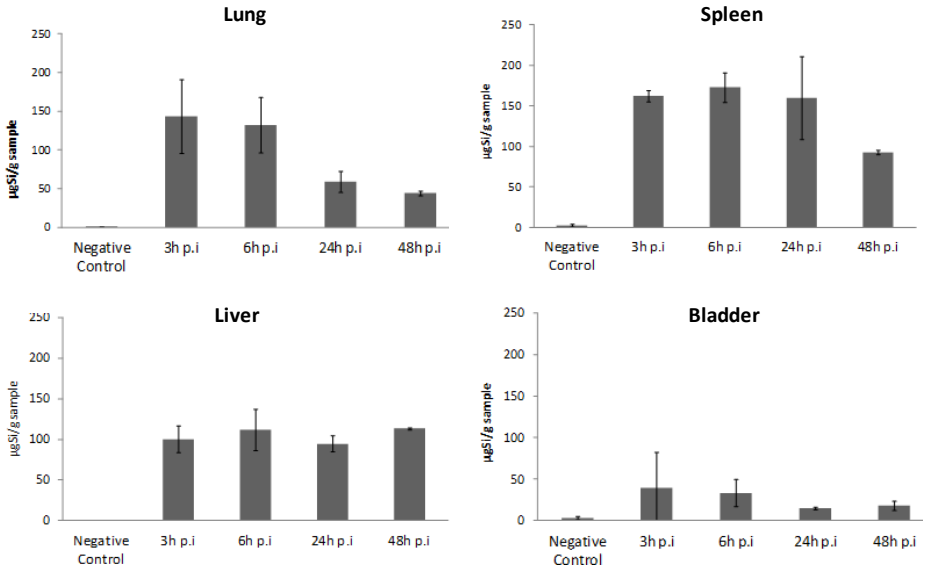

Figure 15: Biodistributions of Si in lungs, spleen, liver and bladder after different p.i times determined by ICP-AES. The contents of Si were expressed as µg/g fresh tissue. Values represent means ±SD.

4.4.3.2 *Ex vivo studies*

The targeted delivery efficacy of **GOS-MSN** (and **Glu-MSN** as control) was evaluated in the mouse model of bleomycin-induced pulmonary fibrosis. In first experiments, *ex vivo* incubation of control and fibrotic lungs with rhodamine B loaded nanoparticles were carried out. Mice were treated by direct intratracheal installation with 25 µl of PBS or bleomycin at 2.5 mg/kg of weight body. After 15 days p.t, mice were sacrificed by cervical dislocation and lungs were extracted and incubated *ex vivo* with **GOS-MSN** or **Glu-MSN** suspensions (1mg/mL) for 4h at 37^{o}C. After that time, lungs were examined by IVIS imaging spectrum system for the rhodamine b fluorescence. Interestingly, when control (PBS) and fibrotic lungs (Bleo) were incubated with **Glu-MSN**, the fluorescence signal was homogeneous throughout all the tissue, revealing a non-specific release of the entrapped dye (Figure 16-b). However, in the case of fibrotic lungs treated with **GOS-MSN**, only some areas of lungs presented fluorescence signal, whereas the control lungs showed very low fluorescence (Figure 16-b).

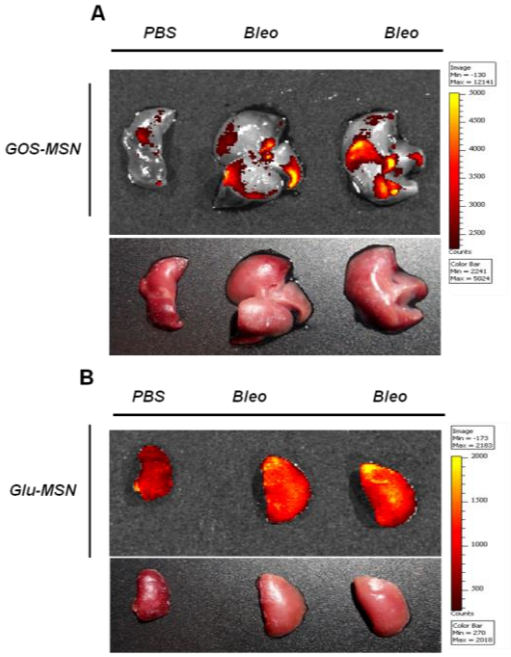

Figure 16. Lungs incubated ex vivo for 4h at 37^{o}C, with 1 mg/mL of **GOS-MSN** (A) and **GLU-MSN** (B) loaded with rhodamine b. Fluorescence detection by IVIS imaging spectrum system.

4.4.3.3 *In vivo administration of capped nanoparticles to control and bleomycin-treated mice*

In a second step, the feasibility of **GOS-MSN** to target specifically senescent cells associated with IPF pathogenesis *in vivo* were carried out. Hence, a group of mice were treated intratraqueally with 25 µl of PBS or bleomycin at 2.5 mg/kg of weight body in order to obtain control mice (PBS) and mice with pulmonary fibrosis (Bleo) respectively. After 15 days p.t, each group of mice was injected *via* tail vein with 4 mg/mL of **GOS-MSN** suspension. Moreover, as a control, other groups of animals (PBS and Bleo) were treated with **Glu-MSN**. After 6h p.i, mice were subjected to IVIS imaging spectrum system for the detection of the rhodamine B associated fluorescence *in vivo*. Afterwards, mice were sacrificed by cervical dislocation and lungs were extracted, examined by IVIS imaging spectrum system, and stained with x-gal reagent.

As seen in Figure 17-a, fibrotic mice treated with **GOS-MSN**, presented fluorescence signal in lungs area when subjected to *in vivo* IVIS images, in contrast to control mice. In addition, besides the visually recognizable inflammation associated with the development of fibrosis, the presence of senescent cells in fibrotic lungs were assessed through the remarkable blue x-gal staining appreciated in bleomycin treated mice (Figure 17-b).

Figure 17-c and -d shows the fluorescence of the rhodamine b dye associated to **GOS-MSN** and **Glu-MSN** respectively. As can be seen, in the case of treatment with **GOS-MSN**, a high intensity of fluorescence was observed in the fibrotic lungs (Bleo), whereas in the lungs of control animals a low signal was appreciated. On the other hand, the fibrotic mice presented a poor fluorescence in their livers, whereas the healthy animals (PBS) shown a high signal in livers. Similar results were obtained in three independent assays carried out in the same conditions. These results suggest that **GOS-MSN** tend to accumulate and release their payload to a greater extent in fibrotic lungs. In the case of **Glu-MSN** the fluorescence signal was found in both controls and fibrotic animals independently. Although histopathological tests shall be made in detail, these results suggest that

the preferential cargo release of GOS capped nanoparticles in mice with pulmonary fibrosis can be associated with the increased alveolar senescence.

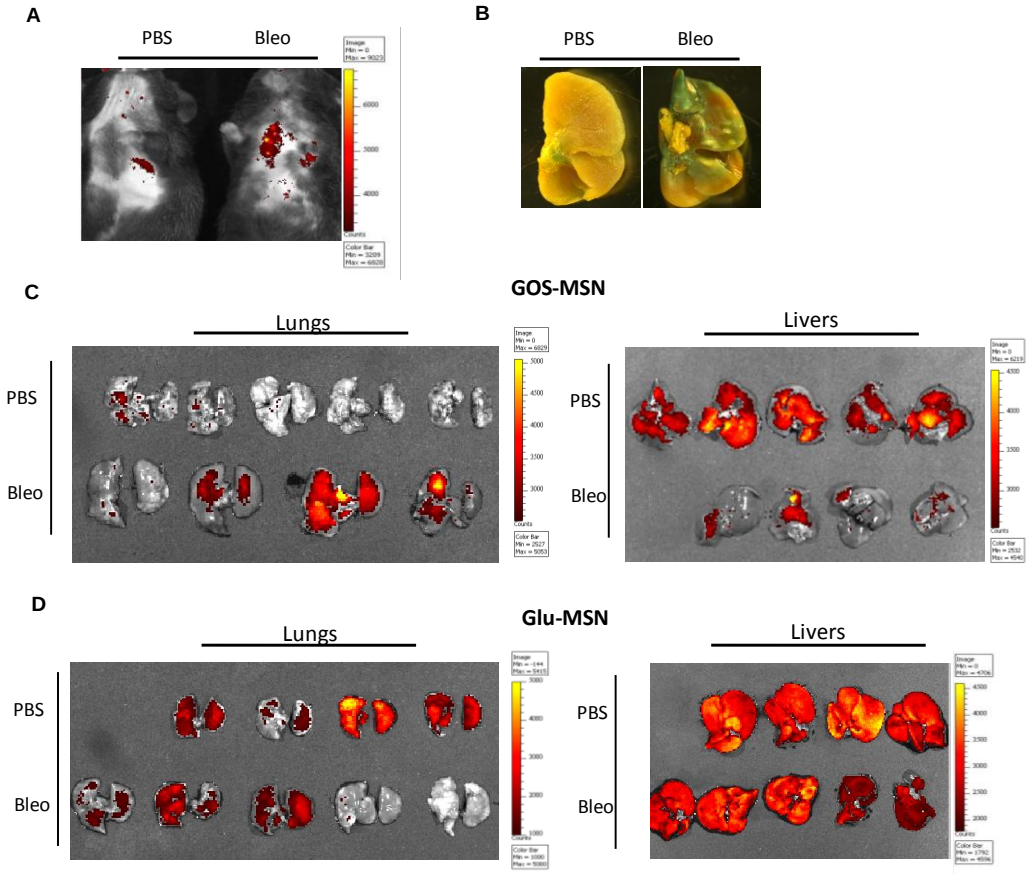

Figure 17. Mice were injected with 4 mg/mL of **GOS-MSN** loaded with rhodamine and subjected to *in vivo* IVIS imaging spectrum system for the detection of rhodamine b (A). X-gal staining of control (PBS) and fibrotic lungs (Bleo) to monitor the SAβ-gal activity (B). Removed lungs and livers from PBS- and bleomycin-treated mice injected with **GOS-MSN** and **Glu-MSN**, (C) and (D) respectively, were subjected to IVIS imaging spectrum system detection of rhodamine B.

4.5 Conclusions

In summary, we report herein the use of β-gal-responsive hybrid material (**GOS-MSN**) as a nanodelivery system for targeting senescence associated with IPF pathology. More specifically, MSN loaded with the dye rhodamine B and capped with a galactoligosaccharide (**GOS-MSN**) was prepared, the material was characterized and its performance in the presence of the enzyme β-Gal was assessed by kinetics release studies. In addition, in order to perform control experiments, mesoporous silica nanoparticles loaded with the same dye and capped with gluco-oligosaccharides derivatives were also prepared (**Glu-MSN**). The intracellular cargo release of **GOS-MSN** and **Glu-MSN** in a senescent cellular model was tested. The assays confirmed the preferentially uptake and aperture of **GOS-MSN** system in senescent cells compared with no senescent cells. In contrast, **Glu-MSN** presented the same internalization in senescent and control cells. Finally, the preferential cargo release of **GOS-MSN** hybrid material in lungs of mice with pulmonary fibrosis was confirmed. This behavior was not shown in **Glu-MSN** material, which was accumulated in lungs of control and fibrotic mice indifferently. These results are the spearhead for the validation of **GOS-MSN** system as targeted delivery nanodevice for senescent cells *in vivo*. Reported results are part of a project that aims to develop and validate a new set of nanomaterials which, by detection/removal/reprogamming of senescent cells might open up new avenues for developing innovative therapeutic applications to diagnose/treat IPF and other senescence related diseases.

4.6 Experimental Section

4.6.1 Chemicals

The chemicals tetraethylorthosilicate (TEOS), *n*-cetyltrimethylammonium bromide (CTAB), sodium hydroxide (NaOH), rhodamine B, 3-aminopropyltriethoxysilane, pancreatin from porcine pancreas and β-galactosidase from *Kluyveromyces lactis* were provided by Aldrich. Analytical-grade solvents were from Scharlab. The

hydrolysed starch Glucidex 47 (5% glucose, 50% maltose, 45% oligosaccharides and polysaccharides) was provided by Roquette. The hydrolyzed galactooligosaccharide PROMOVITA (GOS) (GOS contains at least 60% of galactooligosaccharides; 33% disaccharides, 39% trisaccharides, 18% tetrasaccharides, 7% pentasaccharides and 3% of higher saccharides) was provided by Zeus Química.

Dulbecco's Modified Eagle Medium 1X without phenol red (DMEM), fetal bovine serum (FBS), trypsin-EDTA 0.05% (1X) and the Antibiotic-Antimycotic 100X (A/A) were purchased from Gibco Life Technologies. Dulbecco's phosphate buffered saline modified (PBS), crystal violet, 4-hydroxytamoxifen (4OHT), 4',6-diamidino-2-phenylindole (DAPI), paraformaldehyde (PFA), acetic acid, Trypan Blue, Bleomycin sulfate from *Streptomyces verticillus,* tetramethylammonium hydroxide solution 25% in H_2O (TMHA) and silicon standard for ICP (1000 mg/L Si in NaOH) were provided from Sigma-Aldrich. The Senescence β-galactosidase staining kit was purchased from CellSignalling.

4.6.2 General characterization techniques

Powder XRD, TG analysis, elemental analysis, transmission electron microscopy, N_2 adsorption-desorption and UV-visible spectroscopy techniques were used to characterize the prepared materials. X-ray measurements were performed on a Bruker AXS D8 Advance diffractometer using Cu-K_α radiation. Thermo-gravimetric analyses were carried out on a TGA/SDTA 851e Mettler Toledo equipment, using an oxidant atmosphere (Air, 80 mL/min) with a heating program consisting on a heating rate of 10 °C per minute from 393 K to 1273 K and an isothermal heating step at this temperature during 30 minutes. TEM images were taken with a Philips CM10 microscope working at 100 kV. N_2 adsorption-desorption isotherms were recorded on a Micromeritics ASAP2010 automated sorption analyser. The samples were degassed at 120 °C under vacuum overnight. The specific surface areas were calculated from the adsorption data in the low pressures range using the BET model. Pore size was determined by following the BJH method. UV-visible

spectroscopy was carried out with a Lambda 35 UV/vis spectrometer (Perkin-Elmer Instruments).

4.6.3 Synthesis of the materials

4.6.3.1 *Synthesis of Mesoporous MCM-41 Nanoparticles*

The MCM-41 mesoporous nanoparticles were synthesized using the following procedure: *n*-cetyltrimethylammoniumbromide (CTAB, 2.00 g, 5.48 mmol) was first dissolved in 960 mL of deionized water. NaOH (aq) (2.00 M, 7.00 mL) was added to the CTAB solution, followed by adjusting the solution temperature to 95 °C. TEOS (10.00 mL, 5.14·10-2 mol) was then added dropwise to the surfactant solution. The mixture was allowed to stir for 2.5 h to give a white precipitate. The solid product was centrifuged and washed with deionized water till neutral pH and dried at 60 °C for 12 h (MCM-41 as-synthesized). To prepare the final porous material (MCM-41), the as-synthesized solid was calcined at 550 °C using an oxidant atmosphere for 5 h in order to remove the template phase.

4.6.3.2 *Synthesis of the galactooligosaccharide derivative GOS-d*

The galactooligosaccharide derivative was synthetized and characterized as previously reported.5. Briefly, hydrolyzed galactooligosaccharide was provided as syrup with a pH 3.8. This syrup was diluted in water and the pH was increased with $NaHCO_3$ up to 7. Then, the solution was lyophilized giving a white solid. Afterwards, 5 g of this solid were dissolved in ethanol (total volume 100 mL) and a solution of 3-aminopropyltriethoxysilane (5.85 mL, 25 mmol) was added. The reaction mixture was stirred for 24 h at room temperature. Then, the reaction was maintained at 40 ^{o}C for 1h. Finally, the solvent was evaporated under reduced pressure to give a white solid.

4.6.3.3 *Synthesis of GOS-MSN*

In a typical synthesis, 300 mg of templated-free MCM-41 and the dye rhodamine B (114.96 mg, 0.24 mmol) were suspended in 24 mL of ethanol in a round-

bottomed flask under inert atmosphere. The mixture was stirred for 24 h at room temperature with the aim of achieving the maximum loading in the pores of the MCM-41 scaffolding. Then, an excess of GOS-d (600 mg in 20 mL of ethanol) were added and the final mixture was stirred for 5.5 h at room temperature. Finally, the solid **GOS-MSN** was filtered off and washed with water to remove the externally adsorbed dye.

4.6.3.4 *Synthesis of the glucotooligosaccharide derivative (Glu-d)*

The glucooligosaccharide derivative was synthetized and characterized as previously reported.9 The hydrolysed starch Glucidex 47 (5.4 g) was previously maintained 1h at vacuum in a round bottomed flask in order to remove the adsorbed water. Afterward, the hydrolysed starch was suspended in anhydrous ethanol (250 mL) and 3-aminopropyltriethoxysilane (5.85 mL, 25 mmol) was then added. The reaction mixture was stirred in an inert atmosphere for 24 h at room temperature and then heated at 60 °C for 30 min. The solvent was evaporated under reduced pressure to give a white solid (Glu-d).

4.6.3.5 *Synthesis of Glu-MSN*

To synthetize **Glu-MSN** material, 300 mg of template-free MCM-41 and the dye rhodamine B (114.96 mg, 0.24 mmol) were suspended in 24 mL of water in a round-bottomed flask. The mixture was stirred for 24 h at room temperature. Then, an excess of the functionalized hydrolysed starch derivative (Glu-d, 300 mg) was added and the mixture was stirred for 5.5 h at room temperature. Finally, the solid **Glu-MSN** was isolated by centrifugation, washed with abundant water, and dried at 37 ^{o}C for 12 h.

4.6.4 Delivery studies

4.6.4.1 ***GOS-MSN** release experiments*

In a typical experiment, 10 mg of **GOS-MSN** were suspended in 18.75 mL of water at pH 7.5 and then 6.25 mL of enzyme β-galactosidase solution (0.3 g of enzyme in

10 mL of water at pH 7.5) was added. In parallel, 10 mg of **GOS-MSN** were suspended in 25 mL of water at pH 7.5. Both suspensions were maintained in stirring and, after a fixed time, 0.3 mL of the suspension were filtered off using 0.45 μm PTFE filters. The delivered of the dye from the pore voids to the aqueous solution was monitorized via the emission band of the dye centred at 580 nm (λ_{exc} = 555 nm). A similar experiment using **GOPS-MSN** but in the absence of β-galactosidase was also carried out. Duplicate measurements were performed. Three independent assays were carried out.

4.6.4.2 ***Glu-MSN*** *release experiments*

Following a similar procedure, 10 mg of **Glu-MSN** were suspended in 18.75 mL of water at pH 7.5 and then 6.25 mL of pancreatine enzyme solution (0.4 g in 100 mL of water at pH 7.5) was added. The suspension was stirred and, after a fixed time, 0.3 mL of the suspension were filtered off using 0.45 μm PTFE filters. Rhodamine B delivery was monitored through their emission band centred at 580 nm (λ_{exc} = 555 nm). A similar experiment using **Glu-MSN** but in the absence of pancreatin was also carried out. Duplicate measurements were performed. Three independent assays were carried out.

4.6.5 Cellular studies

4.6.5.1 *Cell culture conditions*

The ITM cell line was provided by Dr. Manuel Serrano from Spanish National Cancer Research Centre (CNIO). This cell line is derived from human primary pulmonary fibroblasts (IMR-90) and immortalized by the expression of the catalytic subunit of telomerase hTERT. In order to obtain the cellular model of senescence, IMR-90 cells were retrovirally transduced with a fusion of the oncogene MEK1 and a modified hormone-binding domain of the oestrogen receptor, obtaining the ITM cell line. ITM cells were routinely grown in DMEM (without phenol red) supplemented with 10% FBS and 1% of A/A, at 37 ^{0}C in an atmosphere of 5% CO_2 and underwent passage three times a week.

4.6.5.2 *Senescence induction in ITM cells and x-gal staining*

Cells were cultured in sterile 6–well microtiter plates at a seeding density of 60 x 10^3 cells/well with DMEM (without phenol red, 10% FBS and 1% of A/A) and were allowed to settle for 24h. After that time, the medium was replaced for DMEM (without phenol red, 0.5% FBS and 1% of A/A) and cells were treated with a solution of 4OHT in ethanol at a final concentration of 100 nM. Cells maintained as a control were treated with the same volume of ethanol instead 4OHT. After 72 h of treatment, cells were fixed and stained with the senescence β-galactosidase staining kit**.** The followed staining procedure was the described in the commercial kit. Briefly, 1mL of the x-gal staining reagent (kit) was added to each well, and the plate was incubated at 37 ^{0}C in an atmosphere of 5% CO_2 overnight.

4.6.5.3 *Fluorescence microscopy assays*

ITM cells were seeded in 24 mm glass coverslips in 6-well microliter plates at a seeding density of 60 x 10^3 cells/well. After 24 hours, cells were treated with 4OHT or vehicle as described above. After 48h of treatment, the corresponding capped nanoparticles (**GOS-MSN** or **Glu-MSN**) were added to each well at a final concentration of 50 μg/mL and cells were further incubated for 24h. After that time, the medium was removed and washed with PBS, cells were fixed with PFA (4%) and stained with x-gal reagent overnight. Finally, cells were visualized under a fluorescence microscopy (Nikon Eclipse E600, with Nikon DigitalSight DS-Ri1 camera and epifluorescence system, contrast system inter-differential (DIC) and dark field). Identical experiments were done three times.

4.6.5.4 *Confocal microscopy assays*

Cells were seeded in 12 mm glass coverslips in sterile 24–well microtiter plates at a seeding density of 40 x 10^3 cells/well in the case of control cells, and at a seeding density of 150 x 10^3 cells/well in the case of cells addressed to be treated with 4OHT. Cells were allowed to settle for 48h and treated with ethanol (controls) or 4OHT as previously described. After 72h of incubation, the corresponding capped nanoparticles (**GOS-MSN** or **Glu-MSN**) were added to each well at a final

concentration of 50 μg/mL and cells were further incubated for 6h. Finally, cells were washed, fixed with PFA and stained with DAPI for nuclear staining. Cells were visualized under confocal microscopy using a Zeiss LSM 780 multiphoton on an Axio Observer.Z1 invert with 7 laser lines including 405, 458, 488, 514, 561, 594 and 633 nm. Duplicate measurements were performed. Three independent assays were carried out. Data are expressed as (mean ± SE). Images were processed using ImageJ.

4.6.6 In vivo studies

4.6.6.1 *Mice*

Wild-type (WT) mice were housed at the serum pathogen-free (SPF) barrier area of the Spanish National Cancer Research Center, Madrid. Mice were observed on a daily basis and sacrificed in accordance to the Guidelines for Human Endpoints for Animals Used in Biomedical Research from the Council for International Organizations of Medical Sciences (CIOMS). All animal procedures were performed according to protocols approved by the CNIO-ISCIII Ethics Committee for Research and Animal Welfare (CEIyBA).

4.6.6.2 *Induction of pulmonary fibrosis in wild type mice*

Bleomycin solution was prepared in PBS at 2 mg/mL. Bleomycin was delivered with a catheter at dose of 2.5 mg/kg, by intratracheal instillation under light medetomidine/ketamine anesthesia (Day 0). Then, the animals were treated with antisedan solution *i.v* and maintained in the serum pathogen-free (SPF) barrier area.

4.6.6.3 *X-gal staining assays*

X-gal staining was performed in lungs using the senescence β-galactosidase staining kit. Briefly, whole-mount lungs were fixed at room temperature for 45 min with a solution containing 2% formaldehyde and 0.2% glutaraldehyde in PBS,

washed three times with PBS, and incubated overnight at 37 ^{0}C with the staining solution containing x-gal in *N,N*-dimethylformamide (pH 6.0) in stirring.

4.6.6.4 *Biodistribution assays*

WT mice were treated with a suspension of **GOS-MSN** (5 mg/mL) in PBS with 5% BSA via tail vein injection at a final dose of 50 mg/Kg. Then mice were sacrificed at 3, 6, 24 and 48 h p.i (*n* = 2). Additionally, a group of WT mice without treatment was taken as negative control. The brain, heart, lungs, esophagus, stomach, pancreas, spleen, small and large intestines, liver, kidney, bladder, muscle , serum, blood cells, skin, fat, thymus, bone and tail were extracted and kept frozen for Si detection. Tissues were weighed and digested with 2 mL of TMHA (25%)[12] in closed PTFE vessel for 2h at 80^{0}C in the digestion unit Bloc digest 20 (Selecta). After cooling, digests were diluted to 10 mL in polypropylene erlenmeyer flasks to avoid Si contamination and kept in polystyrene tubes. Standard solutions were prepared from silicon standard for ICP and were digested and treated exactly the same way as the samples (5% TMHA). All results were calculated using the calibration with digested standard solutions. The Si concentrations in sample solutions were determined with the ICP-OES system Agilent 5100 and expressed as µg/g fresh tissue. Si-measurements were performed simultaneously on two different wavelengths 251.611 nm and 288.158 nm and all data presented here were obtained on the emission line at 251.611 nm. Data are expressed as (mean ± SE).

4.6.6.5 *In vivo treatment of mice with pulmonary fibrosis with capped nanoparticles*

WT mice were treated with PBS or bleomycin as detailed above (Day 0). 10-12 days after the treatment, mice were isoflurane anesthetized and the chest hair was removed by applying hair removal cream. 15 days p.t mice were injected via

[12] S. Hauptkorn, J. Pavel and H. Seltner, Fresenius, *J. Anal. Chem.,* **2001**, *370*, 246.

tail vein with a suspension of the corresponding nanoparticles, **GOS-MSN** or **Glu-MSN** at 4 mg/mL in DMEM (*n* = 5 per group). After 6h, mice were observed *in vivo* by IVIS *In Vivo* Imaging System (PerkinElmer). Then, mice were sacrificed by cervical dislocation and lungs and livers were removed and examined again by IVIS.

5. Advanced communication processes between nanodevices through the interchange of chemical messengers

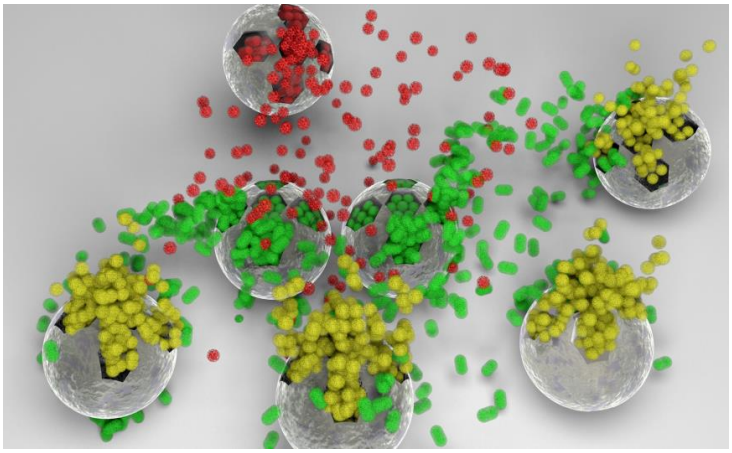

This chapter is derived from the adaptation of the following manuscript:

*Angew. Chem. Int. Ed., **2014**, 53, 12629*

Reprinted with permission from Wiley

5.1 **Introduction**

Human beings primarily communicate through sound and sight. Voice, looks and body language are the major means of active and direct communication. In today's rapidly accelerating age of information technology, digitized renditions of these primary tools of information sharing are becoming more and more popular. However, there is a more basic world of communication that largely escapes this progress, i.e., chemical communication. For the vast majority of creatures on earth, this way of communication is even the most important one.[1] It is presumably the oldest and most wide-spread form of communication.[2] Bacteria,[3] plankton,[4] insects,[5] vertebrates,[6] and plants use it[7] yet it also occurs between different forms of life such as bacteria and hosts in general[8] or certain plants and microbes in particular.[9]

Chemical communication—in the sense of the Latin *communicare* that means to share or exchange information—in man-made systems on the other hand is practically non-existent. There are no relevant applications of anthropogenic origin in which chemical analogues to pheromones, kairomones or other allelochemicals play a major role and connect the active states of two systems. In this context, the classic case of man-made systems responding to chemical stimuli is related to recognition. Such recognition itself can further be associated with a change of a physico-chemical property, resulting for instance in a signal that is

[1] W. C. Agosta, *Chem. Comm.*, Scientific American Library, New York, **1992**.

[2] S. Steiger, T. Schmitt, H. M. Schaefer, *Proc. R. Soc.* **2011**, *278*, 970.

[3] C. M. Waters, B. L. Bassler, *Annu. Rev. Cell Dev. Biol.* **2005**, *21*, 319.

[4] E. Van Donk, *Ecol. Inform.* **2007**, *2*, 112.

[5] G. E. Robinson, Z. Y. Huang, *Apidologie* **1998**, *29*, 159.

[6] A. Sbarbati, F. Osculati, *Cells Tissues Organs* **2006**, *183*, 206.

[7] R. Wayne, *Bot. Rev.* **1994**, *60*, 265.

[8] A. R. Pacheco, V. Sperandio, *Curr. Opin. Microbiol.* **2009**, *12*, 192.

[9] D. V. Badri, T. L. Weir, D. van der Lelie, J. M. Vivanco, *Curr. Opin. Biotechnol.* **2009**, *20*, 642.

subsequently transduced by a device as in a sensor[10] or in the delivery of compounds such as in drug delivery systems.[11] In all of these cases, the receiver is reacting on the stimulus, but there is no sharing of information with other receivers in an information chain. Although several papers deal with chemical reaction networks and interacting synthetic molecules,[12] communication by an exchange of various chemicals as messengers between different systems such as for instance nanoscopic chemical objects has not been realized yet. The advantages of such systems however are immediately obvious; they constitute the basis of a dynamically interacting network eventually resulting in certain autonomy of the system. Consider an ensemble of different types of particles, each being loaded with a certain chemical and containing a specific recognition element that controls the release of the payload. Consider further that some of the payload chemicals can serve as "keys" to control the release of the cargo of a third type of particle. Theoretically, an almost limitless number of particle types can be envisioned that can indeed communicate with another in a designed fashion through their chemical messengers. Depending on the arrangement and device integration of the various particles, directional communication over longer distances, hierarchical communication within a larger population of such systems and more complex cause-and-effect systems can be envisioned.

To rationalize the concept of "communicating nanoparticles", let our particles mimic the perhaps simplest living organisms that communicate with each other, cells. Cells are able to perceive and respond to their environment and to their peers through the exchange of chemical information which is basically

[10] J. Janata, *Principles of Chemical Sensors*, Springer, New York, **2009**.

[11] (a) S. Rieth, K. Hermann, B.-Y. Wang, J. D. Badjić, *Chem. Soc. Rev.* **2011**, *40*, 1609. (b) O. Kreft, M. Prevot, H. Möhwald, G. B. Sukhorukov, *Angew. Chem. Int. Ed.* **2007**, *46*, 5605. (c) C. Coll, A. Bernardos, R. Martínez-Máñez, F. Sancenon, *Acc. Chem. Res*. **2013**, *46*, 339. (d) P. Yang, S. Gai, J. Lin, *Chem. Soc. Rev*. **2012**, *41*, 3679. (e) Z. Li, J. C. Barnes, A. Bosoy, J. F. Stoddart, J. I. Zink, *Chem. Soc. Rev*. **2010**, *41*, 2590.

[12] (a) R. F. Ludlow, S. Otto, *Chem. Soc. Rev.* **2008**, *37*, 101. (b) A. F. Taylor, M. R. Tinsley, F. Wang, Z. Huang, K. Showalter, *Science* **2009**, *323*, 614.

accomplished by cellular receptors located on the cell's surface, often in close proximity to or direct feedback with transport structures in the cell membrane.[3,13] Cells can also communicate in a multi-cellular organism, a widely known prototype being neurons. Neurons share or process information and use neurotransmitters such as glutamate or GABA (γ-aminobutyric acid) to bridge the synaptic region and propagate information.[14]

For the realization of the communicating nanoparticles concept we relied on gated mesoporous hybrid nanoparticles. Taking into account the design versatility, these systems allow the construction of an ensemble of different types of nanodevices, each being loaded with a certain chemical and externally functionalized with a gate-like entity that controls the release of the payload. An accurate selection of the gated solids and the messengers is crucial for the achievement of this chemical communication cascade. In this novel and unique approach the system will produce a macroscopic response which is related to the information which different nanoparticles have shared via chemical substances; the messengers. Taking into account our interest in the design of bio-inspired nanodevices and believing that the development of communication protocols between chemical systems may find applications in a number of fields, we have attempted herein to demonstrate that it is possible to design nanoparticles that can communicate to each other.

5.2 **Objectives**

Bearing in mind the idea of hierarchical information sharing between different species, the aim of this chapter was to design different types of specifically

[13] a) J. S. Dickschat, *Nat. Prod. Rep.* **2010**, *27*, 343-369. b) A. Kerenyi, D. Bihary, V. Venturi, S. Pongor, *PLoS One* **2013**, *8*, e57947.

[14] K. M. Betke, C. A. Wells, H. E. Hamm, *Progr. Neurobiol.* **2012**, *96*, 304.

functionalized nanoparticles able to communicate with each other through the exchange of chemical information. Specifically our objectives were:

- ✓ Design and preparation of three gated nanodevices where the chemical messenger delivered by the first type of gated nanoparticle upon an external stimulus will open the second type of nanoparticle which delivers another messenger that opens the third group of gated system.
- ✓ Characterization of the synthetized solids
- ✓ Evaluation of the communication networks between particles

5.3 **Synthesis and Characterization**

5.3.1 Design of the system

In this work three types of gated mesoporous hybrid nanoparticles have been designed. The crucial task for achieving such "chemical communication" is the careful selection of the gated hybrids and the messengers. The selected capped nanodevices are described below:

- ✓ The first gated solid (**S1**) in the communication chain is an enzyme-triggered MSN loaded with the first messenger **M1**, the reducing agent tris(2-carboxyethyl)phosphine (TCEP, red balls in Figure 1). The pores of **S1** are capped with a saccharide derivative (Glucidex).
- ✓ The second MSN (**S2**) is capped with polyethylene glycol (PEG) chains attached through disulfide linkages to the silica surface and contains the second messenger dodecyltrimethylammonium bromide (DTAB, **M2,** green cylinders in Figure 1) as cargo.
- ✓ The third system (**S3**) hosts a capping lipid bilayer (prepared from 1,2-dioleoyl-sn-glycero-3-phosphocholine, DOPC) and is loaded with a dye (safranin O, yellow balls in Figure 1).

The communication sequence is as follows (cf. Figure 1a). In the presence of a specific enzyme (pancreatin) in an aqueous suspension containing **S1**, **S2** and **S3**, the hydrolysis of the grafted polysaccharide in **S1** is induced with the subsequent delivery of **M1**. In the second step, **M1** would trigger the delivery of **M2** from **S2** by rupture of the redox-labile disulfide bonds. Finally, **M2** molecules would disrupt the lipid bilayer around **S3**, leading to the delivery of the entrapped dye safranin O.

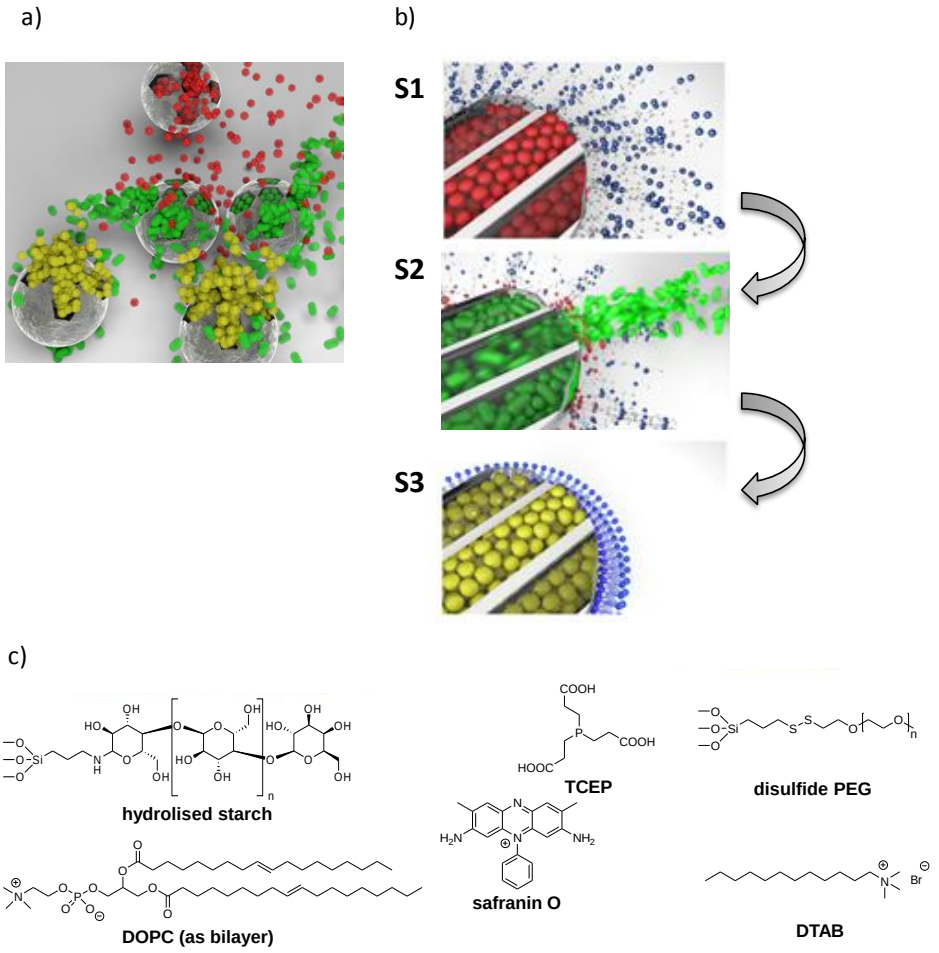

Figure 1. Illustration of global system design: red cargo released from first type of particle opens pores of second type of particles, which release green cargo to open pores of third type of particle;

for sake of clearness only a limited number of particles is displayed and gating chemistries have been omitted. b) Close-up to illustrate design of single systems: Left, **S1** in capped mode with TCEP cargo (red) and starch capping layer; middle, **S2** in single-pore release mode with DTAB cargo (green) and PEG capping layer; right, **S3** in capped mode with safranin O cargo and DOCP capping bilayer. c) Gating chemistries in detail.

In addition, the unequivocal discrimination between individual and collective behaviour of **S1**, **S2** and **S3** is only possible with appropriate reference systems. For this purpose, the gated hybrids $\mathbf{S1_{dye}}$, $\mathbf{S2_{dye}}$, $\mathbf{S1_{blank}}$ and $\mathbf{S2_{blank}}$ were also prepared and investigated. $\mathbf{S1_{dye}}$ and $\mathbf{S2_{dye}}$ are equipped with the same capping system as **S1** and **S2** yet contain a dye as cargo which renders the assessment of their capping/uncapping performance more facile through conventional fluorometric techniques. In particular, $\mathbf{S1_{dye}}$ incorporates rhodamine B and $\mathbf{S2_{dye}}$ safranin O. Moreover, to demonstrate the crucial role played by the messengers in the chemical communication, $\mathbf{S1_{blank}}$ and $\mathbf{S2_{blank}}$ were synthesized, both containing the same gating chemistry on the outer surface as **S1** and **S2** yet lacking the cargo inside the pore voids.

5.3.2 Synthesis of the materials

In order to obtain these gated nanodevices, silica mesoporous (MCM-41-type) nanoparticles (ca. 100 nm) were selected as inorganic scaffold. For the preparation of the final capped nanoparticles the calcined MSN were first loaded with a certain cargo and then capped with the corresponding molecular ensemble.

- **First type of Nanoparticles: S1, $\mathbf{S1_{dye}}$, $\mathbf{S1_{blank}}$**

The synthesis of the gated hybrid material was carried out through the grafting of the gate-like ensemble on the inorganic support previously loaded. Ideally, the final material should contain the **M1** inside the pores and the hydrolyzed starch derivative anchored at the entrances of the pores. For this purpose, MCM-41

mesoporous silica nanoparticles were prepared using TEOS as inorganic precursor and CTAB as structure-directing agent. Finally, the obtained as-synthesised material was calcined in order to remove the template phase. In a second step, MCM-41 nanoparticles were suspended in a solution of TCEP (**M1**) in order to achieving the maximum loading in the pores of the MCM-41 scaffolding. Then, an excess of the functionalized hydrolyzed starch derivative (Glu-d) was added, and the final mixture was stirred at room temperature. Glu-d was previously synthesized and characterized following the procedure described by our group.[15] As a final step, final nanoparticles (**S1**) were washed with abundant water in order to remove the externally adsorbed TCEP, and dried at 40 ^{o}C for 12 h.

S1$_{dye}$ and **S1$_{blank}$** materials were prepared following similar procedures. In the case of **S1$_{dye}$**, MCM-41 nanoparticles were loaded with rhodamine B dye and functionalized with Glu-d compound. Solid **S1$_{blank}$** was prepared as **S1** but MCM-41 material was not loaded with any cargo before its functionalization.

- **Second type of Nanoparticles: S2, S2$_{dye}$, S2$_{blank}$**

As in the case of **S1**, the second type of nanoparticles were prepared following grafting procedures. Calcinated MCM-41 nanoparticles were suspendend in a solution of the cargo molecule DTAB (**M2**) and the mixture was stirred, filtered off and dried under vacuum. In a second step, the loaded material were treated with (3-mercaptopropyl)trimethoxysilane in order to obtain thiol functionalized nanoparticles. Then, 2,2'-dipyridyl disulfide was added to the reaction mixture. Finally, the prepared solid was treated with O-(2-Mercaptoethyl)-O'-methyl-hexa(ethylene glycol) in the presence of an excess of DTAB. The mixture was stirred and the final solid **S2** was isolated by centrifugation, washed with abundant water and dried.

[15] A. Bernardos, L. Mondragón, E. Aznar, M. D. Marcos, R. Martínez-Máñez, F. Sancenón, J. Soto, J. M. Barat, E. Pérez-Payá, C. Guillem, P. Amorós, ACS Nano 2010, 4, 6353-6368.

The solid **S2$_{dye}$** was prepared following the same procedure described above but, in this case, the MCM-41 material was loaded with safranin O dye. In the same way, **S2$_{blank}$** was prepared such as **S2** but without loading the pores of the MCM-41 scaffolding before functionalization.

- **Third type of Nanoparticles: S3**

For the synthesis of **S3** material, template-free MCM-41 nanoparticles were suspended in a safranin O dye solution (**M3**) and the mixture was stirred in order to achieve the maximum dye loading. Afterward, a suspension of liposomes was prepared using DOPC lipid. In order to prepare the nanoparticles coated with the lipid bilayer, the liposome's suspension was added to the suspension of the MCM-41 support. Finally, the nanoparticles were isolated, washed with abundant water and dried at 40 ^{o}C for 12 h.

5.3.3 Characterization

All prepared solids were fully characterized using standard procedures. The powder X-ray diffraction (PXRD) of the as-synthesised nanoparticulated MCM-41 (see Figure 2, curve a) shows the typical low-angle reflections that can be indexed as (100), (110) and (200) Bragg peaks. From the PXRD data of the as-synthesised MCM-41, a d_{100} spacing of 40.04 Å was calculated. A significant displacement of the peaks in the PXRD of the calcined MCM-41 was found corresponding to an approximate cell contraction of 5 Å (Figure 2, curve b). This displacement and broadening are related to further condensation of silanol groups during the calcination step. Figure 2 also shows the PXRD patterns for solids **S1**, **S1$_{dye}$**, **S1$_{blank}$**, **S2**, **S2$_{dye}$**, **S2$_{blank}$** and **S3** (curves c, d, e, f, g, h and i, respectively). For these materials, the reflections (110) and (200) are much less intense, most likely due to a reduction of contrast as consequence of the pore loading and/or the functionalization process. Nevertheless, the presence of the (100) peak in the PXRD patterns in all cases indicated that the process of pore loading, and the additional functionalisation did not modify the mesoporous structure of the

MCM-41 support to a large extent. The preservation of the mesoporous structure in the MCM-41 calcined sample and in the final functionalised solids was also confirmed using transmission electron microscopy (TEM) analysis. Figure 2 also shows TEM images of the calcined MCM-41 and the final solids **S1**, **S2** and **S3**. The typical hexagonal porosity and channels of the MCM-41 matrix as alternate black and white stripes are observed in all cases.

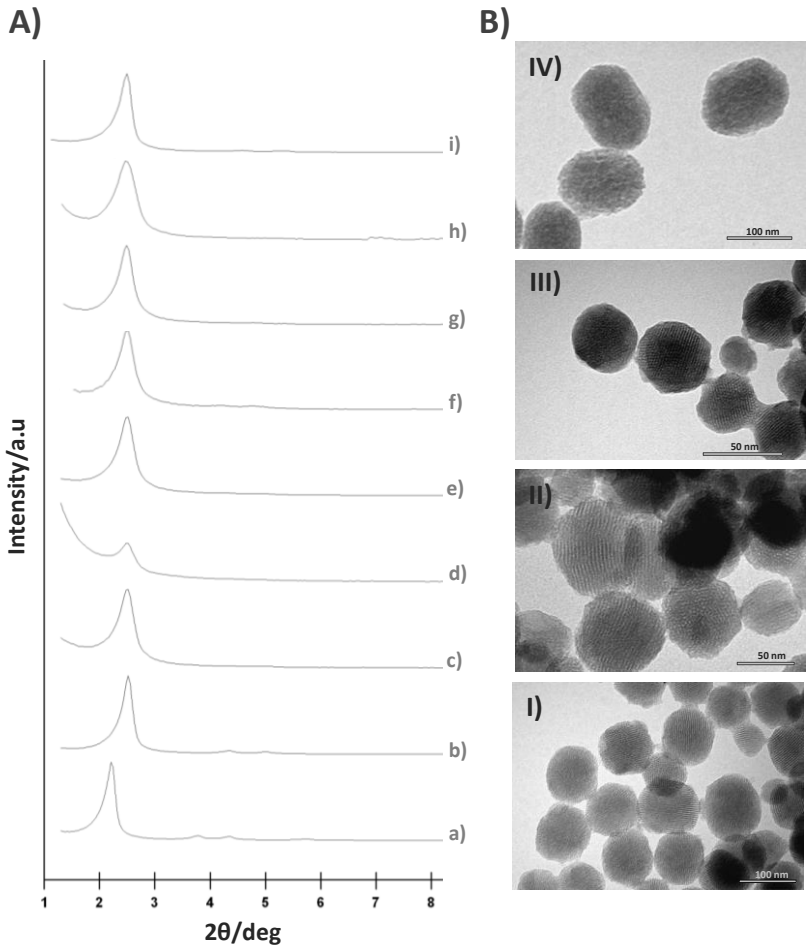

Figure 2. A) Powder X-ray patterns of the solids (a) MCM-41 as synthesised (b) calcined MCM-41, (c) solid **S1,** (d) solid **S1**$_{dye}$, (e) solid **S1**$_{blank}$, (f) solid **S2**, (g) solid **S2**$_{dye}$, (h) solid **S2dye**$_{lank}$ and (i) solid **S3**. B) TEM images of calcined MCM-41 sample (I), solid **S1** (II), solid **S2** (III) and solid **S3** (IV), showing the typical hexagonal porosity of the MCM-41 mesoporous matrix.

The N_2 adsorption-desorption isotherms of the starting calcined MSN show an adsorption step with an intermediate P/P_0 value (0.1–0.3) (see Figure 3 curve a). This curve corresponds to a type IV isotherm, in which the observed step can be related to the nitrogen condensation inside the mesopores by capillarity. The absence of a hysteresis loop in this interval and the narrow pore distribution suggests the existence of uniform cylindrical mesopores. From this curve, a pore volume of 0.81 $m^3 g^{-1}$ was calculated by the BJH model on the adsorption branch of the isotherm. The application of the BET model resulted in a value of 1034 $m^2 g^{-1}$ for the total specific surface area. Moreover, from the PXRD, porosimetry and TEM measurements the a_0 cell parameter (40.41 Å), the *pore diameter* (2.59 nm) and a value for the wall thickness of 1.45 nm can be calculated.

N_2 adsorption-desorption isotherms for **S1**, **S2** and **S3** (see Figure 3) are then in general agreement with a mesoporous systems possessing filled mesopores and a significant decrease in the N_2 volume adsorbed and surface area was observed. The same behavior was found for $\mathbf{S1_{dye}}$, $\mathbf{S1_{blank}}$, $\mathbf{S2_{dye}}$ and $\mathbf{S2_{blank}}$ (curves not shown). In fact, these solids presents relative flat curves when compared (at the same scale) to those of the MCM-41 parent material, indicating that there is a significant pore blocking. BET specific surface values, pore volumes, and pore sizes calculated from the N_2 adsorption-desorption isotherms for MCM-41, **S1**, $\mathbf{S1_{dye}}$, $\mathbf{S1_{blank}}$, **S2**, $\mathbf{S2_{dye}}$, $\mathbf{S2_{blank}}$ and **S3** are listed in Table 1.

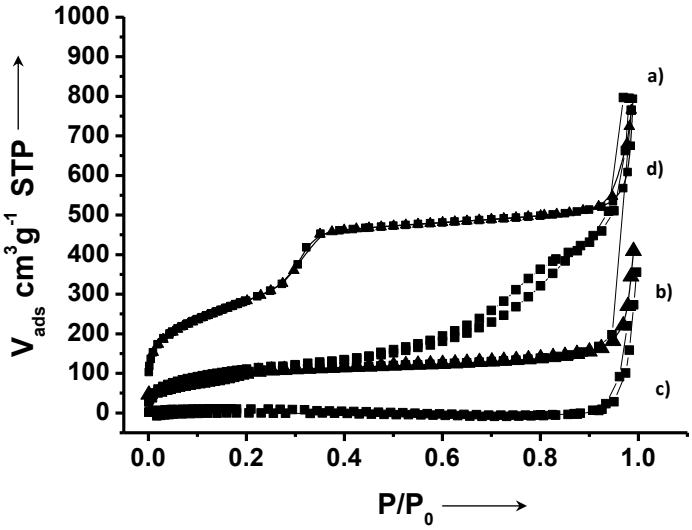

Figure 3. Adsorption-desorption isotherms for a) calcined MCM-41, b) **S1**, c) **S2** and d) **S3**.

Table 1. BET specific surface values, pore volumes and pore sizes calculated from the N_2 adsorption-desorption isotherms for selected materials.

	S_{BET} (m^2g^{-1})	BJH pore ($P/P_0 < 0.4$)[a] (nm)	Total pore volume[b] (cm^3g^{-1})
MCM-41	1034.3	0.81	2.59
S1	372.6	0.25	2.21
$S1_{dye}$	231.5	0.19	---
$S1_{blank}$	697.9	0.49	2.47
S2	247.8	0.19	2.14
$S2_{dye}$	34.82	---	---
$S2_{blank}$	476.8	0.19	2.22
S3	411.3	0.64	---

[a] Pore size estimated by using the BJH model applied on the adsorption branch of the isotherm, for $P/P_0 < 0.4$, which can be associated to the surfactant generated mesopores.

[b] Total pore volume according to the BJH model.

The thermal analyses of the prepared solids show a typical behaviour of functionalized mesoporous materials, that is, an initial weight loss between 25 and 150 ^oC related to solvent evaporation, a second loss between 150 and 800 ^oC

due to the combustion of organic material, and a final loss in the 800-1000 ^{o}C range related to the condensation of the silanol groups. The loading and the grade of functionalisation of the solids were determined by elemental analysis and thermogravimetric studies and the results are listed in Table 2.

Table 2. Content of cargo molecules and capping moieties for the prepared solids in mg g^{-1} SiO_2

	Glu-d	TCEP	RhB	PEG	DTAB	Safranin	DOPC
S1	58.8	56.7	-	-	-	-	-
$S1_{dye}$	59.3	-	44.1	-	-	-	-
$S1_{blank}$	57.9	-	-	-	-	-	-
S2	-	-	-	137.4	58.1	-	-
$S2_{dye}$	-	-	-	257.5	-	53.3	-
$S2_{blank}$	-	-	-	315.5	-	-	-
S3	-	-	-	-	-	27.1	170.8

5.4 **Results and discussion**

5.4.1 Delivery studies of the single ensembles

Before investigating the chemical interplay between the particles, the designated capping/uncapping behavior of the single ensembles was confirmed with the aid of the dye-loaded nanoparticles **$S1_{dye}$**, **$S2_{dye}$** and **S3** and fluorescence spectroscopy. In all cases, the delivery studies demonstrated that virtually no ("zero") delivery is observed in neutral aqueous solution.

- ***Delivery studies with $S1_{dye}$***

As was reported by our group, the anchoring of the starch derivative Glu-d on the pores outlets of a silica mesoporous support inhibits cargo delivery.[15]. Moreover, in presence of pancreatin (containing amylases able to hydrolyze the 1➔4 glycosidic bond between β-D-glucoses present in the starch) the hydrolysis of the

saccharide network would result in an uncapping of the pores allowing delivery of the entrapped molecule (see Figure 4). In a typical experiment, the capped **S1$_{dye}$** material was suspended in distilled water and a suspension of pancreatin was added. In addition, a similar experiment was carried out but without adding the enzyme. Rhodamine B dye delivery was monitored in both cases. From the kinetic curves presented in Figure 5, it can be seen that solid **S1$_{dye}$** was unable to release rhodamine B in the absence of pancreatin, whereas in the presence of the enzyme a remarkable delivery of the dye was found as a consequence of the enzyme-induced hydrolysis of the glycosidic bonds in the anchored starch fragments on the outer particles' surface.

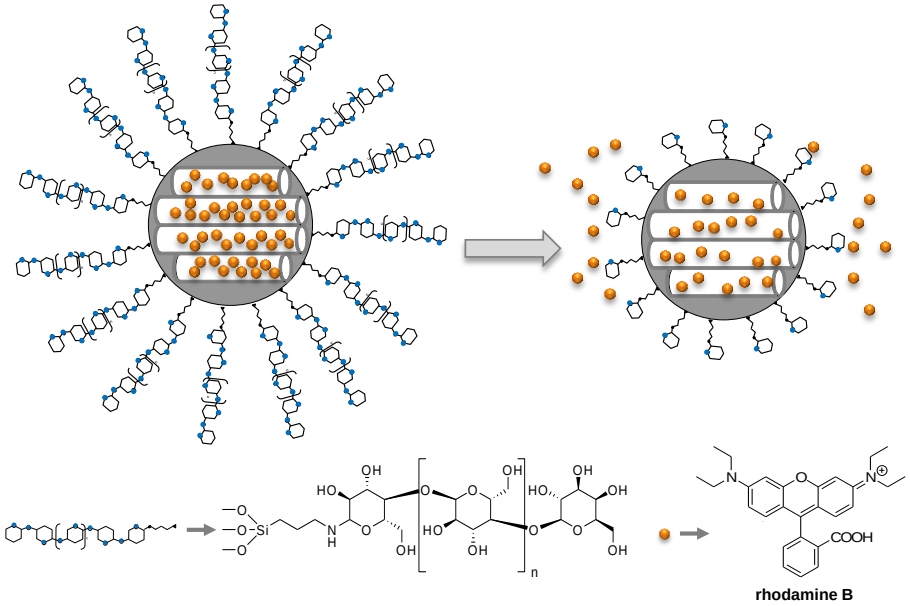

Figure 4. Representation of the gated material **S1$_{dye}$** capped with a hydrolyzed starch derivative (**Glu-d**). The delivery of the entrapped guest (rhodamine B) is selectively accomplished in the presence of pancreatin.

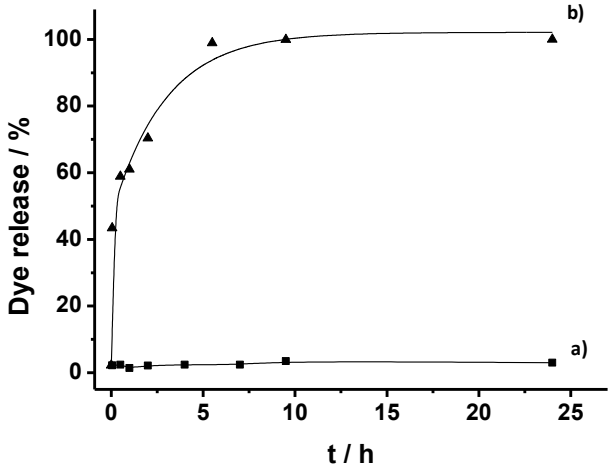

Figure 5. Release of rhodamine B dye from solid **S1**$_{dye}$ in the absence (a), and in the presence (b), of pancreatin at pH 7.5.

- **Delivery studies for S2**$_{dye}$

In the second type of designed nanoparticles, PEG chains anchored on particles surface through a disulphide bond were expected to cap the pores and inhibit cargo release. The addition of a reductive agent, that is able to reduce the disulphide linkages, would trigger the PEG chains detachment and cargo release (Figure 6). Delivery experiments were carried out using the capped material **S2**$_{dye}$, in the presence of tris(2-carboxyethyl)phosphine (TCEP) as reducing agent. To carry on this study, the material **S2**$_{dye}$ was suspended in distilled water and a TCEP solution was added. The suspension was then stirred and dye delivery was monitored through the emission band of safranin O. An identical experiment using **S2**$_{dye}$ in the absence of TCEP was also carried out.

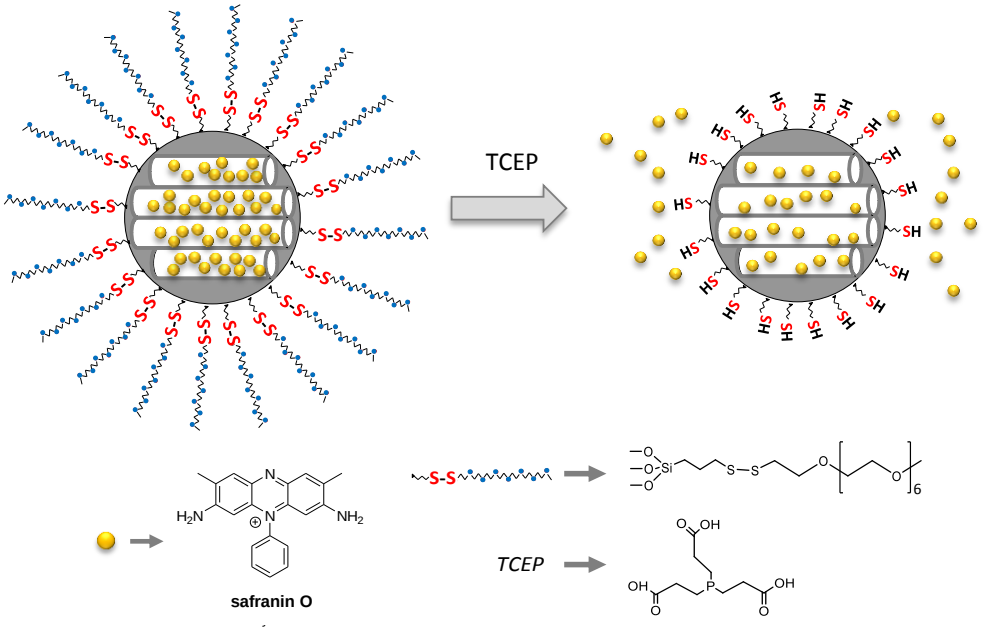

Figure 6. Representation of the gated material **S2$_{dye}$** functionalized with polyethylene glycol through a disulphide linkage. The delivery of the entrapped guest (safranin O) is triggered by the reducing agent TCEP.

As it can be seen in Figure 7, in the absence of TCEP a negligible dye release from **S2$_{dye}$** was observed, whereas upon addition of the reducing agent a remarkable release of safranin O was found because of the reduction of disulfide groups and cleaving the PEG caps.

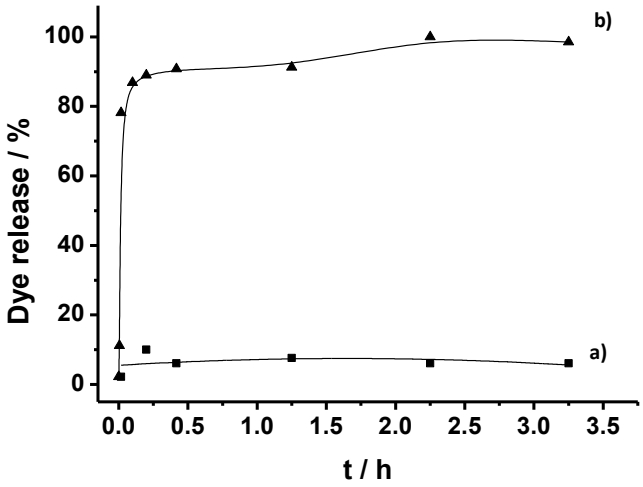

Figure 7. Release of safranine O dye from solid $\mathbf{S2_{dye}}$ in the absence (a), and in the presence (b), of TCEP 0.1 mM.

- **Delivery studies for S3**

The designed system **S3** is based on the liposome fusion on a mesoporous silica particle core.[16] The obtained mesoporous nanoparticle containing the lipid bilayer is expected to retain the entrapped cargo until a disrupting agent is added (Figure 8). The delivery of safranin O cargo from **S3** material was monitored in the presence or absence of the surfactant DTAB. As it can be seen in Figure 9, the addition of DTAB induced a massive safranin O release due to the surfactant-induced rupture of the bilayer coating. In contrast, a negligible dye release was observed in the absence of DTAB.

[16] a) J. Liu, A. Stace-Naughton, X. Jiang, C. J. Brinker, *J. Am. Chem. Soc.,* **2009**, *131*, 1354. b)J. Sun, E. Jakobsson, Y. Wang, C. J. Brinker, *Life*, **2015**, *5,* 214.

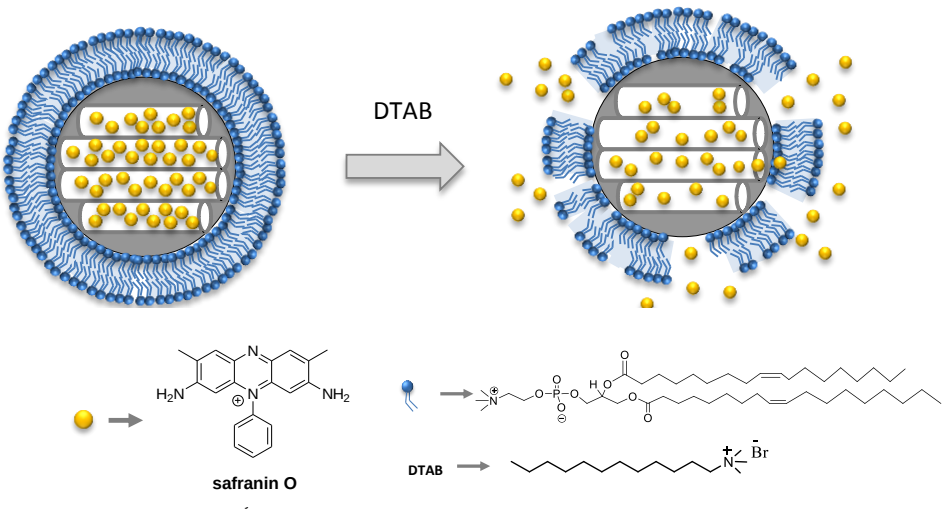

Figure 8. Representation of the material **S3** which is coated with a lipid bilayer. The delivery of the entrapped guest (safranin O) is triggered by the presence of the surfactant DTAB.

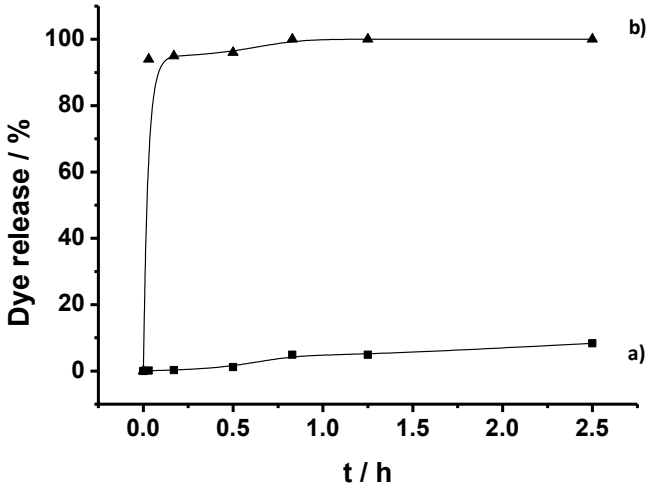

Figure 9. Release of safranin O dye from solid **S3** in the absence (a), and in the presence (b), of DTAB 0.1 mM.

5.4.2 Chemical communication studies between S1 and $S2_{dye}$

The interaction between solids **S1** and $\mathbf{S2_{dye}}$ was also studied. For this purpose, both materials were suspended in water and in water containing pancreatin at pH 7. Fractions of both suspensions were then centrifuged at certain time intervals and the amount of safranin O released was measured. The obtained results are shown in Figure 10. As it can be seen, in the absence of pancreatin (curve c) a poor safranin O release was observed, whereas in the presence of the enzyme a gradual emission enhancement was found (curve d). In addition to these delivery studies with **S1** and $\mathbf{S2_{dye}}$, further control experiments were carried out with solids $\mathbf{S1_{blank}}$ and $\mathbf{S2_{dye}}$ in order to test that the chromogenic response observed arises from the TCEP released from **S1**. As it can be seen in Figure 10 a poor dye release is observed when a mixture of $\mathbf{S1_{blank}}$ and $\mathbf{S2_{dye}}$ was suspended in water (curve a) or in water containing pancreatin (curve b). This absence of dye release from $\mathbf{S2_{dye}}$ indicated the pivotal role played by the TCEP released from **S1** in the cascade communication between **S1** and $\mathbf{S2_{dye}}$.

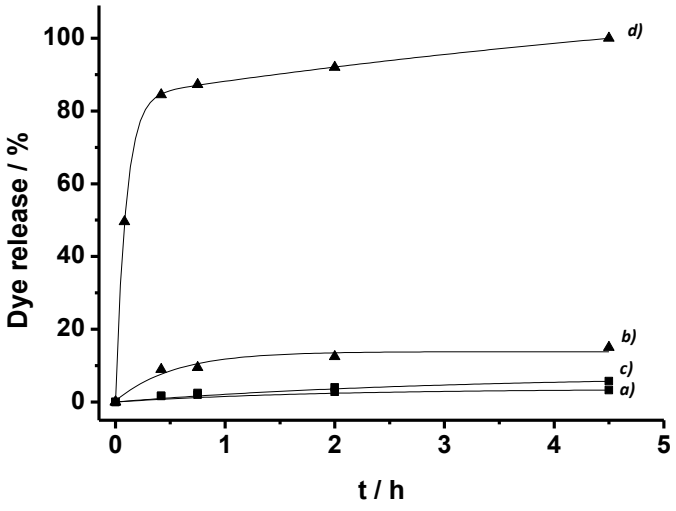

Figure 10. Release of safranin O from solid $\mathbf{S2_{dye}}$ in the presence of $\mathbf{S1_{blank}}$, in the absence (a), and in the presence (b), of pancreatin. Release of safranin O from solid $\mathbf{S2_{dye}}$ in the presence of **S1,** in the absence (c), and in the presence (d), of pancreatin.

5.4.3 Chemical communication studies between S1, S2 and S3

Having established the cargo delivery/retention performance of the individual nanoparticles with regard to stimulus selectivity, we next addressed actual chemical inter-particle communication. In this complex scenario, the final release of the dye from **S3** is expected to be related to the information that three different nanoparticles (**S1**, **S2** and **S3**) have previously shared via two different chemical messengers (**M1** and **M2**). In a typical experiment, **S1**, **S2** and **S3** were suspended in water at pH 7. After division of the suspension into two aliquots, pancreatin was added to one aliquot while the other was used as a control. Dye release was monitored at certain time intervals for both suspensions thought measuring the fluorescence emission of the dye. Typical delivery profiles of safranin O from **S3** in the presence and absence of pancreatin are displayed in Figure 11.

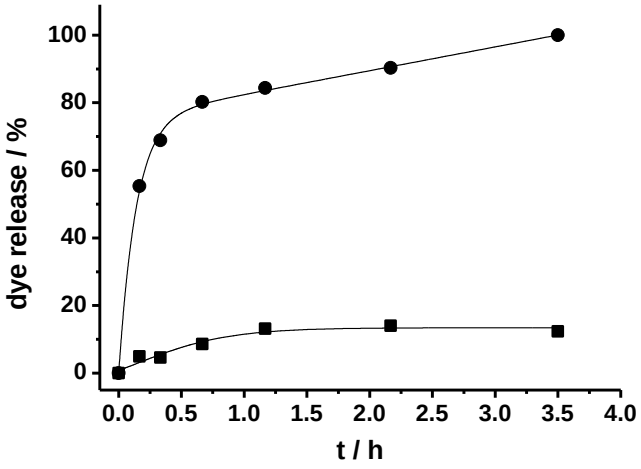

Figure 11. Release of safranin O from solid **S3** in aqueous mixture containing **S1**, **S2** and **S3** in the absence (■) and in the presence (●) of pancreatin enzyme.

Whereas in the absence of the enzyme, negligible safranin O release from **S3** was observed, a remarkable delivery of the fluorophore occurred in the presence of pancreatin, resulting in the liberation of 80% of the total dye release after 1h. Taking into account control experiments in which no dye delivery was found for **S3** alone in the presence of pancreatin, the high fluorescence generated from the community of the three different types of nanoparticles must have its origin in chemical inter-particle communication in the fashion illustrated in Figure 1, involving enzyme-triggered uncapping of **S1**, delivery of **M1**, **M1**-induced opening of **S2**, delivery of **M2** and **M2**-induced opening of **S3**. The opening of the pores of **S3** thus occurs remotely, through the information chain, via the stimulus selective gating chemistry of **S1**.

5.4.4 Communication studies with $S1_{blank}$ and $S2_{blank}$

In a hierarchical, cascade-like system as the one presented here, direct and sequential communication between the different particles is crucial and unintended cross-talk or "Chinese whispers" have to be avoided. This means that the specific interplay of gating chemistries and messenger molecules is essential. To get a deeper understanding of our communicating particle ensemble, additional studies were performed with $\mathbf{S1_{blank}}$ and $\mathbf{S2_{blank}}$—the gated hybrids lacking the cargo—substituting **S1** or **S2**. If the community **S1**/**S2**/**S3** shown above "talks" properly with one another, the communities $\mathbf{S1_{blank}}$/**S2**/**S3**, **S1**/$\mathbf{S2_{blank}}$/**S3** and $\mathbf{S1_{blank}}$/$\mathbf{S2_{blank}}$/**S3** should not be able to do so; their communication should either be disturbed or break down entirely, resulting in the absence of dye release from **S3**. In these experiments the corresponding solids were suspended in water and in water containing pancreatin. Fractions of both suspensions were then centrifuged at certain time intervals and the amount of safanin O released was measured fluorometrically. Water suspension of the combination of solids

S1$_{blank}$/S2$_{blank}$/S3, **S1$_{blank}$/S2/S3** and **S1/S2$_{blank}$/S3** showed a very poor safranin O release in both the presence and absence of pancreatin. This behaviour contrast with that observed for the mixture **S1**+**S2**+**S3** in the presence of pancreatin (Figure 12). These experimental observations indicated the relevance of **M1** and **M2** (TCEP and DTAB) in the cascade chemical communication between **S1**, **S2** and **S3** solids. The release of the entrapped safranin O from solid **S3** is a direct consequence of the delivery of **M1** (from solid **S1**) and **M2** (from solid **S2**).

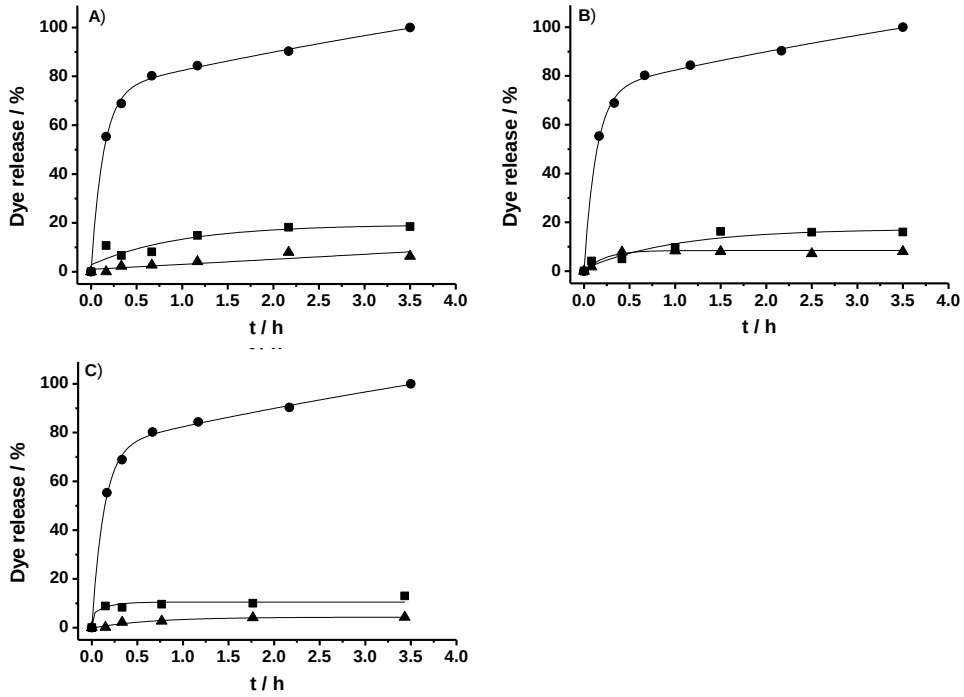

Figure 12. Safranin O released from (A) **S1$_{blank}$** +**S2$_{blank}$** +**S3** in the absence (▲) or in the presence (■) of pancreatin. (B) **S1$_{blank}$**+**S2**+**S3** in the absence (▲) or in the presence (■) of pancreatin. (C) **S1**+**S2$_{blank}$**+**S3** in the absence (▲) or in the presence (■) of pancreatin. For the sake of comparison in all three graphics the release behaviour of solids **S1**+**S2**+**S3** in the presence of pancreatin (●) is also plotted.

Simplified into Boolean logics, Table 3 collects how the observed output (delivery of safranin O from **S3**) depends on the nanoparticles being endowed with suitable

messengers (**S1** and **S2** vs. $\mathbf{S1_{blank}}$ and $\mathbf{S2_{blank}}$) and the presence of the primary stimulus pancreatin. The last row in Table 3 shows that a highly selective final response was only found for an intact community of gated MSNs.

Table 3. Release of safranin O from **S3** in the cascade chemical communication system depending on the use of capped nanoparticles containing messengers 1 (solid **S1**) and 2 (solid **S2**) or empty nanoparticles ($\mathbf{S1_{blank}}$ and $\mathbf{S2_{blank}}$) and the presence or absence of pancreatin

External Trigger[a] (Enzyme)	Presence of messenger M1[a] (TCEP)	Presence of messenger M2[a] (DTAB)	Response[b] (Safranin O)
0	0	0	0
0	1	0	0
0	0	1	0
1	0	0	0
1	1	0	0
1	0	1	0
1	1	1	1

[a] The presence or absence of the trigger and messengers in the MSN is represented by "1" and "0" respectively.

[b] Delivery or not of dye from **S3** is represented by 0 = no delivery, 1 = delivery. In particular "1" refers to a maximum dye release (100%) whereas "0" represents no release or poor release (typically less than 15%).

5.5 **Conclusions**

In summary, we have presented here the first proof of concept of a hierarchically organized community of different nanoparticles that can communicate through chemical messengers. The cargo delivery from a certain type of nanoparticle (**S3**) can only be triggered by a stimulus that acts remotely on another type of nanoparticle (**S1**) if the intermediate communication chain is intact. In particular, we sequentially used an enzyme (pancreatin) as the primary stimulus, a redox-active compound (TCEP) and a surfactant (DTAB) as the first and second messengers, and a dye as the final reporter. For our proof-of-principle, we used

three different types of nanoparticles yet the design features make it obvious that the concept can be extended to a larger number of inter-connected nanodevices. Although we are aware that the system we report herein is of limited real use, we believe that the conceptual idea that nanodevices can be designed to communicate with each other harbours enormous prospects for the development and application of cooperative systems in which complex behaviour can emerge as a result of a chemical interplay between individual simple abiotic components. Besides delivery,[16,17] sensing[17] and catalysis,[18] our approach may open a new, exciting and fruitful area of functional biomimetic chemistry.[19]

5.6 **Experimental Section**

5.6.1 Chemicals

The chemicals tetraethylorthosilicate (TEOS), *n*-cetyltrimethylammonium bromide (CTAB), sodium hydroxide (NaOH), tris(2-carboxyethyl)phosphine hydrochloride (TCEP), rhodamine B, 3-aminopropyltriethoxysilane, pancreatin from porcine pancreas, dodecyltrimethylammonium bromide (DTAB), safranin O, (3-mercaptopropyl)trimethoxysilane, 2,2'-dipyridyl disulfide , O-(2-mercaptoethyl)-O'-methyl-hexa(ethyleneglycol), 1,2-dioleoyl-*sn*-glycero-3-phosphocholine (DOPC), potassium chloride (KCl), potassium phosphate monobasic (KH_2PO_4) and sodium chloride (NaCl) were provided by Aldrich. The hydrolysed starch Glucidex 47 (5% glucose, 50% maltose, 45% oligosaccharides and polysaccharides) was provided by Roquette. The sodium phosphate dibasic heptahydrate (Na_2HPO_4) was provided by Acros. Anhydrous ethanol was provided by VWR International Eurolab (Barcelona, Spain), whereas other analytical-grade solvents were from Scharlab (Barcelona, Spain). All reactives were used as received.

[17] (a) P. Scrimin, L. J. Prins, *Chem. Soc. Rev.* **2011**, *40*, 4488. (b) R. Martínez-Máñez, F. Sancenón, M. Biyical, M. Hecht, K. Rurack, *J. Mater. Chem.* **2011**, *21*, 12588.

[18] M. Y. Darensbourg, R. D. Bethel, *Nat. Chem.* **2012**, *4*, 11.

[19] R. Breslow, *J. Biol. Chem.* **2009**, *284*, 1337.

5.6.2 General techniques

X-ray measurements were performed on a Philips D8 Advance diffractometer using CuK_α radiation. Thermo-gravimetric analysis were carried out on a TGA/SDTA 851e Mettler Toledo equipment, using an oxidant atmosphere (air, 80 mL/min) with a heating program consisting on a heating ramp of 10 °C per minute from 393 K to 1273 K and an isothermal heating step at this temperature for 30 minutes. N_2 adsorption-desorption isotherms were recorded on a Micromeritics ASAP2010 automated sorption analyser. The samples were degassed at 70 ^oC in vacuum overnight. The specific surfaces areas were calculated from the adsorption data in the low pressures range using the BET model. Pore size was determined following the BJH method. Fluorescence spectroscopy was carried out on a Felix 32 Analysis Version 1.2 (Build 56) PTI (Photon Technology International) and UV-visible spectroscopy was carried out with a Lambda 35 UV/Vis Spectrometer (Perkin Elmer Instruments). ^{1}H-NMR spectra were obtained on a Bruker AVANCE III 400 MHz spectrometer.

5.6.3 Synthesis of the materials

5.6.3.1 *Synthesis of the hydrolysed starch derivative (Glu-d)*

The hydrolysed starch Glucidex 47 (5.4 g) was previously maintained 1h at vacuum in a round bottomed flask in order to remove the adsorbed water. Afterward, the hydrolysed starch was suspended in anhydrous ethanol (250 mL) and 3-aminopropyltriethoxysilane (5.85 mL, 25 mmol) was then added. The reaction mixture was stirred in an inert atmosphere for 24 h at room temperature and then heated at 60 °C for 30 min. The solvent was evaporated under reduced

pressure to give a white solid (Glu-d). The ^{1}H NMR was coincident with the published by Bernardos et al.[15]

5.6.3.2 *Synthesis of the MCM-41 mesoporous silica nanoparticles (MSN)*

Mesoporous MCM-41 nanoparticles were synthesised by the following procedure: *n*-cetyltrimethylammonium bromide (CTAB, 1.00 g, 2.74 mmol) was first dissolved in deionized water (480 mL). Then, an aqueous solution of NaOH (3.5 mL, 2.00 mol L^{-1}) was added followed by adjusting the solution temperature to 80 ^{o}C. TEOS (5.00 mL, 2.57 x 10^{-2} mol) was then added dropwise to the surfactant solution. The mixture was stirred for 2 h to give a white precipitate. Finally, the solid product was centrifuged, washed with deionized water and dried at 60 ^{o}C (MCM-41 as-synthesised). To prepare the final porous nanoparticles (MCM-41), the as-synthesised solid was calcined at 550 ^{o}C using an oxidant atmosphere for 5 h in order to remove the template phase.

5.6.3.3 *Synthesis of S1*

500 mg of template-free MCM-41 were suspended in a solution of TCEP (564.81 mg, 1.96 mmol) in distilled water (38 mL) at pH 7 in a round-bottomed flask. The mixture was stirred for 24 h at room temperature with the aim of achieving the maximum loading in the pores of the MCM-41 scaffolding. Then, an excess of the functionalized hydrolysed starch derivative (Glu-d, 500 mg) was added and the final mixture was stirred for 5.5 h at room temperature. Finally, the solid **S1** was isolated by centrifugation, washed with abundant water, and dried at 40 ^{o}C for 12h.

5.6.3.4 *Synthesis of $S1_{dye}$*

The solid $\mathbf{S1_{dye}}$ was prepared following the same procedure described for **S1** but the MCM-41 material was loaded with rhodamine B dye. 500 mg of template-free

MCM-41 and the dye (191.60 mg, 0.4 mmol) were suspended in 30 mL of water in a round-bottomed flask. The mixture was stirred for 24 h at room temperature. Then, an excess of the functionalized hydrolysed starch derivative (Glu-d, 500 mg) was added and the mixture was stirred for 5.5 h at room temperature. Finally, the solid **S1$_{dye}$** was isolated by centrifugation, washed with abundant water, and dried at 40 ^{o}C for 12 h.

5.6.3.5 *Synthesis of S1$_{blank}$*

Solid **S1$_{blank}$** was prepared following the same procedure described for **S1** but without loading the pores of the MCM-41 scaffolding before its functionalisation. 100 mg of template-free MCM-41 were suspended in 10 mL of distilled water in a round-bottomed flask. Then, the functionalised hydrolysed starch derivative (Glu-d, 100 mg) was added and the mixture was stirred for 5.5 h at room temperature. Finally, the solid **S1$_{blank}$** was isolated by centrifugation, washed with abundant water, and dried at 40 ^{o}C for 12 h.

5.6.3.6 *Synthesis of S2*

500 mg of template-free MCM-41 were suspended in a solution of DTAB (3.08 g, 10 mmol) in distilled water (10 mL) in a round-bottomed flask. The mixture was stirred for 24 h at room temperature, filtered off and dried under vacuum. Afterward, the solid (300 mg) was re-suspended in acetonitrile (15 mL) in the presence of DTAB in order to inhibit the delivery of the surfactant from the pores to the bulk solution. Then, (3-mercaptopropyl)trimethoxysilane (557.25 µL, 3 mmol) was added and the mixture was stirred for 5.5 h at room temperature, in order to obtain thiol functionalized nanoparticles. In a further step, 2,2'-dipyridyl disulfide (660.92 mg, 3 mmol) was added to the reaction mixture. After stirring for 12 h at room temperature, the resulting solid was filtered off and dried under vacuum. Finally, a mixture of this prepared solid (50 mg) and O-(2-mercaptoethyl)-O'-methyl-hexa(ethylene glycol) (1.4 mmol) were suspended in acetonitrile (3.33 mL) in the presence of an excess of DTAB. The mixture was stirred for 12 h and the final solid **S2** was isolated by centrifugation, washed with abundant water and dried at 40 ^{o}C for 12 h.

5.6.3.7 *Synthesis of $S2_{dye}$*

The solid **$S2_{dye}$** was prepared following the same procedure described for **S2** but, in this case, the MCM-41 material was loaded with safranin O dye. For the preparation of this solid, 500 mg of calcined MCM-41 and safranin O dye (140.34 mg, 0.40 mmol) were suspended in distilled water (17 mL) in a round-bottomed flask. The mixture was stirred for 24 h at room temperature, filtered off and dried under vacuum. Afterward, this loaded solid (250 mg) was re-suspended in acetonitrile (8.5 mL) in the presence of an excess of safranin O and (3-mercaptopropyl) trimethoxysilane (464.38 µL, 2.5 mmol) was added. The suspension was stirred for 5.5 h at room temperature and then, 2,2'-dipyridyl disulfide (550.77 mg, 2.5 mmol) was added to the reaction mixture. After stirring for 12 h at room temperature, the resulting solid was filtered off and dried under vacuum. Finally, a mixture of this prepared solid (50 mg) and O-(2-mercaptoethyl)-O'-methyl-hexa(ethylene glycol) (1.4 mmol) were suspended in acetonitrile (3.33 mL) in the presence of an excess of safranin O. The mixture was stirred for 12 h and the final support $S2_{dye}$ was isolated by centrifugation, washed with abundant water and dried at 40 ^{o}C for 12 h.

5.6.3.8 *Synthesis of $S2_{blank}$*

Solid **$S2_{blank}$** was prepared following the same procedure described for **S2** but without loading the pores of the MCM-41 scaffolding before functionalisation. 250 mg of template-free MCM-41 was suspended in acetonitrile (8.50 mL) in a round-bottomed flask and (3-mercaptopropyl) trimethoxysilane (464.38 µL, 2.5 mmol) was added. The suspension was stirred for 5.5 h at room temperature and then, 2,2'-dipyridyl disulfide (550.77 mg, 2.5 mmol) was added to the reaction mixture. After stirring for 12 h at room temperature, the resulting solid was filtered off and dried under vacuum. Finally, a mixture of this solid (50 mg) and O-(2-mercaptoethyl)-O'-methyl-hexa(ethylene glycol) (1.4 mmol) were suspended in acetonitrile (3.33 mL) and stirred for 12 h at room temperature. The final support **$S2_{blank}$** was isolated by centrifugation, washed with abundant water and dried at 40 ^{o}C for 12 h.

5.6.3.9 *Synthesis of S3*

400 mg of calcined MCM-41 and safranin O dye (112.26 mg, 0.32 mmol) were suspended in PBS 0.25x buffer solution (10 mL) and the mixture was stirred for 24 h at room temperature. Afterward, a suspension of liposomes was prepared as follows. The lipid 1,2-dioleoyl-sn-glycero-3-phosphocholine (DOPC) (22.30 mg, 0.02 mmol) was dissolved in chloroform (5 mL) in a glass vial. The chloroform was then evaporated under nitrogen flow, and the lipid was dried under vacuum 1 h in order to remove any residual chloroform, obtaining lipid films. Then, PBS 0.25x (10 mL) was added and the medium was sonicated, obtaining a cloudy lipid suspension. In order to prepare the nanoparticles coated with the lipid bilayer, the liposome's suspension was added to the suspension of the MCM-41 support by manual pipetting. The mixture was allowed to sit at room temperature overnight. Finally, the nanoparticles were isolated by centrifugation, washed with abundant water and dried at 40 ^{o}C for 12 h.

5.6.4 Delivery studies

5.6.4.1 *Delivery studies with S1$_{dye}$*

In a typical experiment, 4 mg of **S1$_{dye}$** were suspended in 7.5 mL of distilled water at pH 7.5. After sonication, 2.5 mL of an enzyme suspension (pancreatin, 0.4 g in 100 mL of water at pH 7.5) was added. The suspension was stirred and the rhodamine B delivery was monitored through their emission band centred at 580 nm (λ_{exc} = 555 nm). A similar experiment using **S1$_{dye}$** but in the absence of pancreatin was also carried out.

5.6.4.2 *Delivery studies for S2$_{dye}$*

In a typical experiment, 0.5 mg of **S2$_{dye}$** were suspended in 2.70 mL of distilled water at pH 7.5. After sonication, 30 µL of a TCEP solution (10 mM) were added. The suspension was then stirred and dye delivery was monitored through the

emission band of safranin O centred at 585 nm (λ_{exc} = 520 nm). An identical experiment using **S2$_{dye}$** in the absence of TCEP was also carried out.

5.6.4.3 *Delivery studies for S3*

In a typical experiment, 0.5 mg of **S3** were suspended in 2.70 mL of distilled water at pH 7.5. After sonication, 30 μL of a DTAB solution (10 mM) were added. The suspension was then stirred and the delivery of safranin O was monitored through its emission band centred at 585 nm (λ_{exc} = 520 nm). An identical experiment in the absence of DTAB was carried out.

5.6.4.4 *Chemical communication studies between S1 and S2$_{dye}$*

For the chemical communication between solids **S1** and **S2$_{dye}$**, 0.5 mg of each material was suspended in 3 mL of water and in 3 mL of water containing pancreatin at pH 7. Fractions of both suspensions (0.3 mL) were then centrifuged at certain time intervals and the amount of safranin O released was measured by monitoring the emission band at 585 nm (λ_{exc} = 520 nm).

5.6.4.5 *Chemical communication studies between S1, S2 and S3*

In a typical experiment, 1.0 mg of each **S1**, **S2** and **S3** were suspended in 6 mL of water at pH 7. After division of the suspension into two aliquots, pancreatin was added to one aliquot while the other was used as a control. Fractions of both suspensions (0.3 mL) were then centrifuged and the dye release was monitored by sampling at certain time intervals and measuring the fluorescence emission of safranine O at 585 nm (λ_{exc} = 520 nm).

5.6.4.6 *Communication studies with **S1$_{blank}$** and **S2$_{blank}$***

In these experiments 0.5 mg of the corresponding solid were suspended in 3 mL of water at pH 7 and in 3 mL of water at pH 7 containing pancreatin. Fractions of both suspensions (0.3 mL) were then centrifuged at certain time intervals and the amount of safanin O released was measured fluorometrically.

6. Conclusions

Design of stimuli-responsive gated nanodevices has recently attracted significant attention in areas such as controlled delivery, offering a wide range of future applications. The present thesis has attempted to contribute to this field.

A general introduction has been included in the first chapter of this thesis. The main aspects of nanotechnology and the development of hybrid organic-inorganic mesoporous materials have been reported. In particular, the application of stimuli-responsive hybrid materials as controlled drug delivery systems was emphasized. Moreover, a brief description of some significant examples of gated nanodevices based on mesoporous silica supports for controlled delivery applications has been presented.

In the second chapter, a new approach for the development of gated materials using enzymes has been reported. More specifically, in this proof-of-principle, we have described a selective substrate-responsive gated mesoporous material based on the inorganic nanoscopic silica matrix MCM-41 capped with an active CD-modified-glucose oxidase enzyme and triggered by the presence of glucose as target substrate. We evaluated the response of the material as a function of the glucose concentration level and we were able to state that our nanodevice was in the range of other glucose-responsive reported detection systems. In addition, we concluded the material displayed a great selectivity toward glucose.

In the third chapter the design, synthesis, characterization and application of a new redox-responsive nanodevice for cargo delivery were reported. The gated material was based on MCM-41 mesoporous nanoparticles capped with highly hydrophilic and bio-compatible PEG derivatives through disulphide linkages. *In vitro* studies showed that the material designed was able to remain closed in non-reductive environments (for instance in plasma) yet delivered the cargo in an efficient way in the presence of a high concentrations of GSH (for instance in intracellular media). Moreover, viability assays in HeLa cells reveled the 'non'-toxicity of nanoparticles and confirmed their ability to deliver their cargo in a controlled manner in the intracellular reductive environment of cytosol.

In the fourth chapter a nanoscopic mesoporous silica based hybrid system, able to selectively release its cargo into senescent cells, was evaluated *in vivo* to target specifically senescent cells in fibrotic lungs of an IPF murine model. In a first step, the selectivity and targeted delivery of the synthesized nanodevice in senescent cells were confirmed with a senescence cellular model. Afterwards, *in vivo* studies were performed. In these studies, the hybrid material displayed a preferential cargo release in lungs of mice with pulmonary fibrosis when compared with control mice.

In the fifth chapter we have presented the first proof of concept of a hierarchically organized community of different nanoparticles that can communicate through chemical messengers and, given a specific external stimulus, offer a macroscopic response. Three different types of nanoparticles were designed, synthetized and characterized. *In vitro* studies confirmed that the cargo delivery from a certain type of nanoparticle (**S3**) was only triggered by a stimulus that acts remotely on another type of nanoparticle (**S1**) when the intermediate communication chain was intact.

In summary, it can be concluded that new hybrid organic-inorganic solids have been developed and their application as controlled delivery systems have been described in this thesis. A possible future development related with this thesis is the design of more biocompatible and more suspendable hybrid materials. In particular, the design of delivery supports able to be removed from the biologic system after the accomplishment of their diagnostic or therapeutic function is very interesting and a primordial issue to get into clinical applications.